

Quantifying resource states and efficient regimes of measurement-based quantum computation on a superconducting processor

by

Ryohei Weil

B.Sc., The University of British Columbia, 2022

A THESIS SUBMITTED IN PARTIAL FULFILLMENT OF
THE REQUIREMENTS FOR THE DEGREE OF
MASTER OF SCIENCE

in

The Faculty of Graduate and Postdoctoral Studies

(Physics)

THE UNIVERSITY OF BRITISH COLUMBIA
(Vancouver)

July 2024

© Ryohei Weil 2024

The following individuals certify that they have read, and recommend to the Faculty of Graduate and Postdoctoral Studies for acceptance, the thesis entitled:

Quantifying resource states and efficient regimes of measurement-based quantum computation on a superconducting processor

submitted by **Ryohei Weil** in partial fulfillment of the requirements for the degree of **Master of Science in Physics**.

Examining Committee:

Robert Raussendorf, Professor, Physics, Leibniz University Hannover
Co-supervisor

Andrew Potter, Associate Professor, Physics, UBC
Co-supervisor

Abstract

Recent theory has clarified the computational power of finite symmetric short-range entangled spin chains as resources for measurement-based quantum computation and the most efficient regimes of computation therein. In this work, we seek to experimentally demonstrate these advancements on IBM’s superconducting quantum processor. We variationally prepare resource states with tunable computational order and experimentally confirm the effects of logical decoherence on the encoded quantum information. We then demonstrate the equivalence of computational order and string order, and confirm the scaling relation of the logical decoherence with system size. We then construct a family of states with length scale to study the effects of correlated logical operations. We attempt to demonstrate that the “counterintuitive regime” of computation is the most efficient, i.e. that the densest possible packing of symmetry-breaking measurements minimizes logical decoherence. Our results are inconclusive for this last experiment. Our work demonstrates that noisy intermediate-scale quantum devices are capable of exploring novel phenomenology of measurement-based quantum computation beyond the cluster state.

Lay Summary

Quantum computers are devices that use the physical laws that govern quantum-mechanical systems to solve certain problems more efficiently than their classical counterparts. Existing quantum computers are too small and susceptible to errors for many such proposed applications. Nevertheless, they are a viable testbed for proof-of-concept demonstrations. In this thesis, we experimentally showcase recent theory results on measurement-based quantum computing. In this paradigm, a resource state is initially prepared as the substrate, and the computation proceeds by measuring different parts of the state in a specific pattern. A key research question is to determine how useful a given quantum state is as a resource in this setting. We showcase the answer on a superconducting quantum processor by preparing resource states of interest, measuring their computational power, and quantifying the efficiency of different measurement patterns.

Preface

The thesis consists of original research carried out in collaboration with Arnab Adhikary, Dr. Dmytro Bondarenko, and my supervisor Dr. Robert Raussendorf. The original motivation for the project was given by Robert, with the experimental predictions of Chapter 3 proposed by him and developed through discussion with Arnab, Dmytro, and I. Using a variational protocol to prepare resource states (Section 4.1.1) was proposed by Dmytro, with the variational ansatz provided by Robert and the details of the protocol (Section 4.1.2) developed by Robert and I. The resource state with length scale (Section 4.1.3) was proposed by me and analyzed in collaboration with Arnab. The protocol for accounting for non-unitary operations (Section 4.2.1) was proposed by Dmytro. The collection (via virtual interfacing with IBM hardware), post-processing and analysis of the experimental data of Chapter 5 was carried out wholly by me. The thesis has been written entirely by me and this work is yet to be published elsewhere.

Table of Contents

Abstract	iii
Lay Summary	iv
Preface	v
Table of Contents	vi
List of Tables	viii
List of Figures	ix
List of Abbreviations	x
List of Symbols	xi
Acknowledgements	xiii
1 Introduction	1
2 Background	4
2.1 A lightning review of quantum computing	4
2.2 Measurement-based quantum computing with cluster states	6
2.2.1 Quantum wire	7
2.2.2 Single-qubit operations	8
2.2.3 Two-qubit operations and universality	10
2.3 Measurement-based quantum computing beyond the cluster state	11
2.3.1 Measurement-based quantum computing with $\mathbb{Z}_2 \times \mathbb{Z}_2$ -symmetric states	11
2.3.2 The cluster phase and interpolation Hamiltonian	15
2.3.3 The counterintuitive regime	16
3 Predictions	19
3.1 Decoherence	19
3.2 Equivalence of string order and computational order	20
3.3 Rotation splitting	21
3.4 Counterintuitive is the most efficient	23
4 Methods	25

4.1	State preparation	25
4.1.1	Approximate ground states of the interpolation Hamiltonian	25
4.1.2	VQE protocols	26
4.1.3	The XX-rotated cluster state	29
4.2	Measurement-based quantum computing on a circuit model device	33
4.2.1	Unitary and non-unitary operations	36
4.3	Errors and mitigation	37
4.3.1	Readout errors	37
4.3.2	Gate errors	38
4.3.3	Thermal relaxation errors	39
5	Results	42
5.1	Decoherence	43
5.2	Equivalence of string order and computational order	44
5.3	Rotation splitting	45
5.4	Counterintuitive is the most efficient	48
6	Conclusion	54
	Bibliography	56

Appendices

A	Details on the VQE ansatz state	66
A.1	Perturbation theory calculation	66
A.2	VQE expectation value calculations	68
A.3	VQE circuit derivations	70
A.3.1	Derivation of $\langle X_i \rangle_\theta$ protocol	73
A.3.2	Tracing lemmas	74
A.3.3	Derivation of boundary $\langle K_i \rangle_\theta$ protocol	76
A.3.4	Derivation of bulk $\langle K_i \rangle_\theta$ protocol	78
A.4	Phase transition calculation	82
B	Details on the XX-rotated cluster state	83
B.1	Proof of string order parameter convexity	83
B.2	Efficient circuits for measuring string order parameters	84
B.3	Analytical calculations of loss in purity for various rotation splittings	89

List of Tables

4.1	Procedure for obtaining the expectation value of the local magnetic field term for the ansatz state of Eq. (4.1.2).	27
4.2	Procedure for obtaining the expectation value of the boundary cluster stabilizer term ($i = 0, 1, n, n + 1$) for the ansatz state of Eq. (4.1.2).	28
4.3	Procedure for obtaining the expectation value of the bulk cluster stabilizer term for the ansatz state of Eq. (4.1.2).	28
4.4	Procedure for the $d = 2$ string order parameter for the state of Eq. (4.1.10).	30
4.5	Probabilities for measurement of $s_2 + s_3 + s_4$ in $\sigma(2)$ measurement protocol.	30
4.6	Procedure for the $d = 4$ string order parameter for the state of Eq. (4.1.10).	31
4.7	Probabilities for measurement of $s_2 + s_3 + s_5 + s_6$ in $\sigma(4)$ measurement protocol.	31
4.8	Procedure for the $d = 6$ string order parameter for the state of Eq. (4.1.10).	32
4.9	Probabilities for measurement of $s_2 + s_3 + s_5 + s_7 + s_8$ in $\sigma(6)$ measurement protocol.	32
4.10	Pauli twirling of CZ and CNOT gates.	39

List of Figures

2.1	A single-qubit state visualized on the surface of the Bloch sphere.	5
2.2	Pictorial depiction of quantum teleportation on a cluster chain.	8
2.3	Z-rotation circuit identity.	9
2.4	Action of Z-measurements on a cluster state.	10
2.5	Realization of logical CNOT gate in MBQC.	11
2.6	Evolution of $ \overline{\mp}\rangle$ via the quantum channel of Eq. (2.3.7a) depicted on the $x - y$ plane of the Bloch sphere.	14
4.1	Architecture of <code>ibm_quebec</code> chip.	34
4.2	Simple example of MBQC protocol on a gate-based device.	35
5.1	Experimental results for variational state preparation.	42
5.2	Experimental test of Prediction 1 (Decoherence).	43
5.3	Plot of ratio of logical observables to extract computational order parameter.	44
5.4	Experimental test of Prediction 2 (String order is computational order).	45
5.5	Circuits for rotation splitting experiments.	46
5.6	Rotation splitting experimental data and comparison with theory/simulation.	47
5.7	Experimental test of Prediction 3 (Rotation splitting).	48
5.8	Experimental test of the convexity of the string order parameters $\sigma(d)$	49
5.9	Circuits for counterintuitive regime experiments.	50
5.10	Experimental test of Prediction 4 (The counterintuitive regime).	51
5.11	Comparison of loss in purities for 2/3/4 split rotations (with various spacings Δ) for $ \Omega(\phi)\rangle$ as a function of ϕ	52
A.1	Full (deterministic) circuit for measuring VQE observables.	72
B.1	Full circuit for measuring string order parameters of $ \Omega(\phi)\rangle$ state.	85

List of Abbreviations


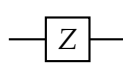
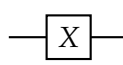
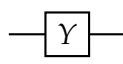
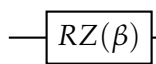
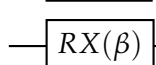
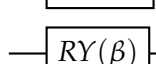
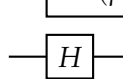
COP	Computational order parameter
CNOT	Controlled-NOT (X)
CZ	Controlled-Z
LP	Loss in purity
MBQC	Measurement-based quantum computing
NISQ	Noisy intermediate-scale quantum
SOP	String order parameter
SPT	Symmetry protected topological
SRE	Short-range entangled
VQE	Variational quantum eigensolver

List of Symbols

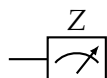
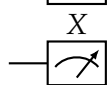
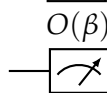
Quantum States

- $|0/1\rangle$ Computational basis states/Pauli-Z eigenstates
- $|\pm\rangle$ Pauli-X eigenstates
- $|C_G\rangle$ Cluster state defined on a graph G
- $|C_n\rangle$ Cluster state defined on a chain of n qubits

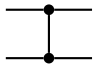
Single-qubit Gates

	$I = 0\rangle\langle 0 + 1\rangle\langle 1 $	Quantum wire/identity
	$Z = 0\rangle\langle 0 - 1\rangle\langle 1 $	Pauli-Z
	$X = 0\rangle\langle 1 + 1\rangle\langle 0 $	Pauli-X
	$Y = -i 0\rangle\langle 1 + i 1\rangle\langle 0 $	Pauli-Y
	$RZ(\beta) = \exp(-i\frac{\beta}{2}Z)$	Z-Rotation
	$RX(\beta) = \exp(-i\frac{\beta}{2}X)$	X-Rotation
	$RY(\beta) = \exp(-i\frac{\beta}{2}Y)$	Y-Rotation
	$H = +\rangle\langle 0 + -\rangle\langle 1 $	Hadamard

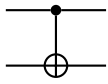
Single-qubit Measurements

	$\Pi_{0/1} = 0/1\rangle\langle 0/1 $	Computational basis/Z-basis Measurement
	$\Pi_{\pm} = \pm\rangle\langle \pm $	X-basis Measurement
	$\Pi_{\pm} = RX(\beta) \pm\rangle\langle \pm RX(-\beta)$	Rotated basis measurement

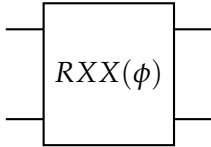
Two-qubit Gates



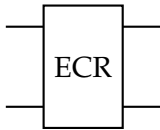
$$CZ = |0\rangle\langle 0| \otimes I + |1\rangle\langle 1| \otimes Z \quad \text{Controlled-Z}$$



$$CNOT = |0\rangle\langle 0| \otimes I + |1\rangle\langle 1| \otimes X \quad \text{Controlled-NOT}$$



$$RXX(\phi) = \exp(-i\frac{\phi}{2}XX) \quad \text{XX-Rotation}$$



$$ECR = \frac{1}{\sqrt{2}}(IX - XY) \quad \text{ECR}$$

Acknowledgements

I would like to foremost thank my supervisor Robert Raussendorf. This project would not have been possible without his insight and support, and without him I likely would not have chosen to pursue a course of study in quantum information or physics entirely. I am consistently impressed by his deep understanding of complex topics and his ability to explain them with exceptional clarity in discussions (though I admit that some of his papers still border on mathematical witchcraft at times). It's a shame that this is the last year he will be my advisor, but I am very grateful that he has been there to guide my journey in physics from the start until the present.

I would also like to thank Arnab Adhikary and Dmytro Bondarenko both for their scientific contributions to various aspects of this project and for their guidance through my BSc to my MSc. Dmytro has been very supportive and I admire his ability to maintain curiosity and hospitality whilst managing the stresses that come with being a new parent. Arnab has been there to cultivate my interest in quantum theory since my first undergrad quantum mechanics course, and since then has become a dear friend who I have turned to for microscopic (quantum) and macroscopic (life) advice alike. I hope to carry on with me their enthusiasm and passion for mentorship as I continue in my studies.

I would also like to thank Amrit Guha for his background and ideas for error mitigation strategies, as well as Daniel Huerga, Thierry Caldenbach, Alexandre Choquette, and Jinglei Zhang for insightful discussions at various stages of the project. Thank you also to Andrew Potter for agreeing to be a second reader for the thesis taking me on unofficially as a student - through his group I have been able to develop more of a background in condensed matter theory which I have found quite inspiring.

Thank you to Quantum Algorithms Institute and PinQ for providing access to IBM quantum services, and IBM for their development of the hardware and interface upon which the results of this thesis are based. The views expressed within this thesis are entirely mine, and do not reflect the official policy or position of IBM or the IBM Quantum team.

Outside of the people directly involved with this research, there are many others who were invaluable to my enjoyment and learning of these past two years. I had the fortunate opportunity to be a research resident at Xanadu, and would like to thank my residency supervisor Ilan, the other members of the architecture team, and the other 2023 summer residents for the many great memories. I also want to thank the other members (past and present) of the quantum theory group at UBC - Gabrielle, Luis, Michael, Paul, Polina - for great conversations about physics and everything else. Finally, thank you to my many friends from Choral Reef and Hugh Boyd Secondary as well as my family for their continued support and for filling my life with happiness.

Chapter 1

Introduction

Quantum computers are believed to exhibit computational speedups in certain tasks - a simple, yet insightful guiding question we will thus consider in this introduction is “what can a quantum computer do?”

The first interpretation of this question we consider is “what can a quantum computer do (in the future)?” Proposed applications include prime factorization [Sho97], database search [Gro96], quantum simulation [Llo96] (such as for quantum chemistry [MEAG⁺20] or more entertainingly, a system of coupled classical oscillators [BBK⁺23]), among others [DMB⁺23]. However, quantum devices are highly susceptible to noise and for many such envisioned applications quantum error correction [Sho95] is a strict requirement [SYGY24]. To this end, the field of fault-tolerance has seen rapid advancement, both in the theoretical search for good error correcting codes [BCG⁺24] [AF24] and in experimental demonstrations of repeated rounds of error correction [ZYH⁺22, PBP⁺23, dSRABR⁺24] and below-threshold scaling of logical error rates with increasing code distance [GAA⁺23, BEG⁺24].

Though these results are promising stepping stones to a future large-scale fault-tolerant quantum computer, for the most part currently available hardware remains rooted in the so-called “NISQ” (Noisy Intermediate-Scale Quantum) regime [Pre18] where devices consist of a small number of qubits at the mercy of noise. Thus a second interpretation of our guiding question we can consider is “what can a quantum computer do (now)?” There have already been multiple valiant attempts in available hardware to achieve quantum supremacy - such as through random circuit sampling [AAB⁺19, WBC⁺21, MVM⁺23, DHL⁺24], Gaussian boson sampling [ZWD⁺20, ZDQ⁺21, MLA⁺22, DGL⁺23] and quantum simulation [KEA⁺23, KNR⁺24]. However, many such claims have been challenged by advancements in classical algorithms [HZN⁺20, OLA⁺24, ZZP⁺24, TFSS24] and as such a convincing demonstration of supremacy - especially that for a useful task - (debatably) remains to be seen. Nevertheless, such hardware has shown promise as settings for exploring interesting physics, such as multipartite entanglement [WLX⁺24] and topological order [SLS⁺21, ITV⁺24].

A shared underlying thread of the two previous interpretations is “What can a quantum computer do (better than a classical computer)?” This question is arguably the central driving question in the theory of quantum information, and is an active research area with a myriad of directions. A non-exhaustive list of avenues of characterizing quantum-ness includes contextuality [HWVE14], wigner negativity [VFGE12], stabilizer theories [Got98], and quantum query complexity [Amb17]. For this thesis, the angle of our interest we shall focus on is that of measurement-based quantum computation (MBQC) [RBB03]. In MBQC, we first prepare (or are given) an entangled universal resource state, and the computation is carried out on it via adaptive single-qubit measurements. In this framework, the engine supplying the power to the

computation is the initial state, and thus we can recast the question of “What can a quantum computer do (better than a classical computer)?” into “How do we understand/classify quantum states that are useful as MBQC resources?”

Finding resources beyond the originally identified cluster state [RB01] is a generally difficult task given that such states are exponentially rare in Hilbert space [GFE09] - most states are, perhaps counterintuitively, too entangled. However, the search for such resources is elucidated in the presence of symmetry. Namely, states within the same symmetry-protected-topological (SPT) phase - those which can be smoothly deformed to each other via a low-depth (independent of system size), bounded-range, symmetry-respecting unitary circuit [CGW10] - have uniform computational power. The study of so-called *computational phases of matter* is a rich intersection of quantum information and condensed matter theory which has seen a wealth of developments.

Initial investigations identified computationally useful phases in 2-D without explicit connections to SPTs [DB09, Miy11, DBB12], with the first explicit connections to SPT order being made in the context of 1-D systems. There, the capability to perform quantum teleportation/wire was found to be uniform within an SPT phase [Miy10, ESD12]. This was extended to the capacity to do all single-qubit logical operations (i.e. single-qubit universality) [RWP⁺17] followed by a complete classification of resources using cohomological data [SWP⁺17]. In 2-D, investigations with an SPT lens showed the stability of the cluster state under symmetry-respecting perturbations to the parent Hamiltonian [EBD12], followed by the identification of various universal computational phases [DW18, ROW⁺19, SNBV⁺19, DAM20], though a full classification remains an open problem. In 3-D the question is even less explored, though phases possessing 1-form symmetry have been identified to have self-correction properties when acting as quantum memory [RB20].

All the above results center around phases of quantum matter, which is a notion only well-defined in the thermodynamic limit. However, any realistic computation takes place in a finite setting. To bridge this gap, the formalism has recently been generalized [RYA23], wherein short-ranged symmetric entangled spin chains are useful MBQC resources so long as they possess string order matching the symmetry - a quantity measurable in finite and infinite systems alike. In tandem, the most efficient regimes of computation in finite settings has been determined [AYR23]. MBQC on states with non-unit string order must manage the resulting logical decoherence, which can be mitigated via subdivision of the symmetry-breaking measurements necessary for the logical evolution of the encoded state. This rotation splitting technique features a tradeoff in finite spin chains, where densely packing/subdividing symmetry breaking measurements within the correlation scale of the system comes at the cost of the logical operations no longer being independent. In [AYR23] this tradeoff is resolved, with the densest possible packing of symmetry-breaking measurements - the so-called “counterintuitive regime” - being the most efficient.

Thus the stage has been set. Our exploration of the question “What can quantum computers do?” gave us a view of the NISQ era of quantum computation, where available devices are small and not protected from errors. It also gave us a view of MBQC, leading us to explore the state-of-the-art techniques with regards to characterizing MBQC resources and efficiency in a finite setting - precisely the setting relevant for NISQ devices. There has been some preliminary experimental work in this area, such as the analysis of stability of the cluster state to perform quantum wire under symmetry-respecting noise [AHN⁺20] as well as measurements of computational order [Wei22] in small 1-D systems. But with the theoretical understanding of 1-D MBQC now practi-

cally complete, the question becomes “Are such results observable in current experiment?” This is the question we will explore in this work.

The remainder of this thesis is organized as follows. In Chapter 2 we review the basics of quantum computation. We then provide the necessary background of MBQC on cluster states and short-ranged symmetric spin chains needed to parse the results of the thesis. In Chapter 3 we concretely present four predictions from the theory of MBQC in SRE symmetric spin chains that we wish to verify experimentally. In Chapter 4 we present the necessary tools for this experimental demonstration. We introduce the families of resource states of interest and their preparation, describe how to simulate MBQC on IBM’s circuit-model quantum device, and explain the error mitigation techniques used. In Chapter 5 we present the experimental results, confirming three of the four predictions. In Chapter 6 we conclude and discuss future directions of the work.

Chapter 2

Background

2.1 A lightning review of quantum computing

Zooming into the computers that we use on a daily basis, we find the base unit of information to be the bit - a binary 0 or 1. A classical computer can be abstractly described as a device that can apply any circuit of logic gates (such as ANDs and NOTs, with the choice of circuit depending on the computation) to manipulate a vector of \mathbb{F}_2^n (n bits) and obtain the desired output.

In a quantum computer, the base unit of information is promoted to the quantum bit, or qubit for short. We take the underlying field \mathbb{F}_2 and promote it to the Hilbert space \mathbb{C}_2 , with the a single-qubit state described as:

$$|\psi\rangle = a|0\rangle + b|1\rangle \quad (2.1.1)$$

with $|0/1\rangle$ the computational basis states and a, b as normalized complex coefficients. The normalization and the irrelevancy of global phase allows us to re-write the above as:

$$|\psi\rangle = \cos\left(\frac{\theta}{2}\right)|0\rangle + \sin\left(\frac{\theta}{2}\right)e^{i\phi}|1\rangle \quad (2.1.2)$$

which allows us to view a qubit state as a vector on the surface of the Bloch sphere, parameterized by polar angle θ and azimuthal angle ϕ . In this visualization we have the Pauli-Z eigenstates $|0/1\rangle$ as the north/south poles of the sphere and the Pauli-X eigenstates $|\pm\rangle = \frac{|0\rangle \pm |1\rangle}{\sqrt{2}}$ on opposing points of the equator. Single-qubit unitaries such as the Pauli-X with $X|0/1\rangle = |1/0\rangle$, the Pauli-Y with $Y|0/1\rangle = \pm i|1/0\rangle$, and Hadamard $H|0/1\rangle = |\pm\rangle$ can be viewed as rotations of the state vector around the sphere. A general rotation can be written as a sequence of rotations about the z and x axes via the Euler decomposition $R(\beta_0, \beta_1, \beta_2) = RZ(\beta_2)RX(\beta_1)RZ(\beta_0)$. A measurement with projector $\Pi_{\pm} = \frac{I \pm O}{2}$ of a single-qubit observable O results in projecting the state onto one of two antipodal points of the sphere (which are the eigenstates of O).

Later in the thesis we will also consider mixed states. To this end, we generalize the pure qubit state of Eq. (2.1.1) to the density operator:

$$\rho = \frac{I + r_x X + r_y Y + r_z Z}{2} \quad (2.1.3)$$

with:

$$\vec{r} = (r_x, r_y, r_z) = (\langle X \rangle, \langle Y \rangle, \langle Z \rangle) \in \mathbb{R}^3 \quad (2.1.4)$$

describing the state of the qubit as a point on the Bloch Ball (i.e. the Bloch sphere and its interior). The purity of the above state can be expressed as:

$$\text{Tr}(\rho^2) = \langle X \rangle^2 + \langle Y \rangle^2 + \langle Z \rangle^2 = r_x^2 + r_y^2 + r_z^2 = \|\vec{r}\|^2. \quad (2.1.5)$$

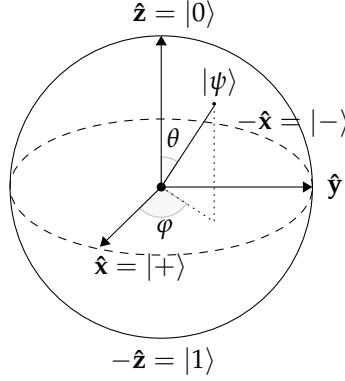


Figure 2.1: A single-qubit state $|\psi\rangle = \cos(\theta/2)|0\rangle + e^{i\phi}\sin(\theta/2)|1\rangle$ visualized on the surface of the Bloch sphere. Single-qubit unitaries can be viewed as the rotation of the vector around the sphere, e.g. $RZ(\beta) = \exp(-i\beta Z/2)$ would result in a rotation of $|\psi\rangle$ by angle β about the z -axis. Projective measurements can be viewed as the projection of the state onto one of two antipodal points, e.g. $|0\rangle/|1\rangle$ in the case of a computational basis measurement or $|\pm\rangle$ in the case of an X -basis measurement. Mixed states lie in the interior of the sphere, for example with $\rho = I/2$ (the origin) corresponding to the maximally mixed state. Figure adapted from [Wei22].

It is 1 for pure states on the surface of the Bloch sphere and < 1 for mixed states corresponding to points in the interior. In later parts of the thesis, we will see such states arise out of applications of linear combinations of unitaries, as well as experimental noise. For now, let's return to pure states.

In analogy with the model of a classical computer discussed above based on circuits, we can consider the circuit model of quantum computation. Here, a quantum computer is a device that applies a circuit of quantum gates corresponding to any desired unitary transformation $V \in SU(2^n)$ (with the choice of unitary depending on the computation) to manipulate a vector of \mathbb{C}_2^n (n qubits, initially in state $|0\rangle^{\otimes n}$) before measuring in the computational basis (potentially repeating the procedure multiple times given the probabilistic nature of the final measurement).

Readers with a computer science background may be familiar with the notion of universality in classical computing. There, a set of logic gates is said to be universal if they can be used to compute an arbitrary Boolean function - that is, any function $f : \{0,1\}^{n_1} \rightarrow \{0,1\}^{n_2}$. Examples of universal classical gate sets include $\{\text{AND}, \text{OR}, \text{NOT}\}$ and $\{\text{NAND}\}$ [NC10]. Like we generalized from bits to qubits, we generalize the notion of universality to quantum computing by defining a set of quantum gates to be universal if they can be used to approximate an arbitrary unitary $V \in SU(2^n)$ to arbitrary accuracy. This is of practical interest as on a physical device we only want to have to engineer a specific family of gates/operations rather than every multi-qubit transformation imaginable. One such possible gate set is the set of single-qubit rotations with Controlled-NOT (CNOT) gates, where the CNOT gate is a 2-qubit unitary which applies a Pauli- X on the target qubit (t) conditioned on the state of the control qubit (c), and can be written as:

$$\text{CNOT}_{c,t} = |0\rangle\langle 0|_c \otimes I_t + |1\rangle\langle 1|_c \otimes X_t. \quad (2.1.6)$$

While the single-qubit unitaries allow us to put qubit states into coherent superpositions, the

CNOT gates allow us to entangle different qubits in the computer - this is demonstrated perhaps the most clearly via the generation of the 2-qubit Bell pair:

$$\text{CNOT} |+\rangle = \frac{|00\rangle + |11\rangle}{\sqrt{2}}. \quad (2.1.7)$$

Not only is this universal gate set useful from the perspective of the engineer building a quantum device, we will derive theoretical use from it in demonstrating the universality of an alternative computational model - the one-way quantum computer - in the next section.

2.2 Measurement-based quantum computing with cluster states

In this section, we present an introductory overview of measurement-based quantum computation (MBQC). We discussed how in the circuit model, one starts with a register of n qubits in the $|0\rangle^{\otimes n}$ state, performs some arbitrary unitary via a sequence of some universal gates, and then measures at the end in the computational basis. In the measurement-based model we take a different approach. In the first step, we are either given or unitarily prepare some (entangled) universal resource state. After this, we never access unitary transformations at any point. Instead, the entire computation is carried out via single-qubit adaptive measurements on the resource state, which gets consumed as the computation proceeds. From an engineering perspective, this paradigm is useful for experimental platforms for which this resource state can be efficiently constructed (e.g. neutral atoms [RB01]) or those for which quantum data registers cannot be stationary in time (e.g. photons [WRR⁺05, BAV⁺21]). From a theoretical perspective, the classification of MBQC resource states provides an avenue to characterize the power of quantum computers.

We begin by presenting the original construction of MBQC using cluster states as the resource state [RB01, RBB03]. We begin by giving an operational definition of a cluster state (equivalently known as a graph state). Given a graph $G = (V, E)$ with vertices V and edges E , the cluster state $|C_G\rangle$ is defined as the state prepared by the following procedure:

1. On each vertex $v \in V$, prepare a qubit in the Pauli-X eigenstate $|+\rangle$.
2. For every pair of qubits connected by an edge $(a, b) = e \in E$, apply a controlled-Z (CZ) gate, i.e.:

$$\text{CZ}_{a,b} = |0\rangle\langle 0|_a \otimes I_b + |1\rangle\langle 1|_a \otimes Z_b = \frac{I_a I_b + I_a Z_b + Z_a I_b - Z_a Z_b}{2} \quad (2.2.1)$$

Note that the CZ gates in the second step are symmetric and mutually commute, so they can be applied simultaneously. Physically, the second step may be accomplished via evolving the qubits under translation-invariant nearest-neighbour Ising-type interaction:

$$H_{\text{Ising}} = -\hbar g \sum_{(a,b) \in E} \frac{I_a - Z_a}{2} \frac{I_b - Z_b}{2}. \quad (2.2.2)$$

This operational definition is useful for the preparation of cluster states. We now present a second, equivalent definition of the cluster state as a stabilizer state. Given a graph $G = (V, E)$,

the cluster state $|C_G\rangle$ is the unique +1 eigenstate of all Pauli operators in the set:

$$\left\{ K_a = X_a \prod_{b \in N(a)} Z_b \mid a \in V \right\} \quad (2.2.3)$$

where $N(a) = \{b \mid (a, b) \in E\}$ is the neighbourhood of the vertex a . The K_a are known as the cluster state stabilizer generators.

To see that these two definitions are equivalent, we simply need to track the stabilizers of the state presented in the preparation protocol of the first definition and show that they coincide. In the first step, the stabilizer generators are simply X_a for each vertex $a \in V$. Let us see how this stabilizer evolves under a CZ gate with a neighbouring qubit:

$$X_a \mapsto (CZ_{a,b})X_a(CZ_{a,b})^\dagger = \frac{I_a I_b + I_a Z_b + Z_a I_b - Z_a Z_b}{2} X_a \frac{I_a I_b + I_a Z_b + Z_a I_b - Z_a Z_b}{2} = X_a Z_b \quad (2.2.4)$$

where in the last equality we use the anticommutation of Z_a, X_a and that Paulis square to the identity. Repeating this conjugation for every edge/CZ connected to qubit a , we find that the stabilizer becomes:

$$X_a \mapsto X_a \prod_{b \in N(a)} Z_b = K_a \quad (2.2.5)$$

the argument is analogous for any vertex $a \in V$ and hence the final cluster state has stabilizers K_a for each vertex, showing the equivalence.

This second definition is convenient for two reasons. For one, we will find for some calculations that tracking the stabilizers of the cluster state under various operations is more convenient compared to keeping track of the state ket. Second (and perhaps more importantly), the above definition allows us to view the cluster state as the unique ground state of the cluster state Hamiltonian:

$$H_{\text{cluster}} = - \sum_{a \in V} K_a. \quad (2.2.6)$$

This framing in terms of Hamiltonians will give rise to condensed-matter-theoretic analysis of phases of useful resource states (so called computational phases of matter), and give us a way to interpolate between a useful resource (the cluster state) and a product state. Within this thesis we will switch back and forth between the definitions as convenient.

2.2.1 Quantum wire

In the remainder of this section, we will show that adaptive measurements on cluster states provide all of the computational primitives necessary for universality. We start with the simplest primitive - the ability to move quantum information from one part of a cluster state to another, which is known as quantum wire. For this, we consider a one-dimensional cluster chain, of odd length $n + 2$. We use 0-based indexing to denote the qubits. Suppose on the (leftmost) edge of the chain we have an input state $|\psi_{\text{in}}\rangle = a|0\rangle + b|1\rangle$. Then, focusing on the first two qubits, we have the state:

$$CZ_{0,1} |\psi_{\text{in}}\rangle_0 \otimes |+\rangle_1 = a|0\rangle_0 |+\rangle_1 + b|1\rangle_0 |-\rangle_1 = |+\rangle_0 (a|+\rangle_1 + b|-\rangle_1) + |-\rangle_0 (a|+\rangle_1 - b|-\rangle_1) \quad (2.2.7)$$

If we measure the first qubit in the X -basis and obtain outcome s_0 (taking $s_0 = 0$ if we measure the $+1$ eigenvalue and $s_0 = 1$ if we measure the -1 eigenvalue), the resulting state on the second qubit is:

$$a|+\rangle_1 + bX^{s_0}|-\rangle_1 = HZ^{s_0}(a|0\rangle_1 + b|1\rangle_1) = HZ^{s_0}|\psi_{\text{in}}\rangle_1 \quad (2.2.8)$$

In other words, up to the operator HZ^{s_0} the X -measurement on the first qubit has teleported the input state $|\psi_{\text{in}}\rangle$ to the second qubit. The HZ^{s_0} is known as a byproduct operator and can be kept track of classically to correct the output state at the end. This modification on the quantum teleportation protocol [BBC⁺93], called “half-teleportation” allows us to wire quantum information from one part of the cluster state to another¹. We can repeat this process along the $n + 2$ -qubit chain, measuring all qubits in the X basis save for the rightmost qubit; the output state on this last qubit is simply the output of $n + 1$ half-teleportations:

$$\begin{aligned} HZ^{s_n} HZ^{s_{n-1}} \dots HZ^{s_2} HZ^{s_1} HZ^{s_0} |\psi_{\text{in}}\rangle_{n-1} &= X^{s_n} Z^{s_{n-1}} \dots Z^{s_2} X^{s_1} Z^{s_0} |\psi_{\text{in}}\rangle_{n-1} \\ &\cong X^{\sum_{i,\text{odd}} s_i} Z^{\sum_{i,\text{even}} s_i} |\psi_{\text{in}}\rangle_{n-1} \end{aligned} \quad (2.2.9)$$

where we note we have used the irrelevancy of global phase to combine the X and Z operators. Up to the total byproduct operator $X^{\sum_{i,\text{odd}} s_i} Z^{\sum_{i,\text{even}} s_i}$ which can be classically tracked and applied, we have successfully teleported the initial quantum state from one end of the chain (qubit 0) to the other (qubit $n + 1$).

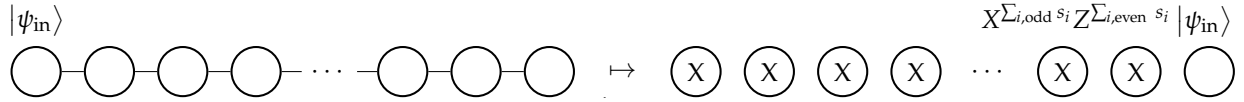


Figure 2.2: Pictorial depiction of quantum teleportation on a cluster chain. A linear cluster state is constructed with $|\psi_{\text{in}}\rangle$ as a logical input qubit state on the first qubit. By measuring all the qubits (save the last) in the X -basis, up to a measurement outcome-dependent byproduct operator, $|\psi_{\text{in}}\rangle$ is teleported to the final qubit.

2.2.2 Single-qubit operations

We now have the ability to teleport our quantum state - the MBQC equivalent of the identity operation. We now expand our toolkit to logical evolutions of our encoded single-qubit state. To this end, suppose we wanted to perform the Z -rotation $RZ(\beta)$. One way would be to input $RZ(\beta)|\psi_{\text{in}}\rangle$ instead of $|\psi_{\text{in}}\rangle$, and then the output from the previous part would be $HZ^{s_0}RZ(\beta)|\psi_{\text{in}}\rangle$. This however would contradict the central idea of MBQC, that we don't have access to unitary operations beyond the initial construction of the resource state. But, let us see if we can accomplish something equivalent with the single-qubit measurements that we do have. First, note that we can commute the z -rotation across the CZ gate:

$$\Pi_{\pm}^0 CZ_{0,1} RZ^0(\beta) |\psi_{\text{in}}\rangle_0 |+\rangle_1 = \Pi_{\pm}^0 RZ^0(\beta) CZ_{0,1} |\psi_{\text{in}}\rangle_0 |+\rangle_1 \quad (2.2.10)$$

¹Those with a background in quantum mechanics are likely unsurprised by the ability for cluster states to carry out quantum wire, as the 2-qubit cluster state is nothing more than a 2-qubit Bell pair (up to a local Hadamard) which is the standard resource in the quantum teleportation protocol.

Now, let us see how the z-rotation modifies the X-basis measurement Π_{\pm} :

$$\Pi_{\pm} RZ(\beta) = \frac{I \pm X}{2} RZ(\beta) = RZ(\beta) RZ(-\beta) \frac{I \pm X}{2} RZ(\beta) \cong \frac{I \pm RZ(-\beta) X RZ(\beta)}{2} \quad (2.2.11)$$

where we use that $RZ(\beta) RZ(-\beta) = I$ and discard the final rotation in the last step by noting that unitary operations performed after the measurement are irrelevant. We see from the above that by measuring not in the X-basis but rather in the rotated basis of the observable:

$$O(\beta) = RZ(-\beta) X RZ(\beta) = \cos(\beta) X - \sin(\beta) Y \quad (2.2.12)$$

the logical state is not only teleported, but is rotated by $RZ(\beta)$, giving us the output of $HZ^{s_0} RZ(\beta) |\psi_{\text{in}}\rangle$ as desired.

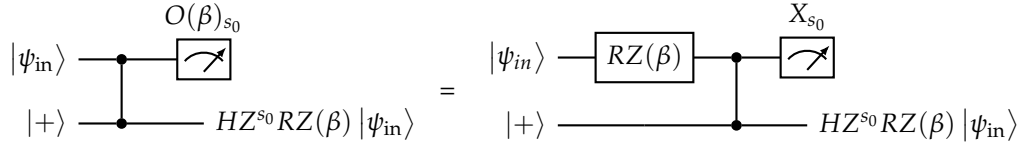


Figure 2.3: Z-rotation circuit identity. Measuring in the rotated basis of $O(\beta) = RZ(-\beta) X RZ(\beta)$ is logically identical to applying a Z-rotation on the input followed by a half-teleportation of the state. Therefore, we can implement a logical Z-rotation via choice of the measurement basis. Figure adapted from [Wei22].

To go from just Z-rotations to arbitrary rotations, we require the ability to perform a general rotation $R(\beta_0, \beta_1, \beta_2) = RZ(\beta_2) RX(\beta_1) RZ(\beta_0)$, invoking the Euler decomposition of rotations. To this end, we consider a 4-qubit cluster chain where we measure the first qubit in $O(\beta_0)$, the second qubit in $O(\beta_1)$, and the third qubit in $O(\beta_2)$. This amounts to three instances of the above procedure, so the quantum state of the fourth/output qubit will be:

$$HZ^{s_2} RZ(\beta_2) HZ^{s_1} RZ(\beta_1) HZ^{s_0} RZ(\beta_0) |\psi_{\text{in}}\rangle_3 = HZ^{s_2} RZ(\beta_2) X^{s_1} RX(\beta_1) Z^{s_0} RZ(\beta_0) |\psi_{\text{in}}\rangle_3 \quad (2.2.13)$$

Moving the byproduct operators to the left, we obtain:

$$HZ^{s_2+s_0} X^{s_1} RZ((-1)^{s_1} \beta_2) RX((-1)^{s_0} \beta_1) RZ(\beta_0) |\psi_{\text{in}}\rangle_3 \quad (2.2.14)$$

where we see that the byproduct operators do not just induce an irrelevant global phase but also flip the rotation angles. This at first seems problematic - the measurement outcomes are random and this poses obstacle to the deterministic implementation of $RZ(\beta_2) RX(\beta_1) RZ(\beta_0)$. However, this is not the case. We can adaptively choose future measurement bases conditioned on the past measurement outcomes, namely choosing the measurement basis of $O((-1)^{s_0} \beta_1)$ conditioned on the outcome of the first qubit and the basis of $O((-1)^{s_1} \beta_2)$ conditioned on the outcome of the second qubit. This deterministically yields the output:

$$HZ^{s_2+s_0} X^{s_1} RZ(\beta_2) RX(\beta_1) RZ(\beta_0) |\psi_{\text{in}}\rangle_3 \quad (2.2.15)$$

as desired. We thus are able to perform arbitrary single-qubit unitaries via adaptive single-qubit measurements on the (linear) cluster state, and thus the cluster chain is universal for a

single-qubit quantum computation. This adaptivity is the key ingredient that makes MBQC deterministic despite the probabilistic nature of quantum measurement, and is what gives rise to temporal order within MBQC. We also make the brief observation that rotated-based measurements on even qubits gave rise to logical Z-rotations and those on odd qubits gave rise to logical X-rotations. In the proceeding sections we will see that this is a generic feature that arises from the $\mathbb{Z}_2 \times \mathbb{Z}_2$ symmetry of the cluster state.

2.2.3 Two-qubit operations and universality

We now upgrade from a cluster chain to a two-dimensional cluster state defined on a square grid. We saw how the action of X-measurements on a cluster state to teleport quantum information. Z measurements play a complementary role in MBQC - namely, they slice out qubits in the cluster. Operationally, this allows us to separate out a two-dimensional cluster into chains corresponding to different logical qubits, as demonstrated by Fig. 2.4. To each of these logical qubits, we may use the constructions of the previous section to perform arbitrary single-qubit logical operations.

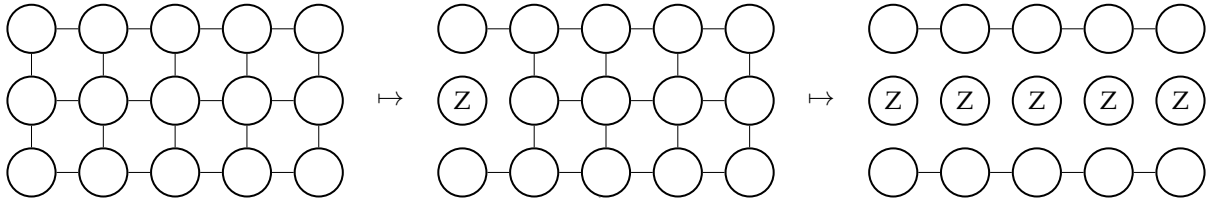


Figure 2.4: Z-measurements on a cluster state. In the central panel, we measure the leftmost center qubit in the Z basis, disconnecting it from the rest of the cluster. In the rightmost panel, we measure all central qubits in the Z basis, separating the cluster state into two cluster chains, each which correspond to a logical qubit. This procedure can be generalized to separate out a height $2k - 1$ rectangular cluster state into k logical qubits.

The slicing property of Z-measurements is most easily seen by looking at the stabilizers of the cluster state. Measuring in the Z-basis on qubit a enforces a new stabilizer $\pm Z_a$. This commutes with all cluster state stabilizers save for the one centered on a , i.e. $K_a = X_a \prod_{b \in N(a)} Z_b$. This one stabilizer is removed/replaced by Z_a , and thus this qubit is removed/disentangled from the overall cluster state (the rest of which is left intact). Hence, Z-measurements allow us to separate regions of a given cluster state. By extending the height of the cluster state and separating chains, we gain the ability to simulate an arbitrary number of logical qubits.

Given a sufficiently large graph state, we now possess the ability to simulate an arbitrary number of qubits and single-qubit operations on such qubits. To promote our scheme to universality, we require one more operation, namely the ability to carry out two-qubit entangling gates. Here we present the simplest such construction, namely a controlled-NOT (CNOT) gate between two logical qubits using 4 physical qubits of the cluster. This is graphically depicted in Fig. 2.5.

Thus, with arbitrary single unitaries and the CNOT, we have an universal gate set. Given a sufficiently tall (to give us a sufficient number of logical qubits) and long (to give us sufficient circuit depth) cluster state we are therefore able to perform an arbitrary quantum computation. Thus single-qubit measurements on a two-dimensional cluster state is a universal model of quantum

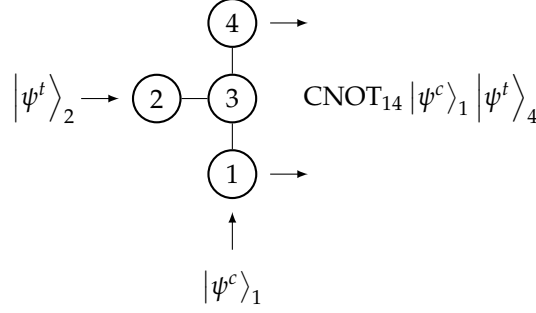


Figure 2.5: Realization of logical CNOT gate in MBQC. We consider the following subsection of the cluster state composed of 4 physical qubits. On qubits 1/2 we have the input states $|\psi^c\rangle_1$ and $|\psi^t\rangle_2$. Qubits 3/4 start in the $|+\rangle$ state. A CZ gate is applied between qubit 3 and 1/2/4. Then by measuring qubits 2/3 in the X-basis, the resulting output state on qubits 1/4 (up to byproduct operator $Z_1^{s_2} X_4^{s_3} Z_4^{s_2}$ depending on the measurement outcomes) is $\text{CNOT}_{14} |\psi^c\rangle_1 |\psi^t\rangle_4$.

computation². We also note that going to one higher dimension provides us with further phenomenology, with the jump to three-dimensional cluster states providing a method to perform MBQC fault-tolerantly [RHG06, RHG07]. However, for the remainder of this thesis we confine ourselves to 1-D MBQC. Though we lose of universality and fault-tolerance, in 1-D we have a comprehensive understanding of how to generalize MBQC beyond the cluster state in finite systems and efficient regimes of computation therein, which we explore in the next section.

2.3 Measurement-based quantum computing beyond the cluster state

2.3.1 Measurement-based quantum computing with $\mathbb{Z}_2 \times \mathbb{Z}_2$ -symmetric states

The construction of [RYA23] yields a classification of 1-D MBQC schemes for short-range entangled symmetric chains of qubits, based on their symmetry group $G = \mathbb{Z}_2^m$ and the representations of G (Theorem 1). The construction also yields the logical unitary operations accessible via such schemes as well as their efficiency (Corollary 1). Here, we discuss the implications for the universality and efficiency of MBQC on the cluster state and other short-range entangled $\mathbb{Z}_2 \times \mathbb{Z}_2$ symmetric states.

Let us unpack the setting by first precisely quantifying what we mean by short-range entangled (SRE). We consider chains of $n + 2$ qubits, with states:

$$|\Phi\rangle = W_\Phi(|+\rangle^{\otimes n+2}). \quad (2.3.1)$$

Here W_Φ is a unitary circuit which is low-depth (i.e. the depth of the circuit does not scale with the system size) and bounded-range (i.e. the locality of unitaries in the circuit does not scale with the system size). We quantify the SRE of W_Φ via the entanglement range ξ . Defining $\{\leq k\}$ and $\{> k\}$ as:

$$\{\leq k\} := \{0, 1, \dots, k\}, \quad \{> k\} := \{k + 1, k + 2, \dots, N\} \quad (2.3.2)$$

²We note also of the existence of a construction [SHW⁺22] that uses the machinery of dual-unitary circuits to accomplish universal MBQC in one spatial dimension.

we say that W_Φ has entanglement range ξ if:

$$\begin{aligned} \text{supp}(W_\Phi^\dagger A W_\Phi) &\subset \{\leq (k + \xi)\}, \forall A | \text{supp}(A) \subset \{\leq k\} \\ \text{supp}(W_\Phi^\dagger A W_\Phi) &\subset \{\geq (k - \xi)\}, \forall A | \text{supp}(A) \subset \{\geq k\} \end{aligned} \quad (2.3.3)$$

where $\text{supp}(A)$ is the support of operator A . In other words, W_Φ is sufficiently short-ranged such that it does not expand the support of operators beyond ξ . This is relevant for MBQC in that logical operations spaced out by sites $\geq 2\xi$ apart can be treated as independent, and the net logical evolution simply a composition of the two independent operations.

By $\mathbb{Z}_2 \times \mathbb{Z}_2$ symmetric, we refer to the states $|\Phi\rangle$ which are the +1-eigenstates of all elements in the group:

$$G = \mathbb{Z}_2 \times \mathbb{Z}_2 \cong \langle g_{01}, g_{10} \rangle = \langle Z_0 X_1 X_3 \dots X_n Z_{n+1}, X_0 X_2 X_4 \dots X_{n-1} X_{n+1} \rangle. \quad (2.3.4)$$

We can see from the stabilizer definition in Sec. ?? that the cluster chain is $\mathbb{Z}_2 \times \mathbb{Z}_2$ -symmetric as $Z_0 X_1 X_3 \dots X_n Z_{n+1}$ is the product of cluster state stabilizer generators on odd sites, and $X_0 X_2 X_4 \dots X_{n-1} X_{n+1}$ is the product of cluster state stabilizer generators on even sites. We can see from the operational definition that the cluster state is short-range entangled, as W_C is a circuit of CZ gates between neighbouring qubits and subsequently has an entanglement range of $\xi = 1$.

The logically encoded Pauli operators of the single qubit are:

$$\bar{Z} := T(g_{01}) = X_1 X_3 \dots X_n Z_{n+1} \quad (2.3.5a)$$

$$\bar{X} := T(g_{10}) = X_0 X_2 \dots X_{n-1} X_{n+1} \quad (2.3.5b)$$

$$\bar{Y} := T(g_{01}) = X_0 X_1 X_2 X_3 \dots X_{n-1} X_n Y_{n+1}. \quad (2.3.5c)$$

We provide some intuition for these operators - the measurement bases on the last qubit can be thought of the chosen basis for conducting the state tomography on the logically encoded qubit. Hence, it is O_{n+1} for the measurement of \bar{O} . The measurement outcomes of X_i s preceding the final qubit correspond to the relevant byproduct operators which flip the measurement outcome, with odd sites corresponding to X byproduct operators (which flip \bar{Z}/\bar{Y}) and even sites corresponding to Z byproduct operators (which flip \bar{X}/\bar{Y}), as we saw in the cluster state analysis of Eq. (2.2.9).

To measure the logical expectation values after performing rotations on the logical qubit, we replace the bulk X_i appearing in the above with $O_i = O_i(\beta_i) = \cos \beta X_i - (-1)^{q_i} \sin \beta Y_i$. q_i here denotes the sum of the prior measurement record $q_i = \sum_{j=1}^{i-2/1} s_{i-j}$ which is necessary for the adaptive selection of measurement bases.

$$\langle \bar{Z} \rangle = \langle O_1 O_3 \dots O_n Z_{n+1} \rangle \quad (2.3.6a)$$

$$\langle \bar{X} \rangle = \langle O_0 O_2 \dots O_{n-1} X_{n+1} \rangle \quad (2.3.6b)$$

$$\langle \bar{Y} \rangle = \langle O_0 O_1 O_2 O_3 \dots O_{n-1} O_n Y_{n+1} \rangle \quad (2.3.6c)$$

Up until this point, the formalism of this section applied just as well to our analysis of MBQC on the 1-D cluster state, and we have not presented anything new. Now comes the point of

departure. While a rotated basis measurement $O_i = O_i(\beta_i)$ on the cluster state resulted in a unitary (Z or X) rotation of the logically encoded qubit, for MBQC on general symmetric SRE spin chains the evolution of the encoded information takes the form of the quantum channels:

$$\mathcal{V}_k^{g_{01}}(\cdot) = \frac{1+\nu_k}{2}[\exp(-i\frac{\beta_k}{2}\bar{Z})] + \frac{1-\nu_k}{2}[\exp(i\frac{\beta_k}{2}\bar{Z})], \quad k \text{ even} \quad (2.3.7a)$$

$$\mathcal{V}_k^{g_{10}}(\cdot) = \frac{1+\nu_k}{2}[\exp(-i\frac{\beta_k}{2}\bar{X})] + \frac{1-\nu_k}{2}[\exp(i\frac{\beta_k}{2}\bar{X})], \quad k \text{ odd} \quad (2.3.7b)$$

where $[V]$ denotes a superoperator that acts on operators via conjugation - i.e. if $\mathcal{V} = [V]$ then $\mathcal{V}(A) = VAV^\dagger$. The $0 \leq \nu_k \leq 1$ appearing in the above channels are the *computational order parameters* (COPs), and control the degree of logical decoherence that is applied to the encoded state.

The presence of this logical decoherence is the fundamental feature (or perhaps more accurately, bug) of MBQC on general symmetric spin chains. To more clearly see how it manifests, let us study the Heisenberg evolution of the logical Paulis $\bar{X}, \bar{Y}, \bar{Z}$ via the Z-rotation channel of Eq. (2.3.7a) (analogous analysis applies to the X-rotation channel of Eq. (2.3.7b)). This will provide us with a geometric picture of the state evolution. Calculating the evolution of \bar{X} , we find:

$$\begin{aligned} \bar{X} &\mapsto \frac{1+\nu_k}{2} \exp(-i\frac{\beta}{2}\bar{Z}) \bar{X} \exp(i\frac{\beta}{2}\bar{Z}) + \frac{1-\nu_k}{2} \exp(i\frac{\beta}{2}\bar{Z}) \bar{X} \exp(-i\frac{\beta}{2}\bar{Z}) \\ &= \frac{1+\nu_k}{2} \left((\cos^2(\frac{\beta}{2}) - \sin^2(\frac{\beta}{2})) \bar{X} - 2 \cos(\frac{\beta}{2}) \sin(\frac{\beta}{2}) \bar{Y} \right) \\ &\quad + \frac{1-\nu_k}{2} \left((\cos^2(\frac{\beta}{2}) - \sin^2(\frac{\beta}{2})) \bar{X} + 2 \cos(\frac{\beta}{2}) \sin(\frac{\beta}{2}) \bar{Y} \right) \\ &= \cos(\beta) \bar{X} - \nu_k \sin(\beta) \bar{Y} \end{aligned} \quad (2.3.8)$$

and analogous calculations follow for \bar{Y}, \bar{Z} , allowing us to conclude:

$$\bar{X} \mapsto \cos \beta \bar{X} - \nu_k \sin \beta \bar{Y} \quad (2.3.9a)$$

$$\bar{Y} \mapsto \cos \beta \bar{Y} + \nu_k \sin \beta \bar{X} \quad (2.3.9b)$$

$$\bar{Z} \mapsto \bar{Z}. \quad (2.3.9c)$$

Thus if our input state has expectation values $\langle \bar{X}_0 \rangle / \langle \bar{Y}_0 \rangle / \langle \bar{Z}_0 \rangle$, from the above we obtain expectation values of the output state of the channel:

$$\langle \bar{X} \rangle = \cos \beta \langle \bar{X}_0 \rangle - \nu_k \sin \beta \langle \bar{Y}_0 \rangle \quad (2.3.10a)$$

$$\langle \bar{Y} \rangle = \cos \beta \langle \bar{Y}_0 \rangle + \nu_k \sin \beta \langle \bar{X}_0 \rangle \quad (2.3.10b)$$

$$\langle \bar{Z} \rangle = \langle \bar{Z}_0 \rangle. \quad (2.3.10c)$$

The logical one-qubit quantum state is in general described as a density operator (Eq. (2.1.4)) with $\vec{r} = (\langle \bar{X} \rangle, \langle \bar{Y} \rangle, \langle \bar{Z} \rangle)$ denoting the position of the state on the Bloch Ball. Thus Eqs. (2.3.10) allow us to see how the logical evolution pushes the logical information to be mixed. In particular, the COPs ν_k control how close the logical rotation is to the target unitary rotation. With $\nu_k = 1$ we recover exactly the unitary rotation $RZ(\beta)$, and with $\nu_k < 1$ the logical state is pushed into

the interior of the Bloch sphere. The other parameter of note is the rotation angle β . For $\beta = 0$ corresponding to the identity operation, there is no logical decoherence present - the ν_k drops out. This is due to the fact that $\beta = 0$ corresponds to $O(\beta = 0) = X$, which respects the $\mathbb{Z}_2 \times \mathbb{Z}_2$ symmetry of the resource state. The symmetry protects the quantum information when carrying out quantum wire and thus the purity of the state is preserved. However, to carry out logical evolution of the encoded qubit we of course need to measure in the rotated basis $O(\beta)$ for nonzero β . Such a measurement breaks the symmetry of the resource state (so long as β is not a multiple of π), resulting in logical decoherence. As a specific example, for $\beta = \frac{\pi}{2}$, we have a measurement in the $O(\beta = \pi/2) = Y$ basis, corresponding to a maximal violation of the symmetry and the largest amount of logical decoherence, as $\beta = \pi/2$ maximizes the terms $\propto \nu_k$ in the evolution. We illustrate the action of the quantum channel graphically in Fig. 2.6 below.

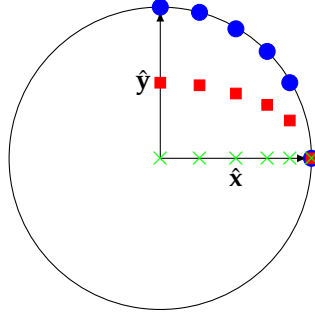


Figure 2.6: Evolution of $|\overline{+}\rangle$ via the quantum channel of Eq. (2.3.7a) depicted on the $x - y$ plane of the Bloch sphere. The logical input has $\langle \overline{X}_0 \rangle = 1$ and $\langle \overline{Y}_0 \rangle = \langle \overline{Z}_0 \rangle = 0$. Note that $\langle \overline{Z} \rangle = 0$ throughout the evolution, so the state remains on the $x - y$ plane. Blue dots correspond to a resource state with computational order parameter $\nu = 1$ (e.g. the cluster state), red squares correspond to a state with $\nu = 1/2$, and green crosses correspond to a state with $\nu = 0$ (e.g. the product state). A symmetry-respecting measurement by $O(\beta = 0) = X$ (rightmost points) carries out quantum wire (identity) with perfect fidelity, preserving the purity of the initial state. We then increase β ($\beta = \frac{\pi}{6}, \frac{\pi}{4}, \frac{\pi}{3}, \frac{5\pi}{12}$ - with each angle corresponding to one vertical slice of points) towards the maximally symmetry breaking angle of $\beta = \frac{\pi}{2}$. We then have unitary evolution for $\nu = 1$, while for $\nu = \frac{1}{2}$ and 0 the logical quantum information become mixed, with the state driven towards the interior of the Bloch sphere.

We have thus established how decoherence manifests in this setting and how the effect is dependent on the COPs $\{\nu_k\}_{k=1}^n$. The relevant consideration in analyzing a symmetric spin chain as a MBQC resource then becomes how the COPs depend on the state. This is addressed via identification of computational order as string order. More precisely, the computational order parameters ν_k are equal to the string order parameters (SOPs) $\sigma_k(g_{01})$ (even sites) and $\sigma_k(g_{10})$ (odd sites), which for $\mathbb{Z}_2 \times \mathbb{Z}_2$ -symmetric states are constructed to be:

$$\sigma_k(g_{01}) = \langle \Phi | Z_k X_{k+1} X_{k+3} \dots X_n Z_{n+1} | \Phi \rangle \quad (2.3.11a)$$

$$\sigma_k(g_{10}) = \langle \Phi | Z_k X_{k+1} X_{k+3} \dots X_{n-1} X_{n+1} | \Phi \rangle \quad (2.3.11b)$$

For the cluster state, we have $\nu_k = \sigma_k(g_{01}) = \sigma_k(g_{10}) = 1$ for all sites k (the Pauli string is simply a product of cluster state stabilizers) and hence the channels \mathcal{V}_k of Eq. (2.3.7) simply reduce to the

application of unitaries $RZ(\beta)/RX(\beta)$. For states with SOPs $\sigma_k(g) < 1$, \mathcal{V}_k is a linear combination of unitaries which drives the encoded quantum information towards a mixed state.

The decoherence that appears in this setting appears a priori seems to doom any MBQC (beyond quantum wire) on resource states with non-unit string order to fail. However, it turns out that there is a way to control this decoherence, in the presence of *any* nonzero string order. Specifically, assuming a sufficiently large chain size, the decoherence can be scaled down arbitrarily. Supposing that $|\sigma_k(g)| \geq \sigma > 0$ for all k , Corollary 1(ii) of [RYA23] ensures that the target unitaries $U(\beta) = \exp(-i\frac{\beta}{2}\bar{O})$ (with $\bar{O} = \bar{Z}$ or \bar{X}) can be approximated by repeated applications of the CPTP map of Eq. (2.3.7) via subdivision into m symmetry-breaking measurements in the eigenbasis of $O(\beta/m)$, with error³:

$$\epsilon_m \leq \frac{\beta^2}{m} \frac{1 - \sigma^2}{\sigma^2}. \quad (2.3.12)$$

for sufficiently small β , i.e. for that which $\beta/\sigma \ll 1$. Therefore, so long as we have a sufficiently long chain, we can split the logical rotation a large number of times m (with rotations β/m separated by $\Delta \geq 2\xi$ qubits) and arbitrarily suppress the error/deviations from unitarity. To carry out a general (potentially large) rotation we can simply compose multiple small rotations, and we can finally compose high-fidelity \bar{Z} and \bar{X} rotations to approximate any $SU(2)$ unitary to arbitrary accuracy.

Thus, the non-vanishing string order of a SRE $\mathbb{Z}_2 \times \mathbb{Z}_2$ -symmetric state $|\Phi\rangle$ indicates its universality for 1-D MBQC, with the magnitude of its SOPs acting as a measure of its efficiency as a resource.

2.3.2 The cluster phase and interpolation Hamiltonian

We consider the thermodynamic limit to connect the SOP-based formalism back to known results about computational phases of matter. In the process we introduce the interpolation Hamiltonian whose (approximate) ground states will be a central object of study in this thesis.

In the thermodynamic limit, we can define the $\mathbb{Z}_2 \times \mathbb{Z}_2$ cluster SPT phase as the phase of quantum states which can be smoothly connected to the cluster state via symmetry-respecting short-depth quantum circuits. We can analogously define the product phase as the phase of states smoothly connected to a product state. The symmetry-respecting condition is key - the depth-2 circuit W_C of CZ gates taking $|+\rangle^{\otimes n+2}$ to $|C_{n+2}\rangle$ is certainly short-depth and bounded-range⁴ but does not respect the $\mathbb{Z}_2 \times \mathbb{Z}_2$ symmetry. From the theory of computational phases, it is known that every state in the cluster phase is a universal resource for MBQC (while every state in the product phase is useless).

It is instructive to consider a line in this phase diagram of $\mathbb{Z}_2 \times \mathbb{Z}_2$ -symmetric states, namely the ground states of the cluster state Hamiltonian with transverse magnetic field:

$$H(\alpha) = -\cos(\alpha) \left[X_0 Z_1 + Z_n X_{n+1} + \sum_{i=1}^n Z_{i-1} X_i Z_{i+1} \right] - \sin(\alpha) \sum_{i=1}^n X_i. \quad (2.3.13)$$

³Here the error is quantified as the diamond norm distance[AKN98] between the target unitary $U(\beta)$ and the m -fold composition of $\mathcal{V}(\beta/m)$

⁴As a side note, this means that the cluster state possesses no genuine topological order, though it has SPT order.

with α the interpolation parameter. Note that the boundary qubits $i = 0, n + 1$ have no magnetic field so as to respect the symmetry. At $\alpha = 0$ the ground state is the cluster chain $|C_{n+2}\rangle$ and at $\alpha = \pi/2$ we have the four-fold degenerate product ground states $|\pm\rangle_0 |+\rangle_1 \dots |+\rangle_n |\pm\rangle_{n+1}$. In the thermodynamic limit, the phase transition from the (universal) cluster phase to the product phase occurs at $\alpha = \pi/4$, which can be observed from the sharp transition seen in the string order parameter as n is taken to be large, e.g. in Fig. 1 of [RYA23].

Even for finite systems, the above Hamiltonian interpolates between computationally useful states and computationally trivial states (though the decay of the string/computational order is smooth instead of sharp). Its ground states are thus prime candidates for showcasing the new formalism.

2.3.3 The counterintuitive regime

Before we discuss the concrete experimental predictions of our theory to test, one final question remains concerning the efficiency of MBQC schemes in finite settings. Namely, in the previous sections our protocol consisted of splitting a logical rotation m times across $\Delta \geq 2\xi$ separated qubits, and independently composing the sub-rotations to suppress the logical error by a factor of $1/m$. In the presence of correlations, can we achieve better efficiency by splitting the rotation as much as possible (i.e. $\Delta < 2\xi$ sites apart), at the expense of the logical operations no longer being independent? [AYR23] answers this in the affirmative.

Concretely, we consider states in the $\mathbb{Z}_2 \times \mathbb{Z}_2$ cluster phase. In addition to the SOPs of Eq. (2.3.11), the string order parameter between sites is defined to be:

$$\sigma_{k,l} := \langle \Phi | Z_k X_{k+1} X_{k+3} \dots X_{l-3} X_{l-1} Z_l | \Phi \rangle. \quad (2.3.14)$$

We assume that the system is translation invariant, i.e. that the circuit W_Φ that prepares the $\mathbb{Z}_2 \times \mathbb{Z}_2$ -symmetric $|\Phi\rangle$ is spatially uniform⁵. It then follows in the bulk of the chain that $\sigma_k = \sigma_\geq$ (i.e. the string order parameters from site k to the end of the chain are independent of k) and that $\sigma_{k,l} = \sigma(k-l) = \sigma(d)$ (i.e. the string order parameters between sites k, l only depend on the separation $d = k - l$ and are independent of k, l).

We first recast Eq. (2.3.7a) which governs the logical evolution of the single-qubit Pauli observables under even site symmetry-breaking measurements (Z-rotations) to matrix form (Eq. (B4) of [AYR23]):

$$\begin{bmatrix} \overline{X}' \\ \overline{Y}' \\ \overline{Z}' \end{bmatrix} = M_j \begin{bmatrix} \overline{X} \\ \overline{Y} \\ \overline{Z} \end{bmatrix} \quad (2.3.15)$$

where M_j is defined as (for even qubit j):

$$M_j := \begin{bmatrix} \cos \beta & -S_j \sin \beta & 0 \\ S_j \sin \beta & \cos \beta & 0 \\ 0 & 0 & 1 \end{bmatrix}. \quad (2.3.16)$$

⁵Translating this to a constraint on Hamiltonians, this means that the couplings present in the Hamiltonian are spatially uniform.

Here, $S_j = Z_j X_{j+1} X_{j+3} \dots X_n Z_{n+1}$ (such that $\langle S_j \rangle = \sigma_j$). After multiple symmetry-breaking (rotated basis) measurements on sites $k_1, k_2 \dots \in \mathcal{R}$, we obtain the expectation values of the Pauli observables at the end by iterating Eq. (2.3.15) and taking expectation values:

$$\begin{bmatrix} \langle \bar{X} \rangle \\ \langle \bar{Y} \rangle \\ \langle \bar{Z} \rangle \end{bmatrix} = \left\langle \left(\prod_{j \in \mathcal{R}} M_j \right) \begin{bmatrix} \bar{X}_0 \\ \bar{Y}_0 \\ \bar{Z}_0 \end{bmatrix} \right\rangle = \left\langle \left(\prod_{j \in \mathcal{R}} M_j \right) \right\rangle \begin{bmatrix} \langle \bar{X}_0 \rangle \\ \langle \bar{Y}_0 \rangle \\ \langle \bar{Z}_0 \rangle \end{bmatrix} \quad (2.3.17)$$

where the last equality follows from the short-range entangled nature of the state (and assuming that the rotation sites \mathcal{R} are much further than a correlation length from the start of the chain). This is the general equation for the logical evolution in the presence of correlations, with the many-body correlators in $\prod_{j \in \mathcal{R}} M_j$ (arising from products of the S_j s) accounting for the dependency between various parts of the evolution. We also note that while we focus on Z-rotations here, the formalism can be equivalently applied (via appropriate modification of Eq. (2.3.16)) to describe X-rotations.

With the general form of the logical evolution established, we consider an MBQC protocol conducted on a state $|\Phi\rangle$ in the cluster phase where we split a Z-rotation of angle β into m parts, separated by distance Δ . The resource state is $|\Phi\rangle$ in the cluster phase with string order parameters σ_{\geq} and $\sigma(d)$. The error ϵ_m in the overall logical operation (defined as the trace distance between the performed channel and the target unitary) can then explicitly calculated (Theorem 1 of [AYR23]) to be:

$$\epsilon_m = \frac{\beta^2}{m} \kappa(\Delta) + O\left(\frac{1}{m^2}\right) \quad (2.3.18)$$

with:

$$\kappa(\Delta) := \left(1 + 2 \sum_{j=1}^{N-1} f(j\Delta) \right) \left(\frac{1 - \sigma_{\geq}^2}{\sigma_{\geq}^2} \right) \quad (2.3.19)$$

such that:

$$f(\Delta) := \frac{(\sigma(\Delta) - \sigma_{\geq}^2)}{1 - \sigma_{\geq}^2}. \quad (2.3.20)$$

κ (which depends on the string order of $|\Phi\rangle$) captures the usefulness of the resource state $|\Phi\rangle$ for the MBQC, with the cluster state having $\kappa = 0$ as $\sigma_{\geq}^2 = 1$. We note that the above formulas do not require that $\Delta \geq 2\xi$, and indeed covers both the uncorrelated and correlated regimes, with $f(\Delta)$ capturing the strength of the correlations. $f(j\Delta) = 0$ corresponds to the uncorrelated regime where logical operations are independent, and we here recover the error scaling of Eq. (2.3.12).⁶

Given this explicit analytic form of the error, we are able to reason about the role that the site-separation Δ plays and how to choose it to minimize the error. Indeed, Theorem 2 of [AYR23] concludes that - so long the SOP $\sigma(d)$ is convex function of the distance d - in the thermodynamic limit the most efficient packing of rotations is to select $\Delta = 2$, i.e. the most dense packing of

⁶The astute reader may notice that Eq. (2.3.12) bounds the error via an inequality, while the error of Eq. (2.3.18) holds as an equality. This arises from the difference between the definition of error between the two expressions - namely, the former is derived as bound on the diamond distance while the latter is calculated explicitly using the trace distance. Importantly, both metrics yield the same $\frac{1}{m}$ scaling of the error.

rotations possible. Thus, we conclude that for MBQC in the finite setting the most efficient regime of computation (i.e. that which minimizes the logical decoherence) is the “counterintuitive” one where the logical operations are split as finely as possible, even at the expense of no longer being able to treat them independently.

Chapter 3

Predictions

In this section, we discuss the concrete theory predictions wish to experimentally test. For each prediction, we first provide a motivation for the effect, i.e. why a given effect is notable in the setting of MBQC with short-range entangled symmetric spin chains. We then derive the prediction from the theory of Section 2.3. We then state the prediction and the minimum system size for which it can be tested. Throughout, the setting is that of SRE $\mathbb{Z}_2 \times \mathbb{Z}_2$ -symmetric chains $|\Phi\rangle$.

3.1 Decoherence

The first prediction we make concerns logical decoherence. This is arguably the most fundamental effect to consider when doing MBQC on general symmetric spin chains. Unlike the cluster state where the symmetry-breaking measurements (rotated basis measurements) logically evolve the encoded quantum information unitarily, for a general resource state symmetry-breaking measurements results in the state evolving via a linear combination of unitaries, reducing the purity of the encoded state.

To this end, we recall the Heisenberg evolution of the Pauli operators of the encoded logical qubit upon a even-site rotated basis/symmetry breaking measurement $O(\beta)$ as given in Eq. (2.3.9):

$$\bar{X} \mapsto \cos \beta \bar{X} - \nu_k \sin \beta \bar{Y} \quad (3.1.1a)$$

$$\bar{Y} \mapsto \cos \beta \bar{Y} + \nu_k \sin \beta \bar{X} \quad (3.1.1b)$$

$$\bar{Z} \mapsto \bar{Z}. \quad (3.1.1c)$$

For simplicity, we initialize the logical state to be the +1 Pauli-X eigenstate $|\bar{+}\rangle$ with $\langle \bar{X}_0 \rangle = 1, \langle \bar{Y}_0 \rangle = \langle \bar{Z}_0 \rangle = 0$. The logical output/expectation values we measure in this protocol then become:

$$\langle \bar{X} \rangle(\beta) = \cos \beta \quad (3.1.2a)$$

$$\langle \bar{Y} \rangle(\beta) = \nu_k \sin \beta \quad (3.1.2b)$$

$$\langle \bar{Z} \rangle(\beta) = 0. \quad (3.1.2c)$$

Thus we obtain our first prediction:

Prediction 1: (Decoherence)

Consider the resource state $|\Phi\rangle$ with computational order parameters $\{\nu_k\}_{k=1}^n$. We perform an MBQC protocol using the $|\overline{+}\rangle$ state as input, a single symmetry-breaking/rotated basis measurement $O(\beta)$ (on qubit k), and subsequent readout of the output expectation values $\langle\overline{X}\rangle(\beta), \langle\overline{Y}\rangle(\beta)$.

Then, the curves in $\langle\overline{X}\rangle(\beta) - \langle\overline{Y}\rangle(\beta)$ space are ellipses with semi-major axes of 1 and semi-minor axes given by ν_k .

The minimum system size for which we can test this prediction is a 5-qubit $|\Phi\rangle$, where we perform a single rotated basis measurement $O(\beta)$ on the central qubit $k = 2$.

3.2 Equivalence of string order and computational order

In the previous experiment, the computational order parameter(s) $\{\nu_k\}_{k=1}^n$ controlled the strength of the logical decoherence. The relevant question when performing MBQC with a resource state $|\Phi\rangle$ then becomes “how does $\{\nu_k\}_{k=1}^n$ depend on $|\Phi\rangle$?” Our second prediction thus concerns the classification of resource states based on their computational order. Specifically, the theory predicts that the computational order parameter ν_k of Eq. (2.3.7a) dictating the fidelity of the logical operation at site k is equivalent to the string order parameter in Eq. (2.3.11a):

$$\sigma_k(g_{01}) = \langle\Phi| Z_k X_{k+1} X_{k+3} \dots X_n Z_{n+1} |\Phi\rangle. \quad (3.2.1)$$

Thus, the string order of $|\Phi\rangle$ defines its value as a computational resource. We seek to verify this equality experimentally. We consider the setting of the previous experiment, and divide the output expectation value of Eq. (3.1.2b) by Eq. (3.1.2a) to obtain:

$$\frac{\langle\overline{Y}\rangle(\beta)}{\langle\overline{X}\rangle(\beta)} = \nu_k \tan(\beta). \quad (3.2.2)$$

Thus the slope of $\frac{\langle\overline{Y}\rangle(\beta)}{\langle\overline{X}\rangle(\beta)}$ vs. $\tan(\beta)$ extracts the computational order parameter ν_k . Furthermore, we are able to independently measure the string order parameter $\sigma_k(g_{01})$ by preparing $|\Phi\rangle$ and measuring $Z_k X_{k+1} X_{k+3} \dots X_n Z_{n+1}$. We thus have the second experimental prediction:

Prediction 2: (Equivalence of string order and computational order)

Consider the resource state $|\Phi\rangle$ with computational order parameters $\{\nu_k\}_{k=1}^n$. We perform an MBQC protocol using the $|\overline{+}\rangle$ state as input, a single symmetry-breaking/rotated basis measurement $O(\beta)$ (on qubit k), and subsequent readout of the output expectation values $\langle\overline{X}\rangle(\beta), \langle\overline{Y}\rangle(\beta)$.

The computational order parameter ν_k is measured from the slope of $\frac{\langle\overline{Y}\rangle(\beta)}{\langle\overline{X}\rangle(\beta)}$ vs. $\tan(\beta)$. The string order parameter $\sigma_k(g_{01})$ is measured from the expectation value of $Z_k X_{k+1} X_{k+3} \dots X_n Z_{n+1}$.

Then, $\nu_k = \sigma_k(g_{01})$.

Again, the minimum system size for which we can test this prediction is a 5-qubit $|\Phi\rangle$, where we perform a single rotated basis measurement $O(\beta)$ on the central qubit $k = 2$. The relevant string order parameter is the cluster state stabilizer $\sigma_k(g_{01}) = \langle Z_2 X_3 Z_4 \rangle$.

3.3 Rotation splitting

We have now seen how decoherence manifests in MBQC in symmetric SRE spin chains, and how the string order of a spin chain defines its computational order. However, for the computation to succeed we must the logical decoherence - this is the topic of our third prediction. We demonstrate how the splitting of a single symmetry-breaking measurement $O(\beta)$ into m subdivided symmetry-breaking measurements $O(\frac{\beta}{m})$ allows us to (arbitrarily) scale down the logical decoherence by a factor of $\frac{1}{m}$.

In Eqs. (2.3.12) and (2.3.18), we see the factor of $\frac{1}{m}$ arise when comparing the diamond and trace norm distances (respectively) between the target unitary rotation and the CPTP map implemented by the m subdivided symmetry-breaking measurements, for small rotation angles β . Here, we probe a related and more experimentally accessible quantity, namely the loss in purity of the logical information; from Eq. (2.1.5) we can define the the loss in purity to be:

$$\text{LP} = 1 - \langle \bar{X} \rangle^2 - \langle \bar{Y} \rangle^2 - \langle \bar{Z} \rangle^2. \quad (3.3.1)$$

We show that this loss in purity exhibits the same $\frac{1}{m}$ scaling for small rotation angles. For simplicity, we again take the logical input to be $|\bar{+}\rangle$ with $\langle \bar{X} \rangle = 1, \langle \bar{Y} \rangle = \langle \bar{Z} \rangle = 0$. Furthermore, we consider $|\Phi\rangle$ with identical computational/string order parameters throughout such that $\nu_k = \sigma_k(g_{01}) = \sigma$ for each site k .

We now can calculate the evolution of the logical Paulis in the case of m Z-evolutions by recursively applying Eq. (2.3.9), and then calculate the loss in purity of the output quantum state from Eq. (3.3.1). We start by recasting Eq. (2.3.9) into matrix form:

$$M_k = \begin{bmatrix} \cos \beta_k & -\sigma \sin \beta_k \\ \sigma \sin \beta_k & \cos \beta_k \end{bmatrix}. \quad (3.3.2)$$

with M_k corresponding to the logical operation (induced by an $O(\beta_k)$ rotated basis/symmetry-breaking measurement) at site k . We assume that the logical operations are independent, i.e. the sites with symmetry-breaking measurements are separated by $\Delta \geq 2\xi$ with ξ the entanglement range of the circuit preparing $|\Phi\rangle$. With this assumption the total logical evolution is obtained from the m -fold product $\prod_k M_k$ (without this assumption, the logical operations are correlated and the logical evolution is dictated by Eq. (2.3.17)). Note that we leave out the Z-evolution as $\langle \bar{Z} \rangle (= 0)$ is invariant under Z-rotations. Diagonalizing M_k we have:

$$M_k = \begin{bmatrix} \frac{i}{\sqrt{2}} & -\frac{i}{\sqrt{2}} \\ \frac{1}{\sqrt{2}} & \frac{1}{\sqrt{2}} \end{bmatrix} \begin{bmatrix} \cos \beta_k + i\sigma \sin \beta_k & 0 \\ 0 & \cos \beta_k - i\sigma \sin \beta_k \end{bmatrix} \begin{bmatrix} -\frac{i}{\sqrt{2}} & \frac{1}{\sqrt{2}} \\ \frac{i}{\sqrt{2}} & \frac{1}{\sqrt{2}} \end{bmatrix} \quad (3.3.3)$$

Thus $\prod_k M_k$ is easily found to be:

$$\prod_k M_k = \begin{bmatrix} \frac{i}{\sqrt{2}} & -\frac{i}{\sqrt{2}} \\ \frac{1}{\sqrt{2}} & \frac{1}{\sqrt{2}} \end{bmatrix} \begin{bmatrix} \prod_k (\cos \beta_k + i\sigma \sin \beta_k) & 0 \\ 0 & \prod_k (\cos \beta_k - i\sigma \sin \beta_k) \end{bmatrix} \begin{bmatrix} -\frac{i}{\sqrt{2}} & \frac{1}{\sqrt{2}} \\ \frac{i}{\sqrt{2}} & \frac{1}{\sqrt{2}} \end{bmatrix} \quad (3.3.4)$$

Applying this to $\begin{bmatrix} \langle \bar{X}_0 \rangle \\ \langle \bar{Y}_0 \rangle \end{bmatrix} = \begin{bmatrix} 1 \\ 0 \end{bmatrix}$ we obtain the output expectation values:

$$\begin{bmatrix} \langle \bar{X} \rangle \\ \langle \bar{Y} \rangle \end{bmatrix} = \prod_k M_k \begin{bmatrix} \langle \bar{X}_0 \rangle \\ \langle \bar{Y}_0 \rangle \end{bmatrix} = \frac{1}{2} \begin{bmatrix} \prod_k (\cos \beta_k + i\sigma \sin \beta_k) + \prod_k (\cos \beta_k - i\sigma \sin \beta_k) \\ -i(\prod_k (\cos \beta_k + i\sigma \sin \beta_k) - \prod_k (\cos \beta_k - i\sigma \sin \beta_k)) \end{bmatrix} \quad (3.3.5)$$

Computing the loss of purity we then find:

$$\text{LP}_m = 1 - \langle \bar{X} \rangle^2 - \langle \bar{Y} \rangle^2 = 1 - \prod_k (\cos^2 \beta_k + \sigma^2 \sin^2 \beta_k) \quad (3.3.6)$$

We make the observation that the loss of purity is invariant under flips of a rotation angle on any site $\beta_k \leftrightarrow -\beta_k$. This has a beneficial implication for the experimental measurement, as we will discuss in Section 4.2 (namely, it will allow us to avoid post-selection). We are interested in the loss in purity from splitting a total rotation angle β into m parts of β/m , so let us set $\beta_k = \beta/m$ for all j in the expression above:

$$\text{LP}_m = 1 - (\cos^2 \frac{\beta}{m} - \sigma^2 \sin^2 \frac{\beta}{m})^m \quad (3.3.7)$$

In the limit of small β , we can expand the cosine/sine and look at the scaling of the quadratic terms:

$$\text{LP}_m \sim 1 - (1 - \frac{\beta^2}{m^2} + \sigma^2 \frac{\beta^2}{m^2})^m \sim 1 - \left(1 - m(1 - \sigma^2) \frac{\beta^2}{m^2}\right) = \frac{1 - \sigma^2}{m} \beta^2 \quad (3.3.8)$$

where with each \sim we drop terms of order β^3 and higher. Thus we obtain the claimed $\frac{1}{m}$ scaling of the small-angle loss in purity:

$$\text{LP}_m = \frac{1 - \sigma^2}{m} \beta^2 + \mathcal{O}(\beta^3). \quad (3.3.9)$$

Thus we obtain the following prediction:

Prediction 3: (Rotation splitting)

Consider the resource state $|\Phi\rangle$ with computational/string order parameters $\{v_k = \sigma\}_{k=1}^n$. We perform an MBQC protocol using the $|\overline{+}\rangle$ state as input, and perform m symmetry-breaking/rotated basis measurements $O(\beta/m)$ on even qubits $k_{i_1}, k_{i_2}, \dots, k_{i_m}$ and subsequent readout of the output expectation values $\langle \overline{X} \rangle, \langle \overline{Y} \rangle$. From these we compute the loss in purity.

Then, for small angles β we find that $LP_m \propto \frac{\beta^2}{m}$.

The minimum system size for which we can test this prediction is a 9-qubit $|\Phi\rangle$, prepared with a circuit of entanglement range $\xi = 1$. This allows us to compare the loss in purity between:

- (i) A single $O(\beta)$ measurement on qubit 2
 - (ii) Two $O(\beta/2)$ measurements, on qubit 2 and 4
 - (iii) Three $O(\beta/3)$ measurements, on qubit 2, 4, and 6.
- and we thus can verify the prediction for $m = 1, 2, 3$.

3.4 Counterintuitive is the most efficient

The first three experiments all considered MBQC in the regime where logical operations were independent. Generically, the correlations of a state presents the tradeoff between the $\frac{1}{m}$ scaling in the logical decoherence (encouraging the maximal splitting/densest packing of symmetry-breaking measurements) and treating the logical operations independently (encouraging symmetry-breaking measurements with $\Delta > 2\xi$ with ξ the entanglement range, or alternatively Δ much greater than the correlation length of the system). Our fourth and final prediction thus concerns the most efficient (i.e. decoherence-minimizing) regime of computation in the presence of correlations.

To this end, we consider resource states $|\Phi\rangle$ prepared with circuits of entanglement range $\xi > 1$ such that the effects of correlations must be considered. We require that the bulk string orders $\sigma(d) = \sigma(k-l) = \sigma_{k,l}$ of $|\Phi\rangle$ as defined by Eq. (2.3.14) are convex functions of the distance d . Finally, we assume that $|\Phi\rangle$ is large - Theorem 2 of [AYR23] then yields the following prediction:

Prediction 4: (Counterintuitive is the most efficient)

Consider the resource state $|\Phi\rangle$ such that the bulk string orders $\sigma(d)$ are convex in d and $|\Phi\rangle$ is large. We perform an MBQC protocol using the $|\overline{+}\rangle$ state as input, and perform m symmetry-breaking/rotated basis measurements $O(\beta/m)$ on even qubits $k_{i_1}, k_{i_2}, \dots, k_{i_m}$ and subsequent readout of the output expectation values $\langle \overline{X} \rangle, \langle \overline{Y} \rangle$. From these we compute the loss in purity.

Then, the protocol that minimizes the loss in purity is that for which the rotation is maximally subdivided, i.e. we have the densest packing of symmetry breaking measurements $O(\beta/N)$ (with $N = \frac{n-1}{2} \approx \frac{n}{2}$) on sites $k = 2, 4, 6, 8 \dots n-1$ - each separated by $\Delta = 2$.

The minimum system size for which we can test this prediction is an 11-qubit $|\Phi\rangle$, as this is the smallest resource state for which we can verify the convexity condition. Namely, we can measure $\sigma(2) = \sigma_{2,4}$, $\sigma(4) = \sigma_{2,6}$ and $\sigma(6) = \sigma_{2,8}$ and verify that $\sigma(2) \geq \sigma(4) \geq \sigma(6)$ and $\sigma(2) - \sigma(4) \geq \sigma(4) - \sigma(6)$.

For simplicity, we suppose $|\Phi\rangle$ can be prepared by a circuit of entanglement range ξ of 2 or 3. On this state we can compare three protocols, each which considers different ways of splitting up a Z -rotation by angle β :

- I. Two $O(\beta/2)$ measurements on qubits 2,4, i.e. a distance of $\Delta = 2 < 2\xi$ apart, such that the two logical operations are not independent.
- II. Two $O(\beta/2)$ measurements on qubits 2,8, i.e. a distance of $\Delta = 6 \geq 2\xi$ apart, such that the two logical operations are independent.
- III. Four $O(\beta/4)$ measurements on qubits 2,4,6,8, i.e. a distance of $\Delta = 2 < 2\xi$ apart, such that the two logical operations are independent. This is the densest packing of symmetry-breaking measurements possible.

For each of these protocols, we can measure the output expectation values of the logical Paulis to compute the loss in purity of Eq. (3.3.1). Comparing II with I/III, we have the gain that the two split rotations can be treated independently. III on the other hand splits the rotation angle as much as possible/has the densest packing of logical rotations. Thus, our prediction is that $\text{III} < \text{II} < \text{I}$ for the loss in purity.

This 11-qubit chain runs into the technical snag of violating one of the conditions of Theorem 2 - namely the assumption that the system size is large. We discuss the implications of this in detail in Section 5.4.

Chapter 4

Methods

4.1 State preparation

4.1.1 Approximate ground states of the interpolation Hamiltonian

Recall the interpolation Hamiltonian of Eq. (2.3.13) acting on a chain of $n + 2$ qubits:

$$H(\alpha) = -\cos(\alpha) \left[X_0 Z_1 + Z_n X_{n+1} + \sum_{i=1}^n Z_{i-1} X_i Z_{i+1} \right] - \sin(\alpha) \sum_{i=1}^n X_i. \quad (4.1.1)$$

For our first three experiments, we consider a simple variational ansatz for the ground states of the above Hamiltonian:

$$|\Psi(\theta)\rangle = T(\theta) |C_{n+2}\rangle = \bigotimes_{i=1}^n T_i(\theta) |C_{n+2}\rangle := \left(\bigotimes_{i=1}^n \cos(\theta) I_i + \sin(\theta) X_i \right) |C_{n+2}\rangle \quad (4.1.2)$$

with the cluster state $|C_{n+2}\rangle$ reproduced for $\theta = 0$. Note that we avoid the qubits at the end of the chain (qubits $0, n + 1$) such that the ansatz state retains the $\mathbb{Z}_2 \times \mathbb{Z}_2$ symmetry of the cluster state - T_0, T_{n+1} do not commute with $Z_0 X_1 I_2 \dots I_{n-1} X_n Z_{n+1}$. This ansatz suffices for the demonstration of Predictions 1-3 of the previous chapter.

The motivations for the ansatz are fivefold:

- (i) As alluded to above, it shares the $\mathbb{Z}_2 \times \mathbb{Z}_2$ symmetry of the Hamiltonian (2.3.13) and its ground states.
- (ii) It is short-ranged entangled. Specifically, it is a local modification of the cluster state, and thus the circuit to prepare it has the same entanglement range of $\xi = 1$. Note that the translation invariance combined with this fact also implies that the bulk computational/string orders $\nu_k = \sigma_k(g_{01})$ (Eq. (2.3.11a)) are all equal, as we assumed in our analysis in Section 3.3. This can also be seen via direct calculation (as discussed in Appendix A.2)
- (iii) It agrees with perturbation theory to quadratic order (see Appendix A.1)
- (iv) In the thermodynamic limit it predicts the existence of a phase transition, albeit in not the correct location (see Appendix A.4). This at first seems paradoxical as a local finite depth unitary circuit that respects the symmetry should not be able to cause a phase transition, and $T(\theta) = \bigotimes_{i=1}^n T_i(\theta)$ is local and symmetry-respecting. The subtlety is that $T_i(\theta) = \cos(\theta) I_i + \sin(\theta) X_i$ and thus T are *not* unitary, which gets around this condition.

As a concrete example, at $\theta = \pi/4$ $T_i(\theta) = \frac{I+X}{\sqrt{2}}$ is (up to normalization) a projector corresponding to a +1 X -measurement, which takes us from $|C_{n+2}\rangle$ in the cluster phase to a product state in the trivial phase - the ground state of $H(\alpha = \frac{\pi}{2}) = -\sum_{i=1}^n X_i$.

- (v) The locality makes for high-fidelity experimental preparation of the state, given that no additional entangling operations are required beyond the nearest-neighbour entangling gates required to prepare the cluster state.

4.1.2 VQE protocols

We use variational optimization to determine how the θ depends on the interpolation parameter α of the Hamiltonian. The variational theorem [SN20] ensures that the expectation value of a given Hamiltonian for any state $|\psi\rangle$ is always lower bounded by the true ground state energy:

$$\langle\psi|H|\psi\rangle \geq E_0. \quad (4.1.3)$$

The family of quantum algorithms known as variational quantum eigensolvers (VQE) [TCC⁺22] invoke this result to approximate the ground state and its energy. The central idea is to choose a variational ansatz state:

$$|\Psi(\vec{\theta})\rangle = U(\vec{\theta})|0\rangle^{\otimes n} \quad (4.1.4)$$

which is prepared on a quantum computer via parameterized circuit $U(\vec{\theta})$. Then, the expectation value of the energy can be measured:

$$E(\vec{\theta}) = \langle\Psi(\vec{\theta})|H|\Psi(\vec{\theta})\rangle \quad (4.1.5)$$

wherein $E(\vec{\theta})$ can be fed back into a classical computer and the parameters $\vec{\theta}$ updated. The approximation to the ground state energy is then obtained as the minimum taken over parameters $\vec{\theta}$:

$$E_0 \approx \min_{\vec{\theta}} \langle\Psi(\vec{\theta})|H|\Psi(\vec{\theta})\rangle \quad (4.1.6)$$

with the minimizing $\vec{\theta}$ giving an approximation to the ground state $|\Psi(\vec{\theta})\rangle$.

Here, our ansatz only contains a single parameter. Hence it suffices to compute the expectation value of the cluster state Hamiltonian and the transverse magnetic field Hamiltonian for various values of θ , and then for a given value of α choose the minimizing $\theta_{\min}(\alpha)$ that minimizes the sum of the two energies.

Hence we wish to measure and minimize:

$$\langle\Psi(\theta)|H(\alpha)|\Psi(\theta)\rangle = -\cos(\alpha) \sum_{i=0}^{n+1} \langle K_i \rangle_{\theta} - \sin(\alpha) \sum_{i=1}^n \langle X_i \rangle_{\theta}. \quad (4.1.7)$$

Due to the translation invariance of the ansatz state excepting the boundaries, there are only three independent expectation values to measure:

1. $\langle X_i \rangle_{\theta}$ the magnetic field at each (bulk) site ($i = 1, 2, \dots, n$)
2. $\langle K_i \rangle_{\theta}$ the boundary cluster state stabilizers ($i = 0, 1, n, n+1$)

3. $\langle K_i \rangle_\theta$ the bulk cluster state stabilizers ($i = 2, 3, \dots, n-1$)

A direct quantum-mechanical calculation (see Appendix A.2) of the expectation values yields:

$$\langle X_i \rangle_\theta = 2 \cos(\theta) \sin(\theta) \quad (4.1.8a)$$

$$\langle K_i \rangle_\theta = \begin{cases} \cos^2(\theta) - \sin^2(\theta) & i = 0, 1, n, n+1 \\ (\cos^2(\theta) - \sin^2(\theta))^2 & i = 2, 3, \dots, n-1 \end{cases} \quad (4.1.8b)$$

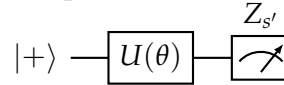
We now seek a quantum protocol to measure these expectation values. The most straightforward way to do so would be to prepare $|\Psi(\theta)\rangle$, and measure $X_0 X_1 \dots X_n X_{n+1}$ to obtain $\langle X_i \rangle_\theta$ and $Z_0 X_1 Z_2 X_3 \dots X_n Z_{n+1}$ and $X_0 Z_1 X_2 \dots Z_n X_{n+1}$ to obtain the $\langle K_i \rangle_\theta$ s. However, this intuitive method is suboptimal in that (a) the number of qubits in the circuit scales with the system size n and (b) The non-unitary $T_i(\theta)$ s can generically be only implemented probabilistically, with the success probability of preparing $|\Psi(\theta)\rangle$ decaying exponentially in the length of the chain. Using symmetry and circuit identity arguments however, it turns out that we can avoid both of these problems by measuring $\langle X_i \rangle_\theta$ and $\langle K_i \rangle_\theta$ using circuits involving a constant, small number of qubits, without the need for probabilistic state preparation.

We give a full derivation of these circuits in Appendix A.3. However, here we simply provide the algorithms necessary to measure $\langle X_i \rangle_\theta$ and $\langle K_i \rangle_\theta$ and prove their correctness via comparison with the result of the quantum-mechanical calculation in Eq. (4.1.8).

Protocol for the measurement of $\langle X_i \rangle_\theta$.

Execute the following:

1. For many times, run the simple one qubit circuit



where $U(\theta) = RY(2\theta) = \exp(-i\theta Y)$.

2. Calculate $\langle X_i \rangle_\theta$ as $\langle X_i \rangle = \langle Z_{s'} \rangle = p(s' = 0) - p(s' = 1)$.
-

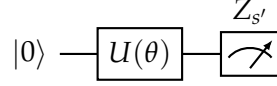
Table 4.1: Procedure for obtaining the expectation value of the local magnetic field term for the ansatz state of Eq. (4.1.2).

The correctness of the above protocol is easily confirmed by calculating $p(s' = 0) = \frac{1+2\sin\theta\cos\theta}{2}$ and $p(s' = 1) = \frac{1-2\sin\theta\cos\theta}{2}$ and so $\langle X_i \rangle_\theta = p(s' = 0) - p(s' = 1) = 2\sin\theta\cos\theta$, in agreement with Eq. (4.1.8a).

Protocol for the measurement of boundary $\langle K_i \rangle_\theta$.

Execute the following:

1. For many times, run the simple one qubit circuit



where $U(\theta) = RY(2\theta)$.

2. Calculate $\langle K_i \rangle_\theta$ as $\langle K_i \rangle = \langle Z_{s'} \rangle = p(s' = 0) - p(s' = 1)$.
-

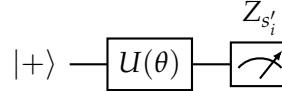
Table 4.2: Procedure for obtaining the expectation value of the boundary cluster stabilizer term ($i = 0, 1, n, n + 1$) for the ansatz state of Eq. (4.1.2).

The correctness of the above protocol is confirmed by calculating $p(s' = 0) = \cos^2 \theta$ and $p(s' = 1) = \sin^2 \theta$ and so $\langle K_i \rangle_\theta = p(s' = 0) - p(s' = 1) = \cos^2 \theta - \sin^2 \theta$, in agreement with Eq. (4.1.8b).

Protocol for the measurement of bulk $\langle K_i \rangle_\theta$.

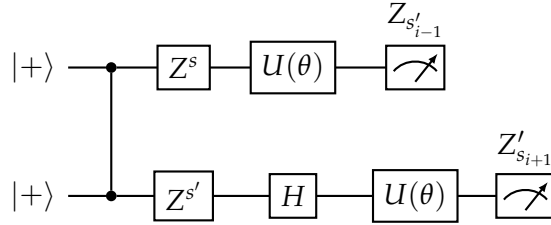
Execute the following:

1. Run the following one-qubit circuit:



where $U(\theta) = RY(2\theta)$.

2. Flip a coin; record the outcome as $s_0 = 0$ for heads, $s_0 = 1$ for tails.
3. Based on the outcomes of the one-qubit circuit and coin-flip, run the following two-qubit circuit:



4. Repeat steps 1-3 many times and compute $\langle K_i \rangle_\theta = \langle (-1)^{s'_{i-1} + s'_i + s'_{i+1}} \rangle$.
-

Table 4.3: Procedure for obtaining the expectation value of the bulk cluster stabilizer term for the ansatz state of Eq. (4.1.2).

We can again check the correctness via a probability calculation, though it is slightly more involved; the probabilities of the first circuit are given by $p(s'_3 = 0/1) = \frac{1 \pm 2 \sin \theta \cos \theta}{2}$.

Suppose the coin comes up heads (probability $\frac{1}{2}$). If $s'_3 = 0$, then $p(s'_2 = s'_4) = 1$ and $p(s'_2 \neq s'_4) = 0$. If $s'_3 = 1$, then $p(s'_2 = s'_4) = (2 \cos \theta \sin \theta)^2$ and $p(s'_2 \neq s'_4) = 1 - (2 \cos \theta \sin \theta)^2$.

Suppose instead the coin comes up tails (probability $\frac{1}{2}$). If $s'_3 = 0$, then $p(s'_2 = s'_4) = 1 - (2 \cos \theta \sin \theta)^2$ and $p(s'_2 \neq s'_4) = (2 \cos \theta \sin \theta)^2$. If $s'_3 = 1$, then $p(s'_2 = s'_4) = 0$ and $p(s'_2 \neq s'_4) = 1$.

Therefore calculating $\langle K_i \rangle$:

$$\begin{aligned}
\langle K_i \rangle_\theta &= p(s_0 = 0) [p(s'_3 = 0)p(s'_2 = s'_4|s'_3 = 0) + p(s'_3 = 1)p(s'_2 \neq s'_4|s'_3 = 1) \\
&\quad - p(s'_3 = 0)p(s'_2 \neq s'_4|s'_3 = 0) + p(s'_3 = 1)p(s'_2 = s'_4|s'_3 = 1)] \\
&\quad + p(s_0 = 1) [p(s'_3 = 0)p(s'_2 = s'_4|s'_3 = 0) + p(s'_3 = 1)p(s'_2 \neq s'_4|s'_3 = 1) \\
&\quad - p(s'_3 = 0)p(s'_2 \neq s'_4|s'_3 = 0) + p(s'_3 = 1)p(s'_2 = s'_4|s'_3 = 1)] \\
&= \frac{1}{2} [1 - (2 \cos \theta \sin \theta)^2 + (2 \cos \theta \sin \theta)^3] + \frac{1}{2} [1 - (2 \cos \theta \sin \theta)^2 - (2 \cos \theta \sin \theta)^3] \\
&= (\cos^2 \theta - \sin^2 \theta)^2
\end{aligned} \tag{4.1.9}$$

which agrees with Eq. (4.1.8b).

4.1.3 The XX-rotated cluster state

We require a different resource state to experimentally test Prediction 4 as this prediction concerns the efficiency of MBQC for a resource state with correlations between logical operations (which does not apply to the state of Eq. (4.1.2)). To this end, we consider the $n + 2$ qubit state:

$$|\Omega(\phi)\rangle = RX_1(\phi)RX_2(\phi)RX_{n-1}(\phi)RX_n(\phi) \prod_{i=1}^{n-2} RXX_{i,i+2}(\phi) |C_{n+2}\rangle \tag{4.1.10}$$

Where $RXX_{i,j}(\phi)$ denotes the two-site XX rotation:

$$RXX_{i,j}(\phi) = \exp(-i\frac{\phi}{2}X_iX_j) = \cos(\frac{\phi}{2})I_iI_j - i\sin(\frac{\phi}{2})X_iX_j. \tag{4.1.11}$$

and may be equivalently written in terms of two CNOT gates:

$$RXX_{i,j}(\phi) = H_0H_1\text{CNOT}_{0,1}R_z(\phi)\text{CNOT}_{0,1}H_0H_1. \tag{4.1.12}$$

The circuit to prepare $|\Omega(\phi)\rangle$ from the product state $|+\rangle^{\otimes n+2}$ is a series of nearest-neighbour CZ gates followed by a series of next-nearest-neighbour XX-rotations, and thus has an entanglement range of $\xi = 3$. The single-qubit X rotations on qubits on the boundary qubits are present to compensate for finite-size effects.

The X and XX rotations respect the $\mathbb{Z}_2 \times \mathbb{Z}_2$ symmetry and hence $|\Omega(\phi)\rangle$ retains the symmetry of the cluster state. The other condition required to test Prediction 4 is the convex decay of the bulk string order parameters $\sigma(d) = \sigma(k-l) = \sigma_{k,l}$ of Eq. (2.3.14). For $n+2 \geq 11$, we can do an analytical quantum-mechanical calculation (as is done in Appendix B.1) of the string order parameters, which yields:

$$\sigma(d) = \begin{cases} \cos^2(\phi) & d = 2 \\ \cos^4(\phi) & d = 4, 6, \dots \end{cases} \tag{4.1.13}$$

so $\sigma(d)$ is convex as required. In the same way that the observables relevant for the VQE energy measurements could be measured using small circuits (as shown in Section 4.1.2), a similar simplification can be done for the measurements of the SOPs which avoids the (noisier) construction of the full state. We introduce quantum protocols to measure $\sigma(d)$ for $d = 2, 4, 6$, proving their

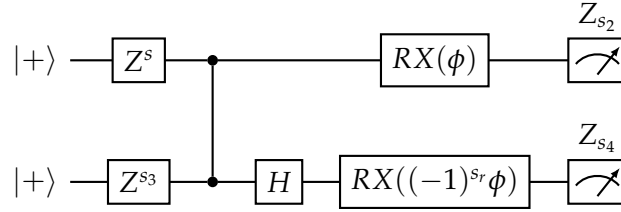
correctness via comparing with the result of the quantum-mechanical calculation. We derive these algorithms in Appendix B.2.

In order to verify the correctness of the protocols, we verify that their output agrees with Eq. (4.1.13). To this end, we calculate the probabilities of measuring a given parity in the protocol and list them in Tables 4.5, 4.7, 4.9, and use these to calculate the output.

Protocol for the measurement of $\sigma(2)$.

Execute the following:

1. Flip three coins, recording the outcomes of s, s_3, s_r as 0 for heads, 1 for tails.
2. Run the two qubit circuit:



3. Repeat steps 1-2 many times and compute $\sigma(2) = \langle (-1)^{s_2+s_3+s_4} \rangle$.
-

Table 4.4: Procedure for the $d = 2$ string order parameter for the state of Eq. (4.1.10).

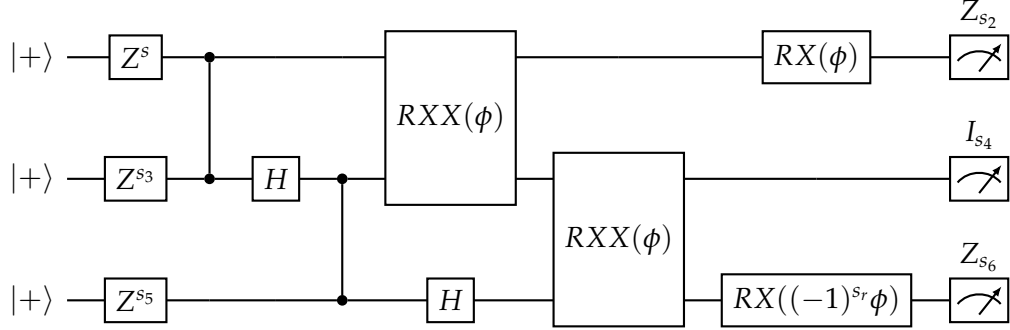
Value of s, s_3, s_r	$p(s_2 + s_3 + s_4 = 0)$	$p(s_2 + s_3 + s_4 = 1)$
000	$\cos^2 \phi$	$\sin^2 \phi$
001	1	0
010	$\cos^2 \phi$	$\sin^2 \phi$
011	1	0
100	1	0
101	$\cos^2 \phi$	$\sin^2 \phi$
110	1	0
111	$\cos^2 \phi$	$\sin^2 \phi$

Table 4.5: Probabilities for measurement of $s_2 + s_3 + s_4$ in $\sigma(2)$ measurement protocol.

Protocol for the measurement of $\sigma(4)$.

Execute the following:

1. Flip four coins, recording the outcomes of s, s_3, s_5, s_r as 0 for heads, 1 for tails.
2. Run the three-qubit circuit:



3. Repeat steps 1-2 many times and compute $\sigma(4) = \langle (-1)^{s_2+s_3+s_5+s_6} \rangle$.

Table 4.6: Procedure for the $d = 4$ string order parameter for the state of Eq. (4.1.10).

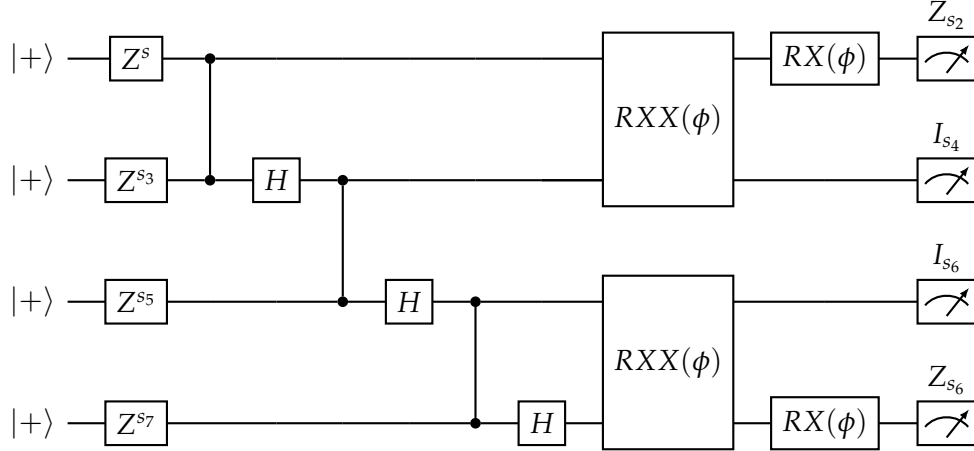
Value of s, s_3, s_5, s_r	$p(s_2 + s_3 + s_5 + s_6 = 0)$	$p(s_2 + s_3 + s_5 + s_6 = 1)$
0000	$(1 + \cos^2 2\phi)/2$	$(1 - \cos^2 2\phi)/2$
0001	$\cos^2 \phi$	$\sin^2 \phi$
0010	$(1 + \cos^2 2\phi)/2$	$(1 - \cos^2 2\phi)/2$
0011	$\cos^2 \phi$	$\sin^2 \phi$
0100	$(1 + \cos^2 2\phi)/2$	$(1 - \cos^2 2\phi)/2$
0101	$\cos^2 \phi$	$\sin^2 \phi$
0110	$(1 + \cos^2 2\phi)/2$	$(1 - \cos^2 2\phi)/2$
0111	$\cos^2 \phi$	$\sin^2 \phi$
1000	1	0
1001	$\cos^2 \phi$	$\sin^2 \phi$
1010	1	0
1011	$\cos^2 \phi$	$\sin^2 \phi$
1100	1	0
1101	$\cos^2 \phi$	$\sin^2 \phi$
1110	1	0
1111	$\cos^2 \phi$	$\sin^2 \phi$

Table 4.7: Probabilities for measurement of $s_2 + s_3 + s_5 + s_6$ in $\sigma(4)$ measurement protocol.

Protocol for the measurement of $\sigma(6)$.

Execute the following:

1. Flip four coins, recording the outcomes of s, s_3, s_5, s_7 as 0 for heads, 1 for tails.
2. Run the four-qubit circuit:



3. Repeat steps 1-2 many times and compute $\sigma(6) = \langle (-1)^{s_2+s_3+s_5+s_7+s_8} \rangle$.

Table 4.8: Procedure for the $d = 6$ string order parameter for the state of Eq. (4.1.10).

Value of s, s_3, s_5, s_7	$p(s_2 + s_3 + s_5 + s_7 + s_8 = 0)$	$p(s_2 + s_3 + s_5 + s_7 + s_8 = 1)$
0000	$(1 + \cos^2 \phi \cos 2\phi)/2$	$(1 - \cos^2 \phi \cos 2\phi)/2$
0001	$(1 + \cos^2 \phi \cos 2\phi)/2$	$(1 - \cos^2 \phi \cos 2\phi)/2$
0010	$(1 + \cos^2 \phi \cos 2\phi)/2$	$(1 - \cos^2 \phi \cos 2\phi)/2$
0011	$(1 + \cos^2 \phi \cos 2\phi)/2$	$(1 - \cos^2 \phi \cos 2\phi)/2$
0100	$(1 + \cos^2 \phi \cos 2\phi)/2$	$(1 - \cos^2 \phi \cos 2\phi)/2$
0101	$(1 + \cos^2 \phi \cos 2\phi)/2$	$(1 - \cos^2 \phi \cos 2\phi)/2$
0110	$(1 + \cos^2 \phi \cos 2\phi)/2$	$(1 - \cos^2 \phi \cos 2\phi)/2$
0111	$(1 + \cos^2 \phi \cos 2\phi)/2$	$(1 - \cos^2 \phi \cos 2\phi)/2$
1000	$(1 + \cos^2 \phi)/2$	$(1 - \cos^2 \phi)/2$
1001	$(1 + \cos^2 \phi)/2$	$(1 - \cos^2 \phi)/2$
1010	$(1 + \cos^2 \phi)/2$	$(1 - \cos^2 \phi)/2$
1011	$(1 + \cos^2 \phi)/2$	$(1 - \cos^2 \phi)/2$
1100	$(1 + \cos^2 \phi)/2$	$(1 - \cos^2 \phi)/2$
1101	$(1 + \cos^2 \phi)/2$	$(1 - \cos^2 \phi)/2$
1110	$(1 + \cos^2 \phi)/2$	$(1 - \cos^2 \phi)/2$
1111	$(1 + \cos^2 \phi)/2$	$(1 - \cos^2 \phi)/2$

Table 4.9: Probabilities for measurement of $s_2 + s_3 + s_5 + s_7 + s_8$ in $\sigma(6)$ measurement protocol.

Using that a given pattern of coin flips has probability $1/2^p$ for p coins, we can compute the expectation values using the probabilities from the three tables:

$$\sigma(2) = 4\frac{1}{8}(1-0) + 4\frac{1}{8}(\cos^2 \phi - \sin^2 \phi) = \frac{1 + \cos 2\phi}{2} = \cos^2 \phi \quad (4.1.14)$$

$$\sigma(4) = \frac{4}{16}((1-0) + (\frac{1 + \cos^2 2\phi}{2} - \frac{1 - \cos^2 2\phi}{2})) + \frac{8}{16}(\cos^2 \phi - \sin^2 \phi) = \left(\frac{1 + \cos 2\phi}{2}\right)^2 = \cos^4 \phi \quad (4.1.15)$$

$$\begin{aligned} \sigma(6) &= \frac{8}{16} \left(\frac{1 + \cos^2 \phi}{2} - \frac{1 - \cos^2 \phi}{2} \right) + \frac{8}{16} \left(\frac{1 + \cos^2 \phi \cos 2\phi}{2} - \frac{1 - \cos^2 \phi \cos 2\phi}{2} \right) \\ &= \frac{\cos^2 \phi}{2} + \frac{\cos^2 \phi \cos 2\phi}{2} = \frac{\cos^2 \phi}{2} + \frac{\cos^2 \phi (2 \cos^2 \phi - 1)}{2} = \cos^4 \phi. \end{aligned} \quad (4.1.16)$$

These with the result of the quantum-mechanical calculation in Eq. (4.1.13), verifying the correctness of the protocols.

4.2 Measurement-based quantum computing on a circuit model device

For our experiments we use quantum circuits programmed using the Qiskit [JATK⁺24] software stack, run on IBM's 127-qubit superconducting device `ibmq_quebec`, which is of the Eagle r3 processor family. The qubits in this device are laid out in a heavy-hex architecture as displayed in Fig. 4.1. Our experiments only require chains of qubits, and thus we choose high-fidelity linear subsets of the chip with length determined by minimum requirements for testing a given prediction.

The IBM devices operate based on the circuit-based model of computation, so we require a translation of the MBQC protocols into the circuit-based model. Namely, we first prepare the resource state of interest using unitary gates starting from $|0\rangle^{\otimes n+2}$ state (at this point there is no change from the MBQC model, where access to unitaries is required at the level of resource state preparation). At this state preparation stage we also choose the logical input state on qubit 0, which in our experiments we always take to be $|\overline{\mp}\rangle$. Then follows the measurement procedure - we only have access to computational/Z-basis measurements, while in MBQC we require access to X and $O(\beta)$ rotated basis measurements (for quantum wire and logical rotations), along with a state tomography measurement on the last qubit. We can simulate an X -basis measurement via a Hadamard gate preceding the computational basis measurement, and we can simulate the action of a rotated basis measurement with a preceding $RZ(\beta)$ and a Hadamard gate. State tomography measurements in an arbitrary basis can be similarly simulated via a combination of a unitary + computational basis measurement - we will be interested specifically in \overline{X} -measurements (Hadamard) and \overline{Y} -measurements, ($RZ(-\pi/2)$ + Hadamard). The final logical measurement outcome is obtained from the outcome on the last/state tomography qubit plus the measurement outcomes on the previous qubits which contribute byproduct operators, as per Eqs. (2.2.9), (2.3.5), and (2.3.6). To elucidate this discussion, we illustrate the simplest example in Fig. 4.2, where we prepare a cluster state on a chain of 5 qubits, perform a logical rotation via an effective rotated basis measurement, and then conduct state tomography on the last qubit.

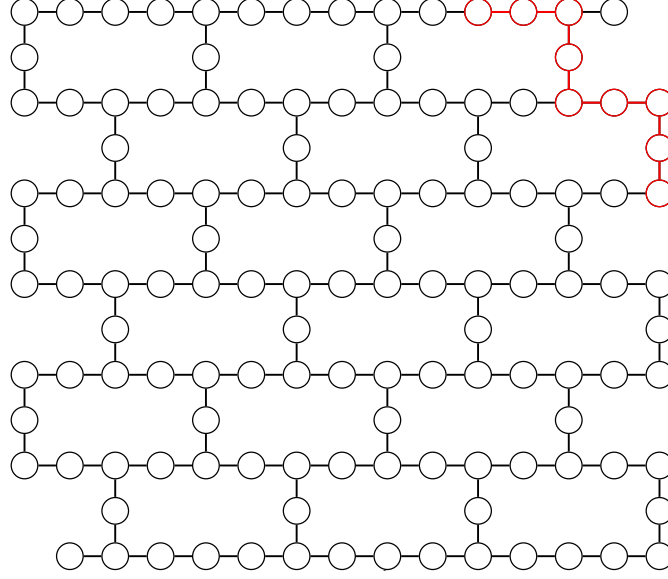


Figure 4.1: Architecture of `ibmq_quebec` chip. The chip is laid out in a 2D heavy-hex pattern, with circles corresponding to qubits and lines corresponding to connections where entangling ECR gates can be performed. For our experiments we choose linear subsets of the chip, for example the 9-qubit chain displayed in red for the rotation splitting experiments (to verify Prediction 3).

One detail of note is how the adaptivity of MBQC enters in the circuit model simulation. As previously discussed, MBQC requires the adaptive adjustment of future measurement bases depending on the past measurement outcomes, which seems to be at odds with the single round of measurement at the end of a computation. One method to resolve this discrepancy is by invoking post-selection. We fix the bases of measurement(s) and discard measurement outcomes that are incompatible with that choice, i.e. those which would have resulted in a flip of the logical rotation angle. This incurs exponential sampling overhead in the number of logical rotations, as the probability of obtaining a measurement outcome where no logical rotations are flipped is $\sim 1/2^m$ in the number of rotations m .

However, we can avoid a degree of post-selection via clever choice of input logical states and output measures. By choosing $|\overline{\mp}\rangle$ as the input state and subsequent Z-rotations, any X byproduct operators arising from measurements on qubits before the first rotated basis measurement can be absorbed into the input state, saving one layer of post-selection. The experiments to test Predictions 1-2 only contain one logical rotation on a $|\overline{\mp}\rangle$ state and hence post-selection is not required. For Prediction 3, we are interested in the (loss of) purity of the logical information, which is invariant under flips of the rotation angle (as seen in Eq. (3.3.6)) - hence by binning measurement outcomes corresponding to different rotation angle flips in measurements of $\langle \overline{X} \rangle, \langle \overline{Y} \rangle$, computing the loss in purity for each bin, and then averaging over the different bins, we avoid discarding any measurement outcomes. However note that for Prediction 4 (where logical rotations are no longer independent due to correlations in the resource state) that the loss in purity is no longer invariant under flips and so this technique does not apply. We must instead post-select.

We note that recent experimental developments have unlocked the possibility for mid-circuit

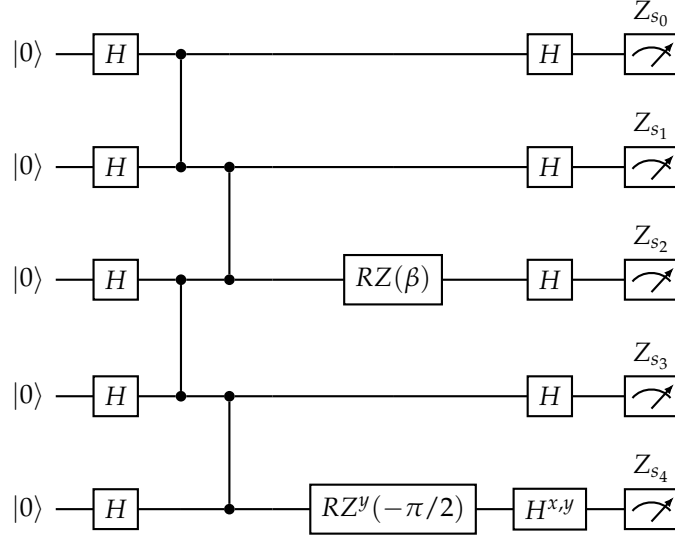


Figure 4.2: Simple (5-qubit) example of MBQC protocol on a circuit-model device. First, we prepare the resource state - here the cluster state from $|0\rangle^{\otimes 5}$ by a layer of Hadamard and nearest-neighbour CZ gates. We input a logical $|\bar{+}\rangle$ state on qubit 0. On sites 0/1/3 we simulate a X /wire-basis measurement via a Hadamard. On site 2 we simulate a rotated basis measurement by performing a $RZ(\beta)$ rotation. On the last qubit we perform state tomography of the logical qubit, applying no gates for the \bar{Z} -basis measurement, H for a \bar{X} -basis measurement, and $HRZ(-\pi/2)$ for a \bar{Y} -basis measurement. The output would then be obtained from the measurement outcomes (taking into account the byproduct operators) as $\langle \bar{Z} \rangle = \langle (-1)^{s_1+s_3+s_4} \rangle = 0$, $\langle \bar{X} \rangle = \langle (-1)^{s_0+s_2+s_4} \rangle = \cos(\beta)$, $\langle \bar{Y} \rangle = \langle (-1)^{s_0+s_1+s_2+s_3+s_4} \rangle = \sin(\beta)$. Measuring $s_1 = 1$ produces a byproduct X operator, but this can be absorbed into the input $|\bar{+}\rangle$ state, avoiding the need for post-selection.

measurement and classical feed-forward/adjustment based on those outcomes on IBM hardware, with accompanying theory developments for benchmarking and error mitigation for mid-circuit measurements [GJW⁺23], [KKT24]. This is very promising for implementations of MBQC on circuit-model devices, and we leave it to future work to test this functionality and explore the tradeoffs between gains in sampling overhead and potential decreases in fidelity due to longer circuit runtimes. However, for the current experiments of interest we are either able to avoid post-selection entirely (tests of predictions 1-3) or limit it to a manageable factor of 2x-8x (testing prediction 4) and as such are content with a single round of measurements at the end of the circuit.

4.2.1 Unitary and non-unitary operations

In our translation of MBQC protocols to a circuit-based computation that we do not have access to arbitrary unitary gates. The Eagle r3 processors use the universal gateset of $\{ECR, RZ(\beta), X, \sqrt{X}\}$. For single qubit operations, $RZ(\beta)$ allows for arbitrary Z-rotations. A Hadamard (up to a global phase) can be constructed as $H = RZ(\pi/2)\sqrt{X}RZ(\pi/2)$ which allows for arbitrary X-rotations via conjugation of RZ and thus (via the Euler decomposition) all possible single-qubit unitaries. The ECR, or echoed cross resonance gate is the native entangling gate and implements $ECR_{0,1} = \frac{1}{\sqrt{2}}(I_0X_1 - X_0Y_1)$. It is asymmetric, and (up to a global phase) equivalent to a CNOT gate up to local rotations:

$$ECR_{0,1} = RZ_0(\pi/2)\sqrt{X}_1CNOT_{0,1}X_0. \quad (4.2.1)$$

ECR gates can only be applied to connecting neighbouring qubits as depicted in Fig. 4.1 - this is an obstacle to performing long-range gates, such as the next-nearest neighbour RXX gates of the resource state of Section (4.1.10). For these, we first transport around the quantum states via the SWAP gate:

$$SWAP_{0,1} = CNOT_{0,1}CNOT_{1,0}CNOT_{0,1} \quad (4.2.2)$$

such that the qubits can be brought to neighbouring sites. We are then able to apply the desired entangling gate. Whenever we run circuits on hardware for our experiments, we thus first transpile them such that they respect the native gate set and connectivity.

The other detail of importance in our experiments is the accounting of non-unitary operations. Namely, the “gates” $T_i(\theta)$ present in ansatz state of Eq. (4.1.2) are not unitary. We thus here present a general scheme for accounting for non-unitary (local) operators via adjustment of measurement basis and post-processing. Suppose given an N -qubit state $|\psi\rangle$ we wish to apply a local non-unitary operator $T = \bigotimes_{i=0}^{n+1} T_i$ and then measure the expectation value of observable $O = \bigotimes_{i=0}^{n+1} O_i$. We observe that:

$$\langle O \rangle_{T|\psi} = \langle \psi | \left(\bigotimes_{i=0}^{n+1} T_i^\dagger \right) \left(\bigotimes_{i=0}^{n+1} O_i \right) \left(\bigotimes_{i=0}^{n+1} T_i \right) | \psi \rangle = \langle \psi | \bigotimes_{i=0}^{n+1} T_i^\dagger O_i T_i | \psi \rangle \quad (4.2.3)$$

Since each $T_i^\dagger O_i T_i$ is still Hermitian, it can be easily diagonalized and its eigenvectors are orthogonal:

$$T_i^\dagger O_i T_i = \lambda_i |\lambda_i\rangle \langle \lambda_i| + \lambda_i^\perp |\lambda_i^\perp\rangle \langle \lambda_i^\perp|. \quad (4.2.4)$$

This leads to the following protocol:

1. Prepare $|\psi\rangle$.
2. Measure m times in the bases $\left\{|\lambda_i\rangle, |\lambda_i^\perp\rangle\right\}$. Denote the outcome of run j on qubit i by λ_i^j .
3. Calculate $\langle O \rangle = \sum_{j=1}^m \prod_{i=0}^{n+1} \lambda_i^j$.

For our experiments involving the state of Eq. (4.1.2), we take $T_i = I$ on boundary sites $i = 0, n+1$ and $T_i = T_i(\theta) = \cos(\theta)I_i + \sin(\theta)X_i$ on all bulk sites. $O_i = RZ(\beta_i)X_iRZ(\beta_i)$ for sites with logical rotations and $O_i = X_i$ for all other sites (for which we do quantum wire).

4.3 Errors and mitigation

Although our experiments seek to probe logical decoherence in MBQC protocols, in tandem we must consider decoherence arising from physical device noise. In the absence of active error correction, we invoke the use of error mitigation techniques. While such techniques generally have exponential sampling scaling [QFK⁺22, SYGY24] which makes their use in large systems unfeasible, they are useful in the small-scale settings of our interest. Thus in this section we discuss various noise sources and how we can mitigate their effects.

4.3.1 Readout errors

Errors can occur in the classical readout/measurement of the quantum information, where the intended outcome of 0 can be read out as a 1 (and vice versa). Mathematically we can model these errors by considering that there is some ideal probability distribution \vec{p}_{ideal} (a vector with 2^N entries for N qubits, one for each possible bit string) which gets modified by a stochastic noise matrix M , leading to an experimental measurement of the noisy distribution $\vec{p}_{\text{noisy}} = M\vec{p}_{\text{ideal}}$. If we were able to find the inverse of the noise matrix, also known as the assignment matrix $A = M^{-1}$, we would then be able to determine the ideal probability distribution by $\vec{p}_{\text{ideal}} = A\vec{p}_{\text{noisy}}$. The goal of measurement error mitigation is thus to approximate A .

To this end we use the M3 error mitigation package [NKSG21]. We first approximate the measurement errors as independent, such that there are no correlated readout errors between qubits. Thus we can approximate M as the tensor product of single-qubit noise matrices $M = \bigotimes_i M_i$, where:

$$M_i = \begin{bmatrix} p_i(0|0) & p_i(1|0) \\ p_i(0|1) & p_i(1|1) \end{bmatrix} \quad (4.3.1)$$

where $p_i(k|j)$ denotes the probability that outcome k was measured when state i was supposed to be measured (on qubit i). The inverse of the above (the assignment matrix) is:

$$A_i = \frac{1}{p_i(0|0)p_i(1|1) - p_i(0|1)p_i(1|0)} \begin{bmatrix} p_i(1|1) & -p_i(1|0) \\ -p_i(0|1) & p_i(0|0) \end{bmatrix} \quad (4.3.2)$$

The M3 package estimates the p_i via a “balanced” method of sampling the measurement statistics of $2N$ bit strings (out of 2^N possible) where each qubit has N strings for which 0 is prepared and N for which 1 is prepared. This has the benefit of being less expensive to measure than running $2N$ estimation circuits (one for each of the N qubits), while being more robust to state

preparation errors than the 2 circuit estimation method of preparing/measuring $|0\rangle^{\otimes n}$ and $|1\rangle^{\otimes n}$. For applying readout mitigation, we can then compute the full n -qubit assignment matrix from the p_i s from $A = \otimes_i A_i$. However for larger systems this construction can be costly (as it involves the construction and then application of a $2^N \times 2^N$ matrix). As such, M3 takes a more efficient approach of restricting the assignment matrix to the subspace of bit strings observed in \vec{p}_{noisy} and constructing the restricted assignment matrix via iterative methods to approximate \vec{p}_{ideal} .

For `ibm_quebec`, measurement readout errors probabilities are on the order of $\sim 10^{-2}$ per qubit, which can be significantly suppressed via the discussed method.

4.3.2 Gate errors

When performing quantum gates on our qubits, the logical action can deviate from its intended value in two ways. The first is via a coherent error, where there is some unintended unitary error, for example an Z rotation:

$$\rho \mapsto \mathcal{E}(\rho) = RZ(\delta\beta)\rho RZ(-\delta\beta) \quad (4.3.3)$$

The second is via an incoherent error, where there is some probabilistic Pauli transformation of the state, e.g. via the partially depolarizing channel of strength p :

$$\rho \mapsto \mathcal{E}(\rho) = (1-p)\rho + \frac{p}{3}(X\rho X + Y\rho Y + Z\rho Z). \quad (4.3.4)$$

The error rate of a noise map \mathcal{E} can be quantified via an average error rate [WE16]:

$$r(\mathcal{E}) = 1 - \int d\psi F_{I,\mathcal{E}}(|\psi\rangle\langle\psi|) \quad (4.3.5)$$

where the fidelity $F_{\mathcal{A},\mathcal{B}}(\rho)$ quantifies the distinguishability of maps \mathcal{A}, \mathcal{B} when acted on state ρ [MBKE11]:

$$F_{\mathcal{A},\mathcal{B}}(\rho) = \text{Tr}(\mathcal{A}(\rho)\mathcal{B}(\rho)). \quad (4.3.6)$$

The error rate can also be quantified via a worst-case error rate:

$$\epsilon(\mathcal{E}) = \sup_{\psi} \|\mathcal{E} \circ I_d - I_{d^2}(\psi)\|_1 \quad (4.3.7)$$

with d the dimension of the space upon which \mathcal{E} acts. Given a coherent and incoherent error channel with the same average error rate r , the incoherent error channel is much preferable experimentally as their worst-case error is greatly suppressed and the average error rate increases linearly in time for incoherent errors but quadratically for coherent ones⁷ [WE16].

Experimentally, the dominant source of gate error comes from entangling gates. We can also modify Eq. (4.3.5) to quantify the average gate fidelity, obtained by comparing the ideal operation of a gate \mathcal{U} with its noisy counterpart \mathcal{E} :

$$r(\mathcal{U}, \mathcal{E}) = 1 - \int d\psi F_{\mathcal{U},\mathcal{E}}(|\psi\rangle\langle\psi|). \quad (4.3.8)$$

⁷Although not relevant for the current work, incoherent errors also have higher fault tolerance thresholds and are thus also preferable from a fault tolerance lens.

Benchmarks of `ibm_quebec` suggest that the average gate error for 2-qubit/ECR gates is on the order of $\sim 10^{-2}$ while the average single-qubit gate error is on the order of $\sim 10^{-4}$. We thus neglect the errors coming from single qubit operations, and wish to mitigate the errors arising from two-qubit gates.

We do this in the form of randomized compilation/Pauli twirling [WE16], where coherent errors get mapped to incoherent errors. For our discussion it suffices to consider twirling of CNOT/CZ gates (as we may twirl these gates before compiling to the native gate set). There are 16 two-qubit Pauli strings, and thus 16 pairs (P_i, P_j) which leave the logical action of CNOT/CZ invariant, e.g. $I_0 X_1 CZ_{0,1} Z_0 X_1 = CZ_{0,1}$. All combinations of these are given in Table 4.10 below.

Pre-gate	Post-CZ	Post-CNOT
II	II	II
IX	ZX	IX
IZ	IZ	ZZ
IY	ZY	ZY
XI	XZ	XX
XX	YY	XI
XZ	XI	YY
XY	YX	YZ
ZI	ZI	ZI
ZX	IX	ZX
ZZ	ZZ	IZ
ZY	IY	IY
YI	YZ	YX
YX	XY	YI
YZ	YI	XY
YY	XX	XZ

Table 4.10: Pauli twirling of CZ and CNOT gates. The leftmost column indicates the two-qubit Pauli string before the two-qubit gate, and the second/third columns indicate the two-qubit Pauli string to place after the respective two-qubit gate such that the logical action of the gate is left invariant, such as (for the last row) $Y_0 Y_1 CZ_{0,1} X_0 X_1 = CZ_{0,1}$ and $Y_0 Y_1 CNOT_{0,1} X_0 Z_1 = CNOT_{0,1}$.

We can thus take every CNOT/CZ that appears in our circuit and randomly compile/replace it with one of the 16 Pauli twirled versions, and then average over these compilations. Each circuit in the average has the identical logical action, but the coherent errors associated with the two-qubit gates gets mapped to an incoherent Pauli noise channel [WE16]. Thus we are able to mitigate coherent errors from two-qubit gates.

4.3.3 Thermal relaxation errors

Even when not performing logical operations on qubits, they still interact with their environment. The thermal relaxation error associated with this open system interaction can be modelled as a combination of amplitude damping and phase damping. Suppose we have the single-qubit

density matrix:

$$\rho = \begin{bmatrix} a & b \\ b^* & (1-a) \end{bmatrix} \quad (4.3.9)$$

Under amplitude damping of strength γ , ρ becomes [NC10]:

$$\begin{bmatrix} a & b \\ b^* & (1-a) \end{bmatrix} \mapsto \begin{bmatrix} 1 - (1-\gamma)(1-a) & b\sqrt{1-\gamma} \\ b^*\sqrt{1-\gamma} & (1-a)(1-\gamma) \end{bmatrix} \quad (4.3.10)$$

or in the Bloch sphere representation:

$$(r_x, r_y, r_z) \mapsto (r_x\sqrt{1-\gamma}, r_y\sqrt{1-\gamma}, \gamma + r_z(1-\gamma)). \quad (4.3.11)$$

In a physical system, γ is often parametrized by the exponential decay $\gamma = 1 - \exp(-t/T_1)$ where T_1 is the time constant of amplitude damping, wherein the above equations become:

$$\begin{bmatrix} a & b \\ b^* & (1-a) \end{bmatrix} \mapsto \begin{bmatrix} 1 - e^{-t/T_1}(1-a) & be^{-t/2T_1} \\ b^*e^{-t/2T_1} & (1-a)e^{-t/T_1} \end{bmatrix} \quad (4.3.12)$$

$$(r_x, r_y, r_z) \mapsto (r_xe^{-t/2T_1}, r_ye^{-t/2T_1}, 1 + (r_z - 1)e^{-t/T_1}) \quad (4.3.13)$$

Amplitude damping can be understood as the system relaxing to the ground state $|0\rangle$. The other form of damping is (pure) phase damping. Under phase damping of strength λ , the density matrix is mapped to:

$$\begin{bmatrix} a & b \\ b^* & (1-a) \end{bmatrix} \mapsto \begin{bmatrix} a & b(1-\lambda) \\ b^*(1-\lambda) & (1-a) \end{bmatrix} \quad (4.3.14)$$

or in the Bloch sphere representation:

$$(r_x, r_y, r_z) \mapsto (r_x\sqrt{1-\lambda}, r_y\sqrt{1-\lambda}, r_z) \quad (4.3.15)$$

In a physical system, λ is often parametrized by the exponential decay $\lambda = 1 - \exp(-t/T_\varphi)$ where T_φ is the time constant of (pure) phase damping. The above equations then become:

$$\begin{bmatrix} a & b \\ b^* & (1-a) \end{bmatrix} \mapsto \begin{bmatrix} a & be^{-t/T_\varphi} \\ b^*e^{-t/T_\varphi} & (1-a) \end{bmatrix} \quad (4.3.16)$$

$$(r_x, r_y, r_z) \mapsto (r_xe^{-t/2T_\varphi}, r_ye^{-t/2T_\varphi}, r_z) \quad (4.3.17)$$

Pure phase damping can be understood as the decoherence of the phase information between $|0\rangle, |1\rangle$, or equivalently by the shrinking of the x-y plane projection of the Bloch sphere vector. Combining these two error channels, we obtain:

$$\begin{bmatrix} a & b \\ b^* & (1-a) \end{bmatrix} \mapsto \begin{bmatrix} 1 - e^{-t/T_1}(1-a) & be^{-t/2T_1}e^{-t/T_\varphi} \\ b^*e^{-t/2T_1}e^{-t/T_\varphi} & (1-a)e^{-t/T_1} \end{bmatrix}. \quad (4.3.18)$$

It is common to define the off-diagonal decay time constant T_2 via:

$$e^{-t/T_2} := e^{-t/2T_1}e^{-t/T_\varphi} \quad (4.3.19)$$

so in terms of the T_1/T_2 decay times:

$$\begin{bmatrix} a & b \\ b^* & (1-a) \end{bmatrix} \mapsto \begin{bmatrix} 1 - e^{-t/T_1}(1-a) & be^{-t/T_2} \\ b^*e^{-t/T_2} & (1-a)e^{-t/T_1} \end{bmatrix}. \quad (4.3.20)$$

Each qubit in our experiments can be modelled as undergoing the above thermal relaxation error channel. Concretely, the qubits of `ibm_quebec` have a median T_1 time of $\sim 300\mu s$ and a median T_2 time of $\sim 150\mu s$.

The running times of the components of our circuit are 0ns for RZ gates, 60.444ns for X and \sqrt{X} gates, 593.778ns for ECR gates, and 835.556ns for readout, with the latter two being the dominant contributions to the execution time. Roughly, experiments for Predictions 1-3 (with two layers of ECR (CZ) gates to prepare the state) have a runtime of $\sim 2\mu s$ and experiments for Prediction 4 (with two layers of ECR (CZ) gates to prepare the cluster state, and 2 sets of SWAPs (3 ECRs) and RXX (2 ECRs) - 12 layers of ECRs in total) have a runtime of $\sim 8\mu s$. For the first set of experiments we have $e^{-t/T_1} \approx e^{-t/T_2} \approx 0.99$ and for the last set of experiments we have $e^{-t/T_1} \approx 0.97$ and $e^{-t/T_2} \approx 0.95$. We do not actively mitigate these errors, but consider them a sub-leading effect given that our experiments consist of short-depth circuits.

Chapter 5

Results

In this section we go through the results of the four experimental tests of Chapter 3. All data, calibrations, and code for running experiments and post-processing data are available at [Wei24].

We begin by discussing the results of the variational state preparation for the resource state of Eq. (4.1.2) (approximating the ground states of Eq. (2.3.13)) for the tests of Predictions 1-3. The experimental measurements of the energy and the subsequent optimization for the variational parameter in Fig. 5.1 below.

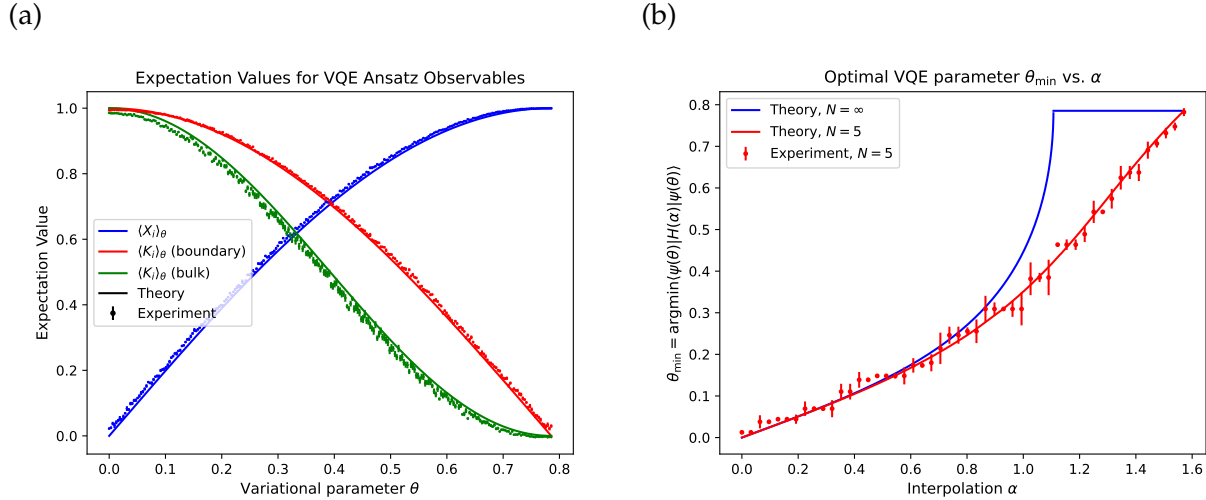


Figure 5.1: Experimental results for variational state preparation. (a) Measurements of the local magnetic field $\langle X \rangle_i$ and cluster state stabilizer terms $\langle K \rangle_i$ using protocols of Tables 4.1-4.3. Solid lines correspond to theory (Eq. (4.1.8)) and dots correspond to experimental measurement. Measurements were taken on 1/2-qubit subsets of `ibm_quebec` for 250 uniformly spaced θ , using readout error mitigation and Pauli twirling. 8 experiments with 5000 shots were taken and averaged, with error bars corresponding to standard error of the mean. (b) Dependence of variational parameter θ of Eq. (4.1.2) on the interpolation parameter α of Eq. (2.3.13) for an $N = 5$ chain. Theory values for $N = 5, \infty$ are plotted for comparison. Experimental points were obtained by minimizing the expectation value of the energy using the data of (a) for a given value of α . Error bars are estimated via determining of the propagated error in the minimized energy and computing the range of θ for which the expectation value falls below the minimum energy + uncertainty. The theory result for $N = 5$ is computed by minimizing over the theory curves in (a), and for $N = \infty$ is computed analytically in Appendix A.4.

We observe the experimental measurements of the three energy terms are in good agreement with the theory, producing a high-accuracy result for the optimal variational parameter. Although the plot takes a chain length of 5, an analogous plot of θ_{\min} vs. α can be obtained for chain of 9 qubits, which we use for experimental tests of Prediction 3. The curve for θ_{\min} is smooth for the finite chain, but exhibits a phase transition in the $N = \infty$ limit. This phase transition occurs at $\alpha = \arctan(2)$ rather than $\alpha = \pi/4$ for the true ground states of the interpolation Hamiltonian.

5.1 Decoherence

For various values of the interpolation α we find the optimal θ_{\min} for a 5-qubit chain, as shown in Fig. 5.1(b). For each state, we then start with a logical input of $|\overline{\mp}\rangle$ on qubit 0, carry out a logical rotation by angle β (Z-rotation) on qubit 2 and perform state tomography on qubit 4 to measure $\langle\overline{X}\rangle/\langle\overline{Y}\rangle$. We use the protocol of Section 4.2.1 to account for the non-unitary operations. The circuits we run are identical to Fig. 4.2 up to the modification of $RZ(\beta)$ on qubit 2 due to $T(\theta)$. We can plot $\langle\overline{Y}\rangle$ vs. $\langle\overline{X}\rangle$ for the output logical state, yielding the results seen in Fig. 5.2.

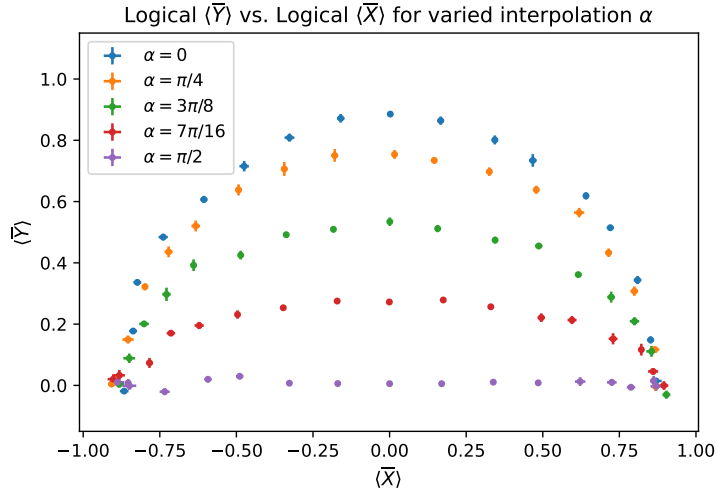


Figure 5.2: Experimental result for test of Prediction 1 (Decoherence). $\langle\overline{Y}\rangle$ and $\langle\overline{X}\rangle$ of the encoded logical qubit were measured for varying logical rotation angles β . The resource state used was Eq. (4.1.2), approximating ground states of the interpolation Hamiltonian Eq. (2.3.13) for 5 values of α . Measurements were taken on a 5-qubit subset of `ibmq_quebec` for 17 uniformly spaced β between 0 and π , using readout error mitigation and Pauli twirling. 8 experiments with 10000 shots were taken and averaged, with error bars corresponding to standard error of the mean.

In the experimental data we observe a slight suppression of $\langle\overline{X}\rangle$ and $\langle\overline{Y}\rangle$ due to device noise (predominantly from incoherent 2-qubit gate errors) which does not respect the symmetry. The noise is evident (for example) in how $\langle\overline{X}\rangle = 0$ is not achieved for $\beta = 0$ for any of the states. As the rotation angle interpolates goes from symmetry respecting ($\beta = 0$) to maximally symmetry breaking ($\beta = \pi/2$) we see an increase in the logical decoherence, with the points being pushed

further into the interior of the Bloch sphere. We observe that the semi-major axes of the ellipses are ~ 1 regardless of the value of α (and hence the computational order parameter ν). As we increase α and decrease ν , we see the reduction in $\langle \bar{Y} \rangle$ and the semi-minor axes of the ellipses. The semi-minor axis is maximal for $\alpha = 0$ (for which we have the cluster state with $\nu = 1$) and is minimal for $\alpha = \pi/2$ (where we have the product state with $\nu = 0$). Thus, the above data confirms the prediction of Prediction 1 - the proceeding test of Prediction 2 will make the measures of decoherence more quantitative by extracting the computational order parameters ν .

5.2 Equivalence of string order and computational order

For the test of Prediction 3.2, we can use the exact same experiment as the last; we divide $\langle \bar{Y} \rangle$ by $\langle \bar{X} \rangle$ and plot the result against $\tan(\beta)$. This yields Fig. 5.3 below.

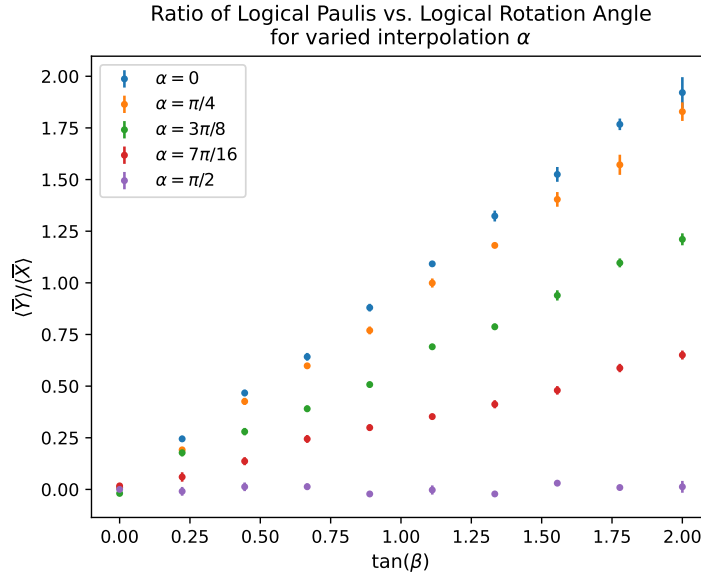


Figure 5.3: Plot of ratio of logical observables to extract computational order parameter. $\langle \bar{Y} \rangle$ and $\langle \bar{X} \rangle$ of the encoded logical qubit were measured for varying logical rotation angles β . The resource state used was Eq. (4.1.2), approximating ground states of the interpolation Hamiltonian Eq. (2.3.13) for 5 values of α . Measurements were taken on a 5-qubit subset of `ibm_quebec` for 10 uniformly spaced $\tan \beta$ between 0 and 2, using readout error mitigation and Pauli twirling. 8 experiments with 10000 shots were taken and averaged, with error bars corresponding to standard error of the mean. The curves of $\langle \bar{Y} \rangle / \langle \bar{X} \rangle$ vs. $\tan(\beta)$ are linear and the computational order parameter for a given α can be extracted as the slope of the line.

Via least-squares fitting to the linear data, we can obtain the computational order parameter ν for a given α (a given θ_{\min}) as the slope of the data as per Eq. (3.2.2). We can then compare against the measurement of the string order parameter $\sigma_2(g_{01}) = \langle \psi(\theta) | Z_2 X_3 Z_4 | \psi(\theta) \rangle$, which is obtained from the measurement of the boundary $\langle K_i \rangle_\theta$ during the VQE. Plotting the two measurements as a function of α , we obtain Fig. 5.4.

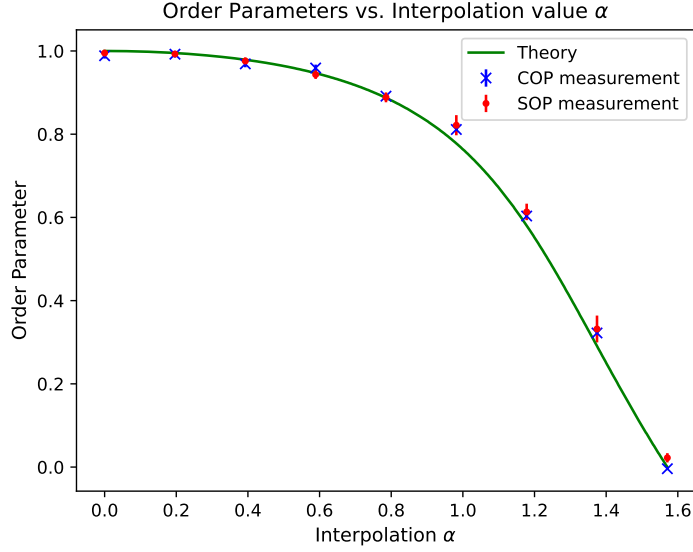


Figure 5.4: Experimental test of Prediction 2 (String order is computational order). We plot the computational order parameters (blue) obtained from the MBQC protocol (slopes of Fig. 5.3 with some additional points) along with the independent measurement of the string order parameters (red) obtained from the VQE protocol (boundary $\langle K_i \rangle_\theta$ of Fig. 5.1 (a)). Measurements were taken for 10 points of evenly spaced α from 0 (cluster state) to $\pi/2$ (product state). Error bars on the COP measurement come from the variance in the optimal fit parameters of the least squares fitting. Error bars on the SOP measurement come from combining statistical error in the $\langle K_i \rangle_\theta$ measurement with the range of $\langle K_i \rangle_\theta$ coming from the error/range in θ_{\min} for a given α . The theory curve (green) was obtained by optimizing over and calculating the SOP for a given α using the analytical expressions of Eq. (4.1.8b).

Comparing the SOP and COP measurements, we can see that across various values of the interpolation α that they agree (within statistical error). There is a slight overestimate of the theory value at points due to experimental error (both in the VQE optimization and in the COP/SOP measurements), but overall there is agreement between the two experiments and with theory. We thus have confirmed Prediction 2, via experimental demonstration that the string order and computational order are equivalent.

5.3 Rotation splitting

We use the VQE data to find the optimal θ_{\min} for interpolation $\alpha = \pi/3$ for a 9-qubit chain. We choose $\alpha = \pi/3$ as it is close to the phase transition of the variational ansatz state Eq. (4.1.2) at $\alpha = \arctan(2)$, thus maximizing the (small) decoherence effect we wish to measure while remaining within the “cluster phase”. We find the optimal variational parameter of $\theta_{\min} = 0.909$. For this resource state we compare three MBQC protocols with various splittings of a Z-rotation - in the first we do a single rotation on qubit 2 by angle β , in the second we do two rotations on qubits 2/4 by angle $\beta/2$ and in the last we do three rotations on qubit 3 by angle $\beta/3$ on qubits 2/4/6. We start with a logical input of $|\overline{+}\rangle$ on qubit 0 and perform state tomography on qubit 8

to measure $\langle \bar{X} \rangle / \langle \bar{Y} \rangle$. We use the protocol of Section 4.2.1 to account for the non-unitary operations. The circuit we run is that of Fig. 5.5.

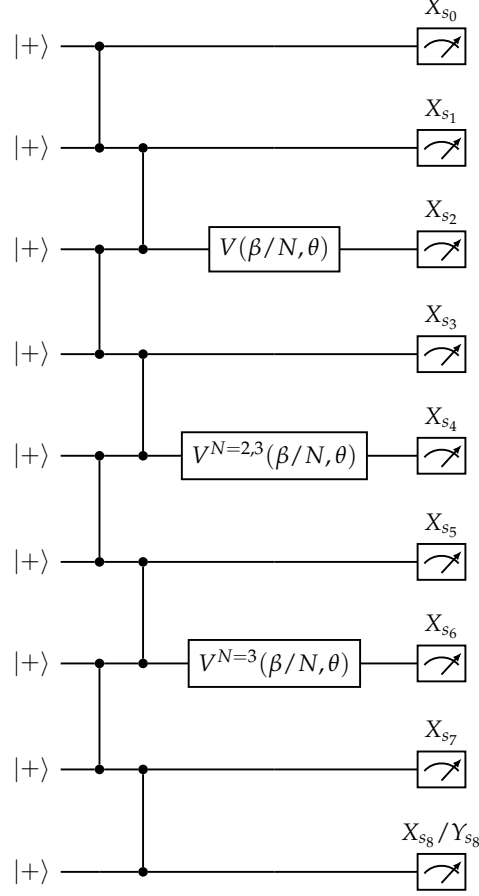


Figure 5.5: Circuits for rotation splitting experiments. We prepare the cluster state, with logical input of $|\bar{+}\rangle$. We perform up to three logical rotations on qubits 2/4/6, depending on whether we split the total rotation angle into 1/2/3 operations. The logical rotations are modified depending on the variational parameter θ to measure in the eigenbasis of $T_i(\theta)RZ_i(\beta/N)X_iRZ_i(\beta/N)T_i(\theta)$. For $\alpha = \pi/3$ on a 9-qubit chain, it is found via the VQE protocol to be $\theta_{\min} = 0.909$. We then perform state tomography on the last qubit, and can compute the logical output observables $\langle \bar{X} \rangle, \langle \bar{Y} \rangle$ from Eq. (2.3.6) combined with the non-unitarity accounting of Section 4.2.1.

We can compute the loss in purity according to Eq. (3.3.1):

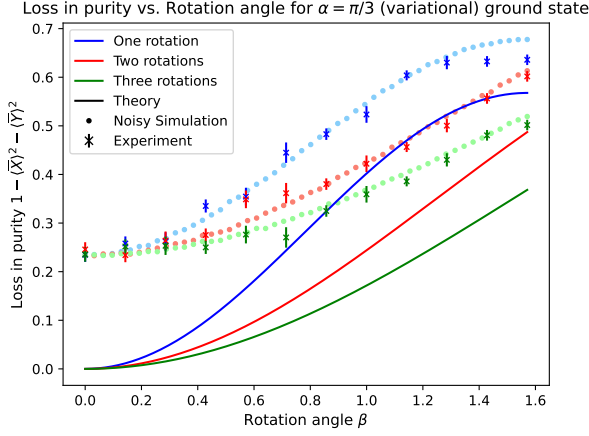
$$\text{LP} = 1 - \langle \bar{X} \rangle^2 - \langle \bar{Y} \rangle^2 - \langle \bar{Z} \rangle^2 \quad (5.3.1)$$

noting that $\langle \bar{Z} \rangle$ does not need to be measured as it is always zero for an input state of $|\bar{+}\rangle$ with Z-rotations. Repeating this process while varying the total logical rotation angle, we obtain the experimental data in Fig. 5.6. We compare the experimental results with the analytic expressions in Eq. (3.3.7), as well as a noisy simulation of the circuits, where the noise model consists of (uniform) depolarizing noise of strength p applied to all 2-qubit gates:

$$\mathcal{E}(\rho) = (1 - p)\rho + \frac{p}{4}I. \quad (5.3.2)$$

We repeat the simulation for various values of p and choose the one which minimizes the least-squares distance to the experimental data.

(a)



(b)

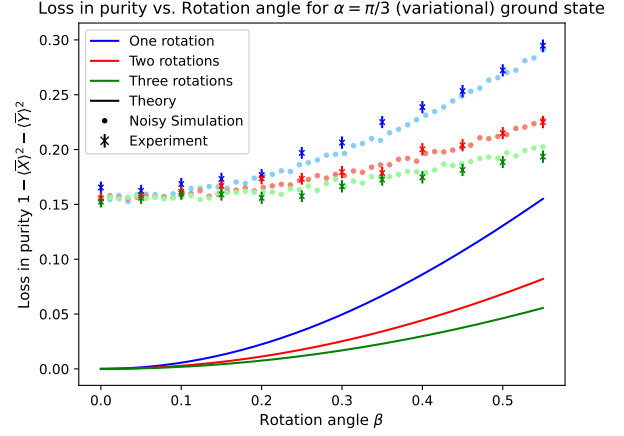


Figure 5.6: Rotation splitting coarse experimental data (crosses) and comparison with theory (curves) and noisy simulation (dots). The resource state is the ansatz state of Eq. (4.1.2) optimized for interpolation parameter $\alpha = \pi/3$. We plot the loss in purity of the logical state, comparing protocols where the rotation is performed on one site (blue) vs. split across two (red)/three (green) sites. Measurements were taken on a 9-qubit subset of `ibm_quebec`, using readout error mitigation and Pauli twirling. Theory curves are obtained from Eq. (3.3.7) and (4.1.8b). Noisy simulation points are obtained by running the circuits with 2-qubit depolarizing noise of strength p . (a) β is taken to be uniformly spaced between 0 and $\pi/2$. 12 experiments with 10000 shots were taken and averaged, with error bars corresponding to standard error of the mean. The simulation depolarizing noise strength is $p = 0.0165$, with 4 million shots. (b) β is taken to be uniformly spaced between 0 and 0.55 (small angles). 240 experiments with 10000 shots were taken and averaged, with error bars corresponding to standard error of the mean. The simulation depolarizing noise strength is $p = 0.0105$, with 4 million shots.

We can see from the experimental data that the behaviour of the loss in purity curves as a function of β are nicely reproduced in experiment. However, compared to the theory they are shifted up and compressed due to device noise. The one-parameter noise model of 2-qubit depolarizing noise channels of uniform strength fits the data well in both cases (though with different strengths of the channel), and lines up well with device benchmarks of median ECR errors on the order of $\sim 1\%$. Differences in the ECR error rates between (a) and (b) (1.65% vs. 1.05%) arises from the fact that the datasets were taken at different times and that the device noise drifts in time. In order to test Prediction 3, we take the small-angle loss in purity data of (b) and extract the curvatures through least squares fitting with fitting function:

$$f(\beta) = c\beta^2 + b \quad (5.3.3)$$

This yields Fig. 5.7.

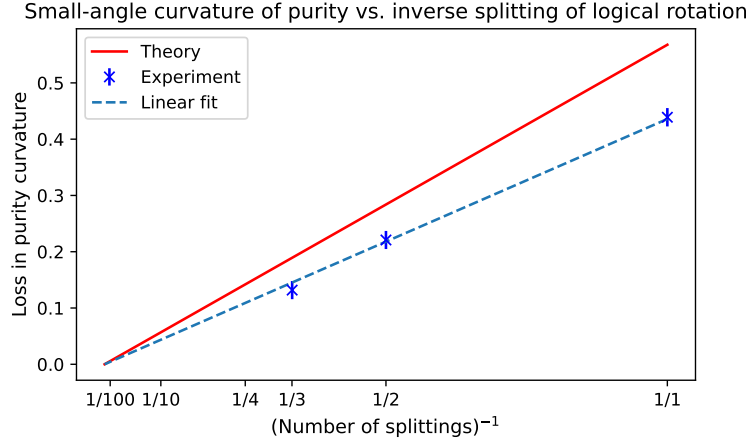


Figure 5.7: Experimental test of Prediction 3 (Rotation splitting). Experimental purity curvatures are obtained from a least-squares quadratic fit of the experimental data of Fig. 5.6(b) and plotted against the (inverse) number of splittings of the logical rotation. Error bars are from the variance in the optimal fit parameters of the least squares fitting. Linear fit is obtained by least-squares fit to the three curvature points, with slope of $m = 0.436 \pm 0.014$. Theory curve is a plot of Eq. (3.3.9) with slope of $m = 0.568$.

We wish to experimentally verify the loss in purity scaling of (3.3.9), which (for a total logical rotation β split into m parts) predicts $LP_m = \frac{1-\sigma^2}{m} \beta^2$. Thus plotting the small angle curvature against $\frac{1}{m}$ we expect to see a straight line with slope $1 - \sigma^2$. For $\alpha = \pi/3$ we can calculate σ from Eq. (4.1.8b) to be $\sigma = 0.657$ and hence a predicted slope of $m = 1 - (0.657)^2 = 0.568$. While the best-fit slope of the experimental purity curvatures is smaller than predicted ($m = 0.436 \pm 0.014$), the experimental data (up to statistical error) nevertheless fits a straight line. This demonstrates the $\frac{1}{m}$ scaling of the small-angle loss in purity, confirming Prediction 3.

5.4 Counterintuitive is the most efficient

We consider the XX-rotated cluster state $|\Omega(\phi)\rangle$ of Eq. (4.1.10) on 11 qubits. For our experiments we take $\phi = \pi/4$ as this is the value for which the decay of the string order parameter $\sigma(2) - \sigma(d = 4, 6, \dots) = \cos^4(\phi) - \cos^2(\phi) = \cos^2(\phi) \sin^2 \phi$ is maximized. We begin by experimentally measuring (via the protocols of Table 4.4, 4.6, 4.8) the string order parameters to verify that their decay as a function of length is convex, as is a precondition of the prediction. The results of this are given in Fig. 5.8.

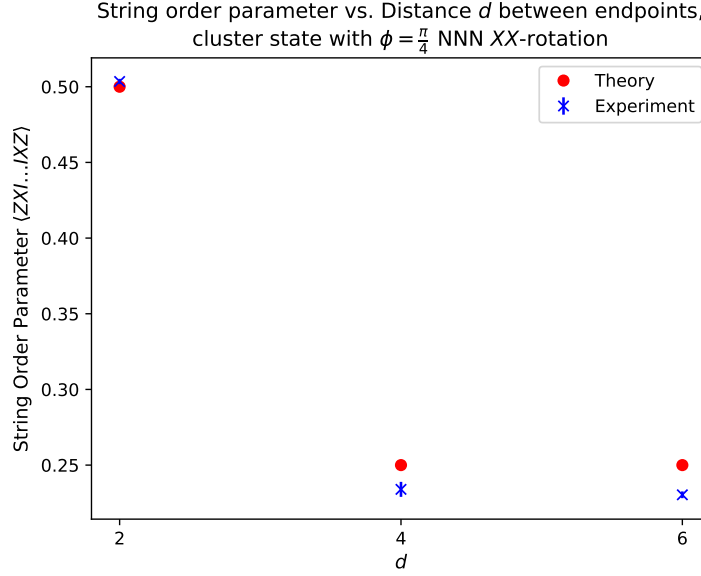


Figure 5.8: Experimental test of the convexity of the string order parameters $\sigma(d)$. We run the protocols of 4.4, 4.6, 4.8 for $\phi = \pi/4$. Measurements were taken on 2-4 qubit subsets of `ibm_quebec`, using readout error mitigation and Pauli twirling. 36 experiments with 10000 shots were taken and averaged, with error bars corresponding to standard error of the mean. Experimental results (blue) were compared with the theory result (red) of $\sigma(2) = \cos^2(\pi/4) = 1/2$ and $\sigma(4) = \sigma(6) = \cos^4(\pi/4) = 1/4$.

We can see that up to a suppression of the measured values of $\sigma(4)$ and $\sigma(6)$ due to device noise (these two protocols have 6-7x the number of two-qubit gates than the protocol for $\sigma(2)$), the experimental measurements agree with the theory prediction, and the decay of the string order parameters is observed to be convex as is required.

We now proceed to the experimental test of Prediction 4. We prepare $|\Omega(\phi = \pi/4)\rangle$ on an 11-qubit chain, and compare three MBQC protocols with various splittings of a Z -rotation - in the first we do two rotations on qubits 2/4 ($\Delta = 2$) by angle $\beta/2$, in the second we do two rotations on qubits 2/8 ($\Delta = 6$) by angle $\beta/2$, and in the last we do four rotations on qubits 2/4/6/8 ($\Delta = 2$) by angle $\beta/4$. We start with a logical input of $|\overline{+}\rangle$ on qubit 0 and perform state tomography on qubit 8 to measure $\langle \overline{X} \rangle / \langle \overline{Y} \rangle$. The circuit we run is that of Fig. 5.9.

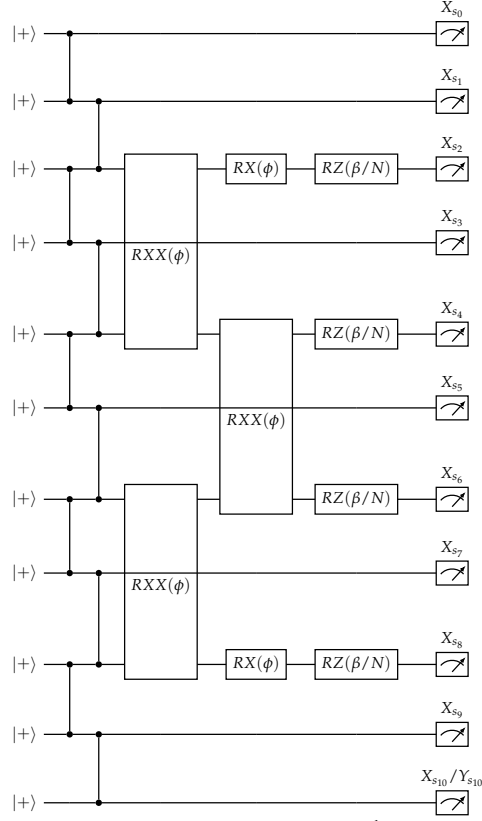


Figure 5.9: Circuits for counterintuitive regime experiments. We prepare the cluster state, with logical input of $|\overline{+}\rangle$, and modify it via next-nearest-neighbour XX -rotations to prepare $|\Omega(\phi)\rangle$ as per Eq. (4.1.10). On sites where we perform quantum wire/measurement in X we can omit the X -rotations as they commute through the measurement. We compare the effect of two split close ($\Delta = 2$) logical rotations on qubits 2/4, two split far ($\Delta = 6$) logical operations on qubits 2/8, and four split maximally packed/divided ($\Delta = 2$) logical operations on qubits 2/4/6/8. We then perform state tomography on the last qubit, and can compute the logical output observables $\langle \overline{X} \rangle, \langle \overline{Y} \rangle$ from Eq. (2.3.6).

We can compute the loss in purity (as in the rotation splitting experiment) according to Eq. (3.3.1) from the experimentally measured $\langle \bar{X} \rangle, \langle \bar{Y} \rangle$. Note that unlike the rotation splitting experiment, calculating the output logical observables here requires post-selection. This is because the invariance under flips of the rotation angle in the LP expression of Eq. (3.3.7) (obtained by composing independent logical operations) no longer holds when one considers correlated logical operations. Thus we post select on $s_3 = 0$ for the two $\Delta = 2$ rotation protocol, $s_3 + s_5 + s_7 \bmod 2 = 0$ for the two $\Delta = 6$ rotation protocol, and $s_3 = s_5 = s_7 = 0$ for the four $\Delta = 2$ rotation protocol.

Computing the loss in purity for the three protocols for various values of the total logical rotation angle β , we obtain the experimental data in Fig. 5.10. We compare the experimental results with the analytic expressions calculated in Appendix B.3, as well as a noisy simulation of the circuits, where the noise model consists of (uniform) depolarizing noise of strength p applied to all 2-qubit gates. We repeat the simulation for various values of p and choose the one which minimizes the least-squares distance to the experimental data.

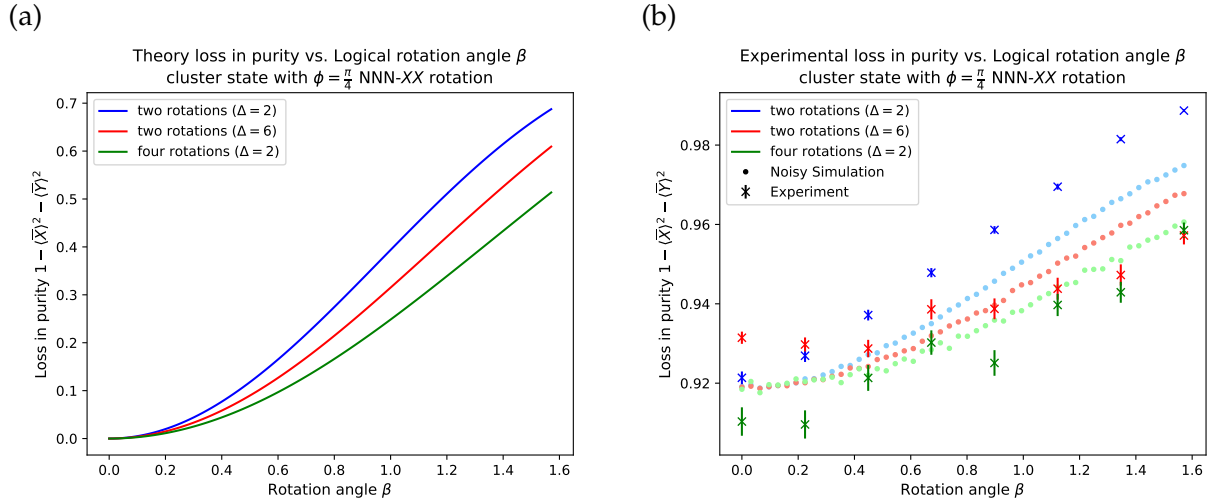


Figure 5.10: Experimental test of Prediction 4 (The counterintuitive regime). The loss in purity for 2 $\Delta = 2$ (blue), 2 $\Delta = 6$ (red), 4 $\Delta = 2$ (green) subdivided rotations as a function of total rotation angle β is compared for the XX-rotated cluster state of Eq. (4.1.10) with $\phi = \pi/4$. (a) Theory curves for loss in purity for as calculated in Appendix B.3. (b) Experimental data (crosses) and comparison with noisy simulation (dots). Measurements were taken on an 11-qubit subset of `ibmq_belem`, using readout error mitigation and Pauli twirling. 360 experiments with 10000 shots were taken and averaged, with error bars corresponding to standard error of the mean. The simulation depolarizing noise strength is $p = 0.049$, with 4 million shots.

The hierarchy of purities in the prediction (which is observed in the theory and simulation curves) is ambiguous in the experimental data. The ordering is not definitive even in the large- β limit where the LP differences should be maximal. In addition, the data fails the consistency check of the three LP curves agreeing in the $\beta = 0$ limit. Thus the result is inconclusive due to the quality of the data. A further interesting point about the results is that the loss in purity is much higher than expected - with a baseline LP of ~ 0.9 , the noisy simulation requires a two-qubit gate error probability 3-5x that of the rotation splitting experiment to reproduce the high levels of (device) decoherence. Furthermore, again unlike the rotation splitting experiment,

the noisy simulation curves do not agree well with the experimental data. This suggests that there are additional sources of error that may be relevant in the analysis of this experiment, such as the thermal relaxation errors. Since the circuit runtimes of this set of experiments are $\sim 4\times$ that of the previous as analyzed in Section 4.3.3, the thermal relaxation of the qubits may enter (in addition to the two-qubit gate errors) as dominant noise source. In addition, though we considered an idealized error model consisting solely of uniform 2-qubit gate errors across the device, to better predict the results of this more complex experiment we may need to include non-uniformity in the errors in the experimental device. This may be done by including gate, readout, and relaxation errors that vary across individual qubits.

In closing out the discussion of the experiment, we discuss another subtlety with our experiment - namely that our system does not fully respect the assumptions of the “counterintuitive is the most efficient” theorem which we are trying to demonstrate. In Fig. 5.11, we compare the theory loss in purities for *all* possible methods of splitting a rotation for an 11-qubit $|\Omega(\phi)\rangle$ chain as we vary ϕ . Namely, we compare two rotations with $\Delta = 2$, two rotations with $\Delta = 4/6$ (the loss in purity in the two cases are equivalent), three rotations with $\Delta = 2$, three rotations - one with $\Delta = 2$ and one with $\Delta = 4$, and four $\Delta = 2$ rotations, all which are calculated in Appendix B.3

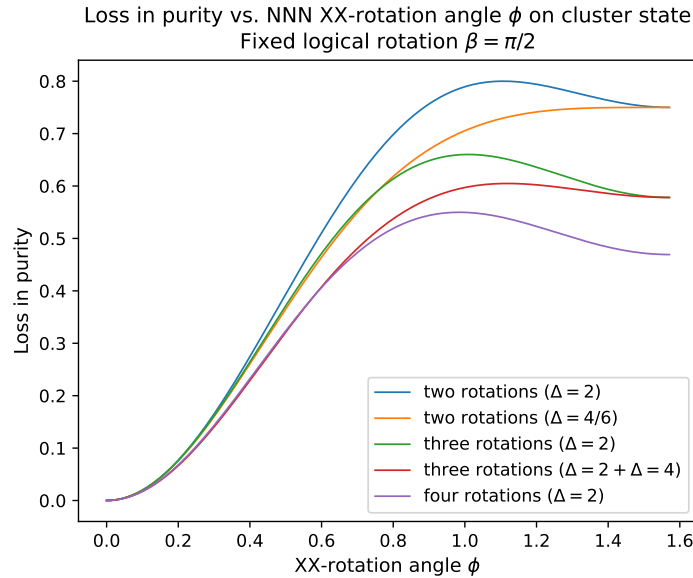


Figure 5.11: Comparison of loss in purities for 2/3/4 split rotations (with various spacings Δ) for $|\Omega(\phi)\rangle$ as a function of ϕ . We fix the logical rotation angle to be the maximally symmetry-breaking value of $\beta = \pi/2$ and use the analytical expressions of Eqs. (B.3.4) - (B.3.8) to obtain the plot.

Comparing the curves, we see that (as Prediction 4 outlines) maximally splitting the rotations (four rotations with $\Delta = 2$) outperforms two uncorrelated rotations (two rotations with $\Delta = 4/6$) which outperforms two correlated rotations (two rotations with $\Delta = 2$), and this hierarchy of efficiency holds for all possible ϕ . Analyzing the LP curves for 3 rotations, we observe some interesting behaviour. Namely, there exists a angle ϕ_1 below which two rotations with $\Delta = 4$ outperforms three rotations with $\Delta = 2$, and a angle ϕ_2 below which the three rotation protocol with

non-uniform spacing of $\Delta = 2$ and $\Delta = 4$ outperforms four rotations with $\Delta = 2$. Numerically these cross-over angles are found to be:

$$\phi_1 \approx 0.757 \tag{5.4.1a}$$

$$\phi_2 \approx 0.574 \tag{5.4.1b}$$

Theorem 2 of [AYR23] suggests that the densest ($\Delta = 2$) packing of symmetry-breaking measurements should be the most computationally efficient for any state in the $\mathbb{Z}_2 \times \mathbb{Z}_2$ cluster phase for which $\sigma(d)$ is convex. While our state $|\Omega(\phi)\rangle$ satisfies the convexity condition, it *cannot* be said to be in the cluster phase when realized on a chain of 11 qubits, and thus does not obey all the necessary conditions for the theorem to apply. The assumption of large system size is required to neglect the order $O(1/m^2)$ terms present in the error expression of Eq. (2.3.18), upon which Theorem 2 is based. For a small number of splittings m (equivalently - a small number of qubits n for which the rotation can be split across) the $O(1/m^2)$ terms become relevant, and thus it is possible to construct states (as we have here) for which the densest packing of symmetry-breaking measurements is not necessarily the most efficient. We note that since the XX -rotation angle $\phi = \pi/4$ we choose in our experiments is greater than both the critical values ϕ_1, ϕ_2 , for $|\Omega(\phi = \pi/4)\rangle$ it is indeed the case that the densest packing is the most efficient. However, a true experimental demonstration of the theorem using $|\Omega(\phi)\rangle$ (or any other resource state) that doesn't require restriction/tuning to particular ϕ s would require a larger system size where the assumptions of the theorem are satisfied.

Chapter 6

Conclusion

In this thesis, we have experimentally showcased state-of-the-art phenomenology of MBQC on IBM's superconducting hardware. We introduced a variational algorithm to prepare a family of states with tunable computational order. We first showed that the decoherence of the logical information scaled with the computational order of the state (Prediction 1). We then proceeded to show the equivalence of computational and string order via a comparison of the output of the MBQC protocol with the independent measurement of the string order parameter (Prediction 2). We then explored the rotation splitting technique, wherein the loss in purity of the encoded information can be reduced via a subdivision of the logical rotation into multiple symmetry-breaking measurements. We demonstrated that the loss in purity scales as $1/m$ in the number of divisions m , as is predicted by the theory (Prediction 3).

We then considered a resource state with a length scale to probe the effects of correlations in MBQC. The theory prediction is that the “counterintuitive regime” of computation is the most efficient, wherein maximally dense packing of symmetry-breaking measurements minimizes the logical decoherence, even at the expense of the operations not being independent (Prediction 4). We thus compared the loss in purity between MBQC protocols with two correlated rotations, two uncorrelated rotations, and four correlated rotations. The data here was inconclusive on whether the four correlated rotations was the most efficient protocol. We observed high logical error rates and a failure to satisfy basic consistency conditions, with the losses in purity disagreeing in the 0 rotation angle limit.

One immediate avenue for potential future work is a refinement of the fourth experiment. On the level of experimental data, the loss in purity we see in the encoded information for this experiment is quite severe, nearing the single-qubit mixed state due to device decoherence. An increased understanding of the source of this experimental error and subsequent techniques for mitigation would be valuable. In addition, we discussed how the theory motivation for this experiment is cloudy given that our 11-qubit chain does not satisfy the large-system size assumption required for “counterintuitive is the most efficient” to generically hold. Future work may thus compare MBQC protocols in larger chains, where the theory can be more concretely applied. We anticipate that further improvements to hardware error rates may be required for such large-chain experiments, given the already low signal-to-noise ratio for the 11-qubit chains considered in this work.

Other possible avenues remain in the further theory developments for MBQC in finite systems. Though in this work we considered only logical Z -rotations, in composing a general single-qubit $SU(2)$ rotation one intersperses Z with X rotations. Although the theory is currently able to handle Z and X rotations independently, the most efficient method to subdivide and compose logical operations using rotations of both types simultaneously remains an open problem. In

addition, while all results in this work centered on 1-D MBQC which only encodes a single qubit, this setting is not universal. A valuable generalization for the classification of universal MBQC resources would be an extension of the order parameter formalism to 2-D. Through this, we will obtain a more comprehensive algebraic classification of universal MBQC resource states. This will provide insight into the structures underlying computational speedups - and shed more light on the question of “What can quantum computers do (better than classical computers)?”

The work presented in this thesis primarily focused on the experimental interpretation of this question, of “What can quantum computers do (today)?” Although they are still faced with limitations in scale and fidelity, we have shown that the characterization of MBQC resource states and protocols can join the list of interesting phenomenology current hardware is capable of exploring. As devices further advance beyond the NISQ-era, so too will our capability to experimentally test further developments in the theory of MBQC. We hope that our work provides a starting point of this exploration as we ponder “What can quantum computers do (in the future)?”

Bibliography

- [AAB⁺19] Frank Arute, Kunal Arya, Ryan Babbush, Dave Bacon, Joseph C. Bardin, Rami Barends, Rupak Biswas, Sergio Boixo, Fernando G. S. L. Brandao, David A. Buell, Brian Burkett, Yu Chen, Zijun Chen, Ben Chiaro, Roberto Collins, William Courtney, Andrew Dunsworth, Edward Farhi, Brooks Foxen, Austin Fowler, Craig Gidney, Marissa Giustina, Rob Graff, Keith Guerin, Steve Habegger, Matthew P. Harrigan, Michael J. Hartmann, Alan Ho, Markus Hoffmann, Trent Huang, Travis S. Humble, Sergei V. Isakov, Evan Jeffrey, Zhang Jiang, Dvir Kafri, Kostyantyn Kechedzhi, Julian Kelly, Paul V. Klimov, Sergey Knysh, Alexander Korotkov, Fedor Kostritsa, David Landhuis, Mike Lindmark, Erik Lucero, Dmitry Lyakh, Salvatore Mandrà, Jarrod R. McClean, Matthew McEwen, Anthony Megrant, Xiao Mi, Kristel Michielsen, Masoud Mohseni, Josh Mutus, Ofer Naaman, Matthew Neeley, Charles Neill, Murphy Yuezhen Niu, Eric Ostby, Andre Petukhov, John C. Platt, Chris Quintana, Eleanor G. Rieffel, Pedram Roushan, Nicholas C. Rubin, Daniel Sank, Kevin J. Satzinger, Vadim Smelyanskiy, Kevin J. Sung, Matthew D. Trevithick, Amit Vainsencher, Benjamin Villalonga, Theodore White, Z. Jamie Yao, Ping Yeh, Adam Zalcman, Hartmut Neven, and John M. Martinis. Quantum supremacy using a programmable superconducting processor. *Nature*, 574(7779):505–510, October 2019. 1
- [AF24] Victor V. Albert and Philippe Faist, editors. *The Error Correction Zoo*. 2024. 1
- [AHN⁺20] Daniel Azses, Rafael Haenel, Yehuda Naveh, Robert Raussendorf, Eran Sela, and Emanuele G. Dalla Torre. Identification of Symmetry-Protected Topological States on Noisy Quantum Computers. *Physical Review Letters*, 125(12):120502, September 2020. 2
- [AKN98] Dorit Aharonov, Alexei Kitaev, and Noam Nisan. Quantum circuits with mixed states. (arXiv:quant-ph/9806029), June 1998. arXiv:quant-ph/9806029. 15
- [Amb17] Andris Ambainis. Understanding Quantum Algorithms via Query Complexity, December 2017. arXiv:1712.06349 [quant-ph]. 1
- [AYR23] Arnab Adhikary, Wang Yang, and Robert Raussendorf. Counter-intuitive yet efficient regimes for measurement based quantum computation on symmetry protected spin chains, July 2023. arXiv:2307.08903 [quant-ph]. 2, 16, 17, 23, 53
- [BAV⁺21] J. Eli Bourassa, Rafael N. Alexander, Michael Vasmer, Ashlesha Patil, Ilan Tzitrin, Takaya Matsuura, Daiqin Su, Ben Q. Baragiola, Saikat Guha, Guillaume Dauphinais, Krishna K. Sabapathy, Nicolas C. Menicucci, and Ish Dhand. Blueprint for a

- Scalable Photonic Fault-Tolerant Quantum Computer. *Quantum*, 5:392, February 2021. arXiv:2010.02905 [quant-ph]. 6
- [BBC⁺93] Charles H. Bennett, Gilles Brassard, Claude Crépeau, Richard Jozsa, Asher Peres, and William K. Wootters. Teleporting an unknown quantum state via dual classical and Einstein-Podolsky-Rosen channels. *Physical Review Letters*, 70(13):1895–1899, March 1993. 8
- [BBK⁺23] Ryan Babbush, Dominic W. Berry, Robin Kothari, Rolando D. Somma, and Nathan Wiebe. Exponential Quantum Speedup in Simulating Coupled Classical Oscillators. *Physical Review X*, 13(4):041041, December 2023. 1
- [BCG⁺24] Sergey Bravyi, Andrew W. Cross, Jay M. Gambetta, Dmitri Maslov, Patrick Rall, and Theodore J. Yoder. High-threshold and low-overhead fault-tolerant quantum memory. *Nature*, 627(8005):778–782, March 2024. 1
- [BEG⁺24] Dolev Bluvstein, Simon J. Evered, Alexandra A. Geim, Sophie H. Li, Hengyun Zhou, Tom Manovitz, Sepehr Ebadi, Madelyn Cain, Marcin Kalinowski, Dominik Hangleiter, J. Pablo Bonilla Ataides, Nishad Maskara, Iris Cong, Xun Gao, Pedro Sales Rodriguez, Thomas Karolyshyn, Giulia Semeghini, Michael J. Gullans, Markus Greiner, Vladan Vuletić, and Mikhail D. Lukin. Logical quantum processor based on reconfigurable atom arrays. *Nature*, 626(7997):58–65, February 2024. 1
- [CGW10] Xie Chen, Zheng-Cheng Gu, and Xiao-Gang Wen. Local unitary transformation, long-range quantum entanglement, wave function renormalization, and topological order. *Physical Review B*, 82(15):155138, October 2010. 2
- [DAM20] Austin K. Daniel, Rafael N. Alexander, and Akimasa Miyake. Computational universality of symmetry-protected topologically ordered cluster phases on 2D Archimedean lattices. *Quantum*, 4:228, February 2020. arXiv:1907.13279 [cond-mat, physics:quant-ph]. 2
- [DB09] Andrew C. Doherty and Stephen D. Bartlett. Identifying Phases of Quantum Many-Body Systems That Are Universal for Quantum Computation. *Physical Review Letters*, 103(2):020506, July 2009. 2
- [DBB12] Andrew S Darmawan, Gavin K Brennen, and Stephen D Bartlett. Measurement-based quantum computation in a two-dimensional phase of matter. *New Journal of Physics*, 14(1):013023, January 2012. 2
- [DGL⁺23] Yu-Hao Deng, Yi-Chao Gu, Hua-Liang Liu, Si-Qiu Gong, Hao Su, Zhi-Jiong Zhang, Hao-Yang Tang, Meng-Hao Jia, Jia-Min Xu, Ming-Cheng Chen, Jian Qin, Li-Chao Peng, Jiarong Yan, Yi Hu, Jia Huang, Hao Li, Yuxuan Li, Yaojian Chen, Xiao Jiang, Lin Gan, Guangwen Yang, Lixing You, Li Li, Han-Sen Zhong, Hui Wang, Nai-Le Liu, Jelmer J. Renema, Chao-Yang Lu, and Jian-Wei Pan. Gaussian Boson Sampling with Pseudo-Photon-Number Resolving Detectors and Quantum Computational Advantage, September 2023. arXiv:2304.12240 [quant-ph]. 1

- [DHL⁺24] Matthew DeCross, Reza Haghshenas, Minzhao Liu, Yuri Alexeev, Charles H. Baldwin, John P. Bartolotta, Matthew Bohn, Eli Chertkov, Jonhas Colina, Davide DelVento, Joan M. Dreiling, Cameron Foltz, John P. Gaebler, Thomas M. Gatterman, Christopher N. Gilbreth, Johnnie Gray, Dan Gresh, Nathan Hewitt, Ross B. Hutson, Jacob Johansen, Dominic Lucchetti, Danylo Lykov, Ivaylo S. Madjarov, Karl Mayer, Michael Mills, Pradeep Niroula, Enrico Rinaldi, Peter E. Siegfried, Bruce G. Tiemann, James Walker, Ruslan Shaydulin, Marco Pistoia, Steven A. Moses, David Hayes, Brian Neyenhuis, Russell P. Stutz, and Michael Foss-Feig. The computational power of random quantum circuits in arbitrary geometries, June 2024. arXiv:2406.02501 [quant-ph]. 1
- [DMB⁺23] Alexander M. Dalzell, Sam McArdle, Mario Berta, Przemyslaw Bienias, Chi-Fang Chen, András Gilyén, Connor T. Hann, Michael J. Kastoryano, Emil T. Khabiboulline, Aleksander Kubica, Grant Salton, Samson Wang, and Fernando G. S. L. Brandão. Quantum algorithms: A survey of applications and end-to-end complexities, October 2023. arXiv:2310.03011 [quant-ph]. 1
- [dSRABR⁺24] M. P. da Silva, C. Ryan-Anderson, J. M. Bello-Rivas, A. Chernoguzov, J. M. Dreiling, C. Foltz, F. Frachon, J. P. Gaebler, T. M. Gatterman, L. Grans-Samuelsson, D. Hayes, N. Hewitt, J. Johansen, D. Lucchetti, M. Mills, S. A. Moses, B. Neyenhuis, A. Paz, J. Pino, P. Siegfried, J. Strabley, A. Sundaram, D. Tom, S. J. Wernli, M. Zanner, R. P. Stutz, and K. M. Svore. Demonstration of logical qubits and repeated error correction with better-than-physical error rates, April 2024. arXiv:2404.02280 [quant-ph]. 1
- [DW18] Trithep Devakul and Dominic J. Williamson. Universal quantum computation using fractal symmetry-protected cluster phases. *Physical Review A*, 98(2):022332, August 2018. 2
- [EBD12] Dominic V. Else, Stephen D. Bartlett, and Andrew C. Doherty. Symmetry protection of measurement-based quantum computation in ground states. *New Journal of Physics*, 14(11):113016, November 2012. arXiv:1207.4805 [cond-mat, physics:quant-ph]. 2
- [ESBD12] Dominic V. Else, Ilai Schwarz, Stephen D. Bartlett, and Andrew C. Doherty. Symmetry-protected phases for measurement-based quantum computation. *Physical Review Letters*, 108(24):240505, June 2012. arXiv:1201.4877 [cond-mat, physics:quant-ph]. 2
- [GAA⁺23] Google Quantum AI, Rajeev Acharya, Igor Aleiner, Richard Allen, Trond I. Andersen, Markus Ansmann, Frank Arute, Kunal Arya, Abraham Asfaw, Juan Atalaya, Ryan Babbush, Dave Bacon, Joseph C. Bardin, Joao Basso, Andreas Bengtsson, Sergio Boixo, Gina Bortoli, Alexandre Bourassa, Jenna Bovaird, Leon Brill, Michael Broughton, Bob B. Buckley, David A. Buell, Tim Burger, Brian Burkett, Nicholas Bushnell, Yu Chen, Zijun Chen, Ben Chiaro, Josh Cogan, Roberto Collins, Paul Conner, William Courtney, Alexander L. Crook, Ben Curtin, Dripto M. Debroy, Alexander Del Toro Barba, Sean Demura, Andrew Dunsworth, Daniel Eppens, Catherine Erickson, Lara Faoro, Edward Farhi, Reza Fatemi, Leslie Flo-

res Burgos, Ebrahim Forati, Austin G. Fowler, Brooks Foxen, William Giang, Craig Gidney, Dar Gilboa, Marissa Giustina, Alejandro Grajales Dau, Jonathan A. Gross, Steve Habegger, Michael C. Hamilton, Matthew P. Harrigan, Sean D. Harrington, Oscar Higgott, Jeremy Hilton, Markus Hoffmann, Sabrina Hong, Trent Huang, Ashley Huff, William J. Huggins, Lev B. Ioffe, Sergei V. Isakov, Justin Iveland, Evan Jeffrey, Zhang Jiang, Cody Jones, Pavol Juhas, Dvir Kafri, Kostyantyn Kechedzhi, Julian Kelly, Tanuj Khattar, Mostafa Khezri, Mária Kieferová, Seon Kim, Alexei Kitaev, Paul V. Klimov, Andrey R. Klots, Alexander N. Korotkov, Fedor Kostritsa, John Mark Kreikebaum, David Landhuis, Pavel Laptev, Kim-Ming Lau, Lily Laws, Joonho Lee, Kenny Lee, Brian J. Lester, Alexander Lill, Wayne Liu, Aditya Locharla, Erik Lucero, Fionn D. Malone, Jeffrey Marshall, Orion Martin, Jarrod R. McClean, Trevor McCourt, Matt McEwen, Anthony Megrant, Bernardo Meurer Costa, Xiao Mi, Kevin C. Miao, Masoud Mohseni, Shirin Montazeri, Alexis Morvan, Emily Mount, Wojciech Mruczkiewicz, Ofer Naaman, Matthew Neeley, Charles Neill, Ani Nersisyan, Hartmut Neven, Michael Newman, Jiun How Ng, Anthony Nguyen, Murray Nguyen, Murphy Yuezhen Niu, Thomas E. O'Brien, Alex Opremcak, John Platt, Andre Petukhov, Rebecca Potter, Leonid P. Pryadko, Chris Quintana, Pedram Roushan, Nicholas C. Rubin, Negar Saei, Daniel Sank, Kannan Sankaragomathi, Kevin J. Satzinger, Henry F. Schurkus, Christopher Schuster, Michael J. Shearn, Aaron Shorter, Vladimir Shvarts, Jindra Skrzyny, Vadim Smelyanskiy, W. Clarke Smith, George Sterling, Doug Strain, Marco Szalay, Alfredo Torres, Guifre Vidal, Benjamin Villalonga, Catherine Vollgraff Heideweiler, Theodore White, Cheng Xing, Z. Jamie Yao, Ping Yeh, Juhwan Yoo, Grayson Young, Adam Zalcman, Yaxing Zhang, and Ningfeng Zhu. Suppressing quantum errors by scaling a surface code logical qubit. *Nature*, 614(7949):676–681, February 2023. 1

- [GFE09] D. Gross, S. Flammia, and J. Eisert. Most quantum states are too entangled to be useful as computational resources. *Physical Review Letters*, 102(19):190501, May 2009. arXiv:0810.4331 [quant-ph]. 2
- [GJW⁺23] L C G Gavia, P Jurcevic, C J Wood, N Kanazawa, S T Merkel, and D C McKay. A randomized benchmarking suite for mid-circuit measurements. *New Journal of Physics*, 25(12):123016, December 2023. 36
- [Got98] Daniel Gottesman. The Heisenberg Representation of Quantum Computers, July 1998. arXiv:quant-ph/9807006. 1
- [Gro96] Lov K. Grover. A fast quantum mechanical algorithm for database search. In *Proceedings of the twenty-eighth annual ACM symposium on Theory of computing - STOC '96*, pages 212–219, Philadelphia, Pennsylvania, United States, 1996. ACM Press. 1
- [HWVE14] Mark Howard, Joel Wallman, Victor Veitch, and Joseph Emerson. Contextuality supplies the ‘magic’ for quantum computation. *Nature*, 510(7505):351–355, June 2014. 1

- [HZN⁺20] Cupjin Huang, Fang Zhang, Michael Newman, Junjie Cai, Xun Gao, Zhengxiong Tian, Junyin Wu, Haihong Xu, Huanjun Yu, Bo Yuan, Mario Szegedy, Yaoyun Shi, and Jianxin Chen. Classical Simulation of Quantum Supremacy Circuits, May 2020. arXiv:2005.06787 [quant-ph]. 1
- [ITV⁺24] Mohsin Iqbal, Nathanan Tantivasadakarn, Ruben Verresen, Sara L. Campbell, Joan M. Dreiling, Caroline Figgatt, John P. Gaebler, Jacob Johansen, Michael Mills, Steven A. Moses, Juan M. Pino, Anthony Ransford, Mary Rowe, Peter Siegfried, Russell P. Stutz, Michael Foss-Feig, Ashvin Vishwanath, and Henrik Dreyer. Non-Abelian topological order and anyons on a trapped-ion processor. *Nature*, 626(7999):505–511, February 2024. 1
- [JATK⁺24] Ali Javadi-Abhari, Matthew Treinish, Kevin Krsulich, Christopher J. Wood, Jake Lishman, Julien Gacon, Simon Martiel, Paul D. Nation, Lev S. Bishop, Andrew W. Cross, Blake R. Johnson, and Jay M. Gambetta. Quantum computing with Qiskit, May 2024. arXiv:2405.08810 [quant-ph]. 33
- [KEA⁺23] Youngseok Kim, Andrew Eddins, Sajant Anand, Ken Xuan Wei, Ewout Van Den Berg, Sami Rosenblatt, Hasan Nayfeh, Yantao Wu, Michael Zaletel, Kristan Temme, and Abhinav Kandala. Evidence for the utility of quantum computing before fault tolerance. *Nature*, 618(7965):500–505, June 2023. 1
- [KKT24] Jin Ming Koh, Dax Enshan Koh, and Jayne Thompson. Readout Error Mitigation for Mid-Circuit Measurements and Feedforward, June 2024. arXiv:2406.07611 [quant-ph]. 36
- [KNR⁺24] Andrew D. King, Alberto Nocera, Marek M. Rams, Jacek Dziarmaga, Roeland Wiersema, William Bernoudy, Jack Raymond, Nitin Kaushal, Niclas Heinsdorf, Richard Harris, Kelly Boothby, Fabio Altomare, Andrew J. Berkley, Martin Boschnak, Kevin Chern, Holly Christiani, Samantha Cibere, Jake Connor, Martin H. Dehn, Rahul Deshpande, Sara Ejtemaee, Pau Farré, Kelsey Hamer, Emile Hoskinson, Shuiyuan Huang, Mark W. Johnson, Samuel Kortas, Eric Ladizinsky, Tony Lai, Trevor Lanting, Ryan Li, Allison J. R. MacDonald, Gaelen Marsden, Catherine C. McGeoch, Reza Molavi, Richard Neufeld, Mana Norouzpour, Travis Oh, Joel Pasvolsky, Patrick Poitras, Gabriel Poulin-Lamarre, Thomas Prescott, Mauricio Reis, Chris Rich, Mohammad Samani, Benjamin Sheldon, Anatoly Smirnov, Edward Sterpka, Berta Trullas Clavera, Nicholas Tsai, Mark Volkmann, Alexander Whitar, Jed D. Whittaker, Warren Wilkinson, Jason Yao, T. J. Yi, Anders W. Sandvik, Gonzalo Alvarez, Roger G. Melko, Juan Carrasquilla, Marcel Franz, and Mohammad H. Amin. Computational supremacy in quantum simulation, March 2024. arXiv:2403.00910 [cond-mat, physics:quant-ph]. 1
- [Llo96] Seth Lloyd. Universal Quantum Simulators. *Science*, 273(5278):1073–1078, August 1996. 1
- [MBKE11] Easwar Magesan, Robin Blume-Kohout, and Joseph Emerson. Gate fidelity fluctuations and quantum process invariants. *Physical Review A*, 84(1):012309, July 2011. arXiv:0910.1315 [math-ph, physics:quant-ph]. 38

- [MEAG⁺20] Sam McArdle, Suguru Endo, Alán Aspuru-Guzik, Simon C. Benjamin, and Xiao Yuan. Quantum computational chemistry. *Reviews of Modern Physics*, 92(1):015003, March 2020. 1
- [Miy10] Akimasa Miyake. Quantum Computation on the Edge of a Symmetry-Protected Topological Order. *Physical Review Letters*, 105(4):040501, July 2010. 2
- [Miy11] Akimasa Miyake. Quantum computational capability of a 2D valence bond solid phase. *Annals of Physics*, 326(7):1656–1671, July 2011. 2
- [MLA⁺22] Lars S. Madsen, Fabian Laudenbach, Mohsen Falamarzi. Askarani, Fabien Rortais, Trevor Vincent, Jacob F. F. Bulmer, Filippo M. Miatto, Leonhard Neuhaus, Lukas G. Helt, Matthew J. Collins, Adriana E. Lita, Thomas Gerrits, Sae Woo Nam, Varun D. Vaidya, Matteo Menotti, Ish Dhand, Zachary Vernon, Nicolás Quesada, and Jonathan Lavoie. Quantum computational advantage with a programmable photonic processor. *Nature*, 606(7912):75–81, June 2022. 1
- [MVM⁺23] A. Morvan, B. Villalonga, X. Mi, S. Mandrà, A. Bengtsson, P. V. Klimov, Z. Chen, S. Hong, C. Erickson, I. K. Drozdov, J. Chau, G. Laun, R. Movassagh, A. Asfaw, L. T. A. N. Brandão, R. Peralta, D. Abanin, R. Acharya, R. Allen, T. I. Andersen, K. Anderson, M. Ansmann, F. Arute, K. Arya, J. Atalaya, J. C. Bardin, A. Bilmes, G. Bortoli, A. Bourassa, J. Bovaird, L. Brill, M. Broughton, B. B. Buckley, D. A. Buell, T. Burger, B. Burkett, N. Bushnell, J. Campero, H. S. Chang, B. Chiaro, D. Chik, C. Chou, J. Cogan, R. Collins, P. Conner, W. Courtney, A. L. Crook, B. Curtin, D. M. Debroy, A. Del Toro Barba, S. Demura, A. Di Paolo, A. Dunsworth, L. Faoro, E. Farhi, R. Fatemi, V. S. Ferreira, L. Flores Burgos, E. Forati, A. G. Fowler, B. Foxen, G. Garcia, E. Genois, W. Jiang, C. Gidney, D. Gilboa, M. Giustina, R. Gosula, A. Grajales Dau, J. A. Gross, S. Habegger, M. C. Hamilton, M. Hansen, M. P. Harrigan, S. D. Harrington, P. Heu, M. R. Hoffmann, T. Huang, A. Huff, W. J. Huggins, L. B. Ioffe, S. V. Isakov, J. Iveland, E. Jeffrey, Z. Jiang, C. Jones, P. Juhas, D. Kafri, T. Khattar, M. Khezri, M. Kieferová, S. Kim, A. Kitaev, A. R. Klots, A. N. Korotkov, F. Kostritsa, J. M. Kreikebaum, D. Landhuis, P. Laptev, K.-M. Lau, L. Laws, J. Lee, K. W. Lee, Y. D. Lensky, B. J. Lester, A. T. Lill, W. Liu, W. P. Livingston, A. Locharla, F. D. Malone, O. Martin, S. Martin, J. R. McClean, M. McEwen, K. C. Miao, A. Mieszala, S. Montazeri, W. Mruczkiewicz, O. Naaman, M. Neeley, C. Neill, A. Nersisyan, M. Newman, J. H. Ng, A. Nguyen, M. Nguyen, M. Yuezhen Niu, T. E. O’Brien, S. Omonije, A. Opremcak, A. Petukhov, R. Potter, L. P. Pryadko, C. Quintana, D. M. Rhodes, E. Rosenberg, C. Rocque, P. Roushan, N. C. Rubin, N. Saei, D. Sank, K. Sankaragomathi, K. J. Satzinger, H. F. Schurkus, C. Schuster, M. J. Shearn, A. Shorter, N. Shutty, V. Shvarts, V. Sivak, J. Skrzynny, W. C. Smith, R. D. Somma, G. Sterling, D. Strain, M. Szalay, D. Thor, A. Torres, G. Vidal, C. Vollgraff Heidweiller, T. White, B. W. K. Woo, C. Xing, Z. J. Yao, P. Yeh, J. Yoo, G. Young, A. Zalcman, Y. Zhang, N. Zhu, N. Zobrist, E. G. Rieffel, R. Biswas, R. Babbush, D. Bacon, J. Hilton, E. Lucero, H. Neven, A. Megrant, J. Kelly, I. Aleiner, V. Smelyanskiy, K. Kechedzhi, Y. Chen, and S. Boixo. Phase transition in Random Circuit Sampling, December 2023. arXiv:2304.11119 [quant-ph]. 1

- [NC10] Michael A. Nielsen and Isaac L. Chuang. *Quantum computation and quantum information*. Cambridge University Press, Cambridge ; New York, 10th anniversary edition, 2010. 5, 40
- [NKSG21] Paul D. Nation, Hwajung Kang, Neereja Sundaresan, and Jay M. Gambetta. Scalable Mitigation of Measurement Errors on Quantum Computers. *PRX Quantum*, 2(4):040326, November 2021. 37
- [OLA⁺24] Changhun Oh, Minzhao Liu, Yuri Alexeev, Bill Fefferman, and Liang Jiang. Classical algorithm for simulating experimental Gaussian boson sampling. *Nature Physics*, June 2024. 1
- [PBP⁺23] Lukas Postler, Friederike Butt, Ivan Pogorelov, Christian D. Marciniak, Sascha Heußen, Rainer Blatt, Philipp Schindler, Manuel Risppler, Markus Müller, and Thomas Monz. Demonstration of fault-tolerant Steane quantum error correction, December 2023. arXiv:2312.09745 [quant-ph]. 1
- [Pre18] John Preskill. Quantum Computing in the NISQ era and beyond. *Quantum*, 2:79, August 2018. arXiv:1801.00862 [cond-mat, physics:quant-ph]. 1
- [QFK⁺22] Yihui Quek, Daniel Stilck França, Sumeet Khatri, Johannes Jakob Meyer, and Jens Eisert. Exponentially tighter bounds on limitations of quantum error mitigation, October 2022. arXiv:2210.11505 [math-ph, physics:quant-ph]. 37
- [RB01] Robert Raussendorf and Hans J. Briegel. A One-Way Quantum Computer. *Physical Review Letters*, 86(22):5188–5191, May 2001. 2, 6
- [RB20] Sam Roberts and Stephen D. Bartlett. Symmetry-Protected Self-Correcting Quantum Memories. *Physical Review X*, 10(3):031041, August 2020. 2
- [RBB03] R. Raussendorf, D. E. Browne, and H. J. Briegel. Measurement-based quantum computation with cluster states. *Physical Review A*, 68(2):022312, August 2003. arXiv:quant-ph/0301052. 1, 6
- [RHG06] R. Raussendorf, J. Harrington, and K. Goyal. A fault-tolerant one-way quantum computer. *Annals of Physics*, 321(9):2242–2270, September 2006. arXiv:quant-ph/0510135. 11
- [RHG07] R Raussendorf, J Harrington, and K Goyal. Topological fault-tolerance in cluster state quantum computation. *New Journal of Physics*, 9(6):199–199, June 2007. 11
- [ROW⁺19] Robert Raussendorf, Cihan Okay, Dong-Sheng Wang, David T. Stephen, and Hendrik Poulsen Nautrup. A computationally universal phase of quantum matter. *Physical Review Letters*, 122(9):090501, March 2019. arXiv:1803.00095 [quant-ph]. 2
- [RWP⁺17] Robert Raussendorf, Dongsheng Wang, Abhishodh Prakash, Tzu-Chieh Wei, and David Stephen. Symmetry-protected topological phases with uniform computational power in one dimension. *Physical Review A*, 96(1):012302, July 2017. arXiv:1609.07549 [quant-ph]. 2

- [RYA23] Robert Raussendorf, Wang Yang, and Arnab Adhikary. Measurement-based quantum computation in finite one-dimensional systems: string order implies computational power. *Quantum*, 7:1215, December 2023. arXiv:2210.05089 [quant-ph]. 2, 11, 15, 16
- [Sho95] Peter W. Shor. Scheme for reducing decoherence in quantum computer memory. *Physical Review A*, 52(4):R2493–R2496, October 1995. 1
- [Sho97] Peter W. Shor. Polynomial-Time Algorithms for Prime Factorization and Discrete Logarithms on a Quantum Computer. *SIAM Journal on Computing*, 26(5):1484–1509, October 1997. arXiv:quant-ph/9508027. 1
- [SHW⁺22] David T. Stephen, Wen Wei Ho, Tzu-Chieh Wei, Robert Raussendorf, and Ruben Verresen. Universal measurement-based quantum computation in a one-dimensional architecture enabled by dual-unitary circuits, September 2022. arXiv:2209.06191 [cond-mat, physics:quant-ph]. 11
- [SLS⁺21] K. J. Satzinger, Y.-J. Liu, A. Smith, C. Knapp, M. Newman, C. Jones, Z. Chen, C. Quintana, X. Mi, A. Dunsworth, C. Gidney, I. Aleiner, F. Arute, K. Arya, J. Atalaya, R. Babbush, J. C. Bardin, R. Barends, J. Basso, A. Bengtsson, A. Bilmes, M. Broughton, B. B. Buckley, D. A. Buell, B. Burkett, N. Bushnell, B. Chiaro, R. Collins, W. Courtney, S. Demura, A. R. Derk, D. Eppens, C. Erickson, L. Faoro, E. Farhi, A. G. Fowler, B. Foxen, M. Giustina, A. Greene, J. A. Gross, M. P. Harrigan, S. D. Harrington, J. Hilton, S. Hong, T. Huang, W. J. Huggins, L. B. Ioffe, S. V. Isakov, E. Jeffrey, Z. Jiang, D. Kafri, K. Kechedzhi, T. Khattar, S. Kim, P. V. Klimov, A. N. Korotkov, F. Kostritsa, D. Landhuis, P. Laptev, A. Locharla, E. Lucero, O. Martin, J. R. McClean, M. McEwen, K. C. Miao, M. Mohseni, S. Montazeri, W. Mruczkiewicz, J. Mutus, O. Naaman, M. Neeley, C. Neill, M. Y. Niu, T. E. O’Brien, A. Opremcak, B. Pató, A. Petukhov, N. C. Rubin, D. Sank, V. Shvarts, D. Strain, M. Szalay, B. Villalonga, T. C. White, Z. Yao, P. Yeh, J. Yoo, A. Zalcman, H. Neven, S. Boixo, A. Megrant, Y. Chen, J. Kelly, V. Smelyanskiy, A. Kitaev, M. Knap, F. Pollmann, and P. Roushan. Realizing topologically ordered states on a quantum processor. *Science*, 374(6572):1237–1241, December 2021. 1
- [SN20] J. J. Sakurai and Jim Napolitano. *Modern Quantum Mechanics*. Cambridge University Press, 3 edition, September 2020. 26, 67
- [SNBV⁺19] David T. Stephen, Hendrik Poulsen Nautrup, Juani Bermejo-Vega, Jens Eisert, and Robert Raussendorf. Subsystem symmetries, quantum cellular automata, and computational phases of quantum matter. *Quantum*, 3:142, May 2019. arXiv:1806.08780 [cond-mat, physics:quant-ph]. 2
- [SWP⁺17] David T. Stephen, Dong-Sheng Wang, Abhishodh Prakash, Tzu-Chieh Wei, and Robert Raussendorf. Computational Power of Symmetry-Protected Topological Phases. *Physical Review Letters*, 119(1):010504, July 2017. arXiv:1611.08053 [quant-ph]. 2

- [SYGY24] Thomas Schuster, Chao Yin, Xun Gao, and Norman Y. Yao. A polynomial-time classical algorithm for noisy quantum circuits. (arXiv:2407.12768), July 2024. arXiv:2407.12768 [math-ph, physics:physics, physics:quant-ph]. 1, 37
- [TCC⁺22] Jules Tilly, Hongxiang Chen, Shuxiang Cao, Dario Picozzi, Kanav Setia, Ying Li, Edward Grant, Leonard Wossnig, Ivan Rungger, George H. Booth, and Jonathan Tennyson. The Variational Quantum Eigensolver: a review of methods and best practices. *Physics Reports*, 986:1–128, November 2022. arXiv:2111.05176 [quant-ph]. 26
- [TFSS24] Joseph Tindall, Matt Fishman, Miles Stoudenmire, and Dries Sels. Efficient tensor network simulation of IBM’s Eagle kicked Ising experiment. *PRX Quantum*, 5(1):010308, January 2024. arXiv:2306.14887 [quant-ph]. 1
- [VFGE12] Victor Veitch, Christopher Ferrie, David Gross, and Joseph Emerson. Negative quasi-probability as a resource for quantum computation. *New Journal of Physics*, 14(11):113011, November 2012. 1
- [WBC⁺21] Yulin Wu, Wan-Su Bao, Sirui Cao, Fusheng Chen, Ming-Cheng Chen, Xiawei Chen, Tung-Hsun Chung, Hui Deng, Yajie Du, Daojin Fan, Ming Gong, Cheng Guo, Chu Guo, Shaojun Guo, Lianchen Han, Linyin Hong, He-Liang Huang, Yong-Heng Huo, Liping Li, Na Li, Shaowei Li, Yuan Li, Futian Liang, Chun Lin, Jin Lin, Haoran Qian, Dan Qiao, Hao Rong, Hong Su, Lihua Sun, Liangyuan Wang, Shiyu Wang, Dachao Wu, Yu Xu, Kai Yan, Weifeng Yang, Yang Yang, Yangsen Ye, Jianghan Yin, Chong Ying, Jiale Yu, Chen Zha, Cha Zhang, Haibin Zhang, Kaili Zhang, Yiming Zhang, Han Zhao, Youwei Zhao, Liang Zhou, Qingling Zhu, Chao-Yang Lu, Cheng-Zhi Peng, Xiaobo Zhu, and Jian-Wei Pan. Strong Quantum Computational Advantage Using a Superconducting Quantum Processor. *Physical Review Letters*, 127(18):180501, October 2021. 1
- [WE16] Joel J. Wallman and Joseph Emerson. Noise tailoring for scalable quantum computation via randomized compiling. *Physical Review A*, 94(5):052325, November 2016. 38, 39
- [Wei22] Ryohei Weil. A Simulation of a Simulation: Algorithms for Symmetry-Protected Measurement-Based Quantum Computing Experiments. page 84, July 2022. 2, 5, 9
- [Wei24] Ryohei Weil. Ibmq-sptmbqc-v2. <https://github.com/RioWeil/IBMQ-SPTMBQC-v2>, 2024. 42
- [WLX⁺24] Ke Wang, Weikang Li, Shibo Xu, Mengyao Hu, Jiachen Chen, Yaozu Wu, Chuanyu Zhang, Feitong Jin, Xuhao Zhu, Yu Gao, Ziqi Tan, Aosai Zhang, Ning Wang, Yiren Zou, Tingting Li, Fanhao Shen, Jiarun Zhong, Zehang Bao, Zitian Zhu, Zixuan Song, Jinfeng Deng, Hang Dong, Xu Zhang, Pengfei Zhang, Wenjie Jiang, Zhide Lu, Zheng-Zhi Sun, Hekang Li, Qiujiang Guo, Zhen Wang, Patrick Emonts, Jordi Tura, Chao Song, H. Wang, and Dong-Ling Deng. Probing many-body Bell correlation depth with superconducting qubits, June 2024. arXiv:2406.17841 [quant-ph]. 1

- [WRR⁺05] P. Walther, K. J. Resch, T. Rudolph, E. Schenck, H. Weinfurter, V. Vedral, M. Aspelmeyer, and A. Zeilinger. Experimental one-way quantum computing. *Nature*, 434(7030):169–176, March 2005. 6
- [ZDQ⁺21] Han-Sen Zhong, Yu-Hao Deng, Jian Qin, Hui Wang, Ming-Cheng Chen, Li-Chao Peng, Yi-Han Luo, Dian Wu, Si-Qiu Gong, Hao Su, Yi Hu, Peng Hu, Xiao-Yan Yang, Wei-Jun Zhang, Hao Li, Yuxuan Li, Xiao Jiang, Lin Gan, Guangwen Yang, Lixing You, Zhen Wang, Li Li, Nai-Le Liu, Jelmer J. Renema, Chao-Yang Lu, and Jian-Wei Pan. Phase-Programmable Gaussian Boson Sampling Using Stimulated Squeezed Light. *Physical Review Letters*, 127(18):180502, October 2021. 1
- [ZWD⁺20] Han-Sen Zhong, Hui Wang, Yu-Hao Deng, Ming-Cheng Chen, Li-Chao Peng, Yi-Han Luo, Jian Qin, Dian Wu, Xing Ding, Yi Hu, Peng Hu, Xiao-Yan Yang, Wei-Jun Zhang, Hao Li, Yuxuan Li, Xiao Jiang, Lin Gan, Guangwen Yang, Lixing You, Zhen Wang, Li Li, Nai-Le Liu, Chao-Yang Lu, and Jian-Wei Pan. Quantum computational advantage using photons. *Science*, 370(6523):1460–1463, December 2020. 1
- [ZYH⁺22] Youwei Zhao, Yangsen Ye, He-Liang Huang, Yiming Zhang, Dachao Wu, Huijie Guan, Qingling Zhu, Zuolin Wei, Tan He, Sirui Cao, Fusheng Chen, Tung-Hsun Chung, Hui Deng, Daojin Fan, Ming Gong, Cheng Guo, Shaojun Guo, Lianchen Han, Na Li, Shaowei Li, Yuan Li, Futian Liang, Jin Lin, Haoran Qian, Hao Rong, Hong Su, Lihua Sun, Shiyu Wang, Yulin Wu, Yu Xu, Chong Ying, Jiale Yu, Chen Zha, Kaili Zhang, Yong-Heng Huo, Chao-Yang Lu, Cheng-Zhi Peng, Xiaobo Zhu, and Jian-Wei Pan. Realization of an Error-Correcting Surface Code with Superconducting Qubits. *Physical Review Letters*, 129(3):030501, July 2022. 1
- [ZZP⁺24] Xian-He Zhao, Han-Sen Zhong, Feng Pan, Zi-Han Chen, Rong Fu, Zhongling Su, Xiaotong Xie, Chaoxing Zhao, Pan Zhang, Wanli Ouyang, Chao-Yang Lu, Jian-Wei Pan, and Ming-Cheng Chen. Leapfrogging Sycamore: Harnessing 1432 GPUs for 7x Faster Quantum Random Circuit Sampling, June 2024. arXiv:2406.18889 [quant-ph]. 1

Appendix A

Details on the VQE ansatz state

In this appendix, we include the detailed calculations concerning the interpolated Hamiltonian of Eq. (2.3.13):

$$H(\alpha) = -\cos(\alpha) \left[X_0 Z_1 + Z_n X_{n+1} + \sum_{i=1}^n Z_{i-1} X_i Z_i \right] - \sin(\alpha) \sum_{i=1}^n X_i. \quad (\text{A.0.1})$$

and the ansatz state of cluster state with local translation-invariant transformations of Eq. (4.1.2):

$$|\Psi(\theta)\rangle = T(\theta) |C_{n+2}\rangle = \bigotimes_{i=1}^n T_i(\theta) |C_{n+2}\rangle := \left(\bigotimes_{i=1}^n \cos(\theta) I_i + \sin(\theta) X_i \right) |C_{n+2}\rangle. \quad (\text{A.0.2})$$

A.1 Perturbation theory calculation

We show here that the ansatz state agrees with the ground state of the interpolated Hamiltonian up to second order in perturbation theory. Rescaling the Hamiltonian by dividing out by $\cos(\alpha)$, we obtain:

$$H(\alpha) = - \left[X_0 Z_1 + Z_n X_{n+1} + \sum_{i=1}^n Z_{i-1} X_i Z_i \right] + \lambda \sum_{i=1}^n X_i = - \sum_{i=0}^{n+1} K_i + \lambda \sum_{i=1}^n X_i \quad (\text{A.1.1})$$

with $\lambda = -\tan(\alpha)$. It is worth noting that the perturbation expansion is only valid for $\alpha \ll 1$.

The eigenstates of the cluster state Hamiltonian (which form the basis for our perturbation theory expansion) we denote by $|\vec{x}\rangle$, with $x_i = 1$ if $K_i |\vec{x}\rangle = -|\vec{x}\rangle$ and $x_i = 0$ if $K_i |\vec{x}\rangle = +|\vec{x}\rangle$. In this notation $|\vec{0}\rangle = |C\rangle$ the cluster state. The energy of $|\vec{x}\rangle$ is $E_{\vec{x}} = -(n+2) + |\vec{x}|$ with $|\cdot|$ denoting the Hamming weight. For brevity, we write just the indices of \vec{x} that are nonzero - i.e. we would write $|(0,1,0,1,0,0)\rangle$ as $|1,3\rangle$. Note that since X_i (for any bulk i , i.e. all X_i s that appear in the perturbation) flips the sign of the stabilizers K_{i-1} and K_{i+1} , we have $X_i |C\rangle = |i-1, i+1\rangle$.

Zeroth order

The unperturbed ground state is just the cluster state $|\vec{0}\rangle = |C\rangle$.

First order

The first order correction to the ground state is given by [SN20]:

$$\begin{aligned}
\lambda \sum_{\vec{x} \neq 0} \frac{\langle \vec{x} | \sum_{i=1}^n X_i | \vec{0} \rangle}{E_{\vec{0}} - E_{\vec{x}}} |\vec{x}\rangle &= \lambda \sum_{i=1}^n \sum_{\vec{x} \neq 0} \frac{\langle \vec{x} | i-1, i+1 \rangle}{E_{\vec{0}} - E_{\vec{x}}} |\vec{x}\rangle \\
&= \lambda \sum_{i=1}^n \frac{1}{-(n+2) - [-(n+2) + 2]} |i-1, i+1\rangle \\
&= -\frac{\lambda}{2} \sum_{i=1}^n |i-1, i+1\rangle \\
&= -\frac{\lambda}{2} \sum_{i=1}^n X_i |C\rangle
\end{aligned} \tag{A.1.2}$$

Second order

The second order correction to the ground state is given by [SN20]:

$$\begin{aligned}
&\lambda^2 \left(\sum_{\vec{x} \neq \vec{0}} \sum_{\vec{y} \neq \vec{0}} \frac{\langle \vec{x} | \sum_{i=1}^n X_i | \vec{y} \rangle \langle \vec{y} | \sum_{j=1}^n X_j | \vec{0} \rangle}{(E_{\vec{0}} - E_{\vec{x}})(E_{\vec{0}} - E_{\vec{y}})} |\vec{x}\rangle - \sum_{\vec{x} \neq \vec{0}} \frac{\langle \vec{0} | \sum_{i=1}^n X_i | \vec{0} \rangle \langle \vec{x} | \sum_{j=1}^n X_j | \vec{0} \rangle}{(E_{\vec{0}} - E_{\vec{x}})^2} |\vec{x}\rangle \right) \\
&= \lambda^2 \left(\sum_{\vec{x} \neq \vec{0}} \sum_{\vec{y} \neq \vec{0}} \frac{\langle \vec{x} | \sum_{i=1}^n X_i | \vec{y} \rangle \langle \vec{y} | \sum_{j=1}^n |j-1, j+1\rangle}{(E_{\vec{0}} - E_{\vec{x}})(E_{\vec{0}} - E_{\vec{y}})} |\vec{x}\rangle - \sum_{\vec{x} \neq \vec{0}} \frac{0 \cdot \langle \vec{x} | \sum_{j=1}^n X_j | \vec{0} \rangle}{(E_{\vec{0}} - E_{\vec{x}})^2} |\vec{x}\rangle \right) \\
&= \lambda^2 \sum_{\vec{x} \neq \vec{0}} \sum_{j=1}^n \frac{\langle \vec{x} | \sum_{i=1}^n X_i | j-1, j+1 \rangle}{(E_{\vec{0}} - E_{\vec{x}})(-(n+2) - [-(n+2) + 2])} |\vec{x}\rangle \\
&= \lambda^2 \sum_{\vec{x} \neq \vec{0}} \sum_{j=i} \frac{\langle \vec{x} | \sum_{i=1}^n X_i | j-1, j+1 \rangle}{(E_{\vec{0}} - E_{\vec{x}})(-2)} |\vec{x}\rangle + \lambda^2 \sum_{\vec{x} \neq \vec{0}} \sum_{j \neq i} \frac{\langle \vec{x} | \sum_{i=1}^n X_i | j-1, j+1 \rangle}{(E_{\vec{0}} - E_{\vec{x}})(-2)} |\vec{x}\rangle \\
&= \lambda^2 n \frac{\langle \vec{x} | \vec{0} \rangle}{(E_{\vec{0}} - E_{\vec{x}})(-2)} |\vec{x}\rangle + \lambda^2 \sum_{\vec{x} \neq \vec{0}} \sum_{j \neq i} \sum_{i=1}^n \frac{\langle \vec{x} | j-1, j+1, i-1, i+1 \rangle}{(E_{\vec{0}} - E_{\vec{x}})(-2)} |\vec{x}\rangle \\
&= \lambda^2 \sum_{j \neq i} \sum_{i=1}^n \frac{1}{(-(n+2) - [-(n+2) + 4])(-2)} |j-1, j+1, i-1, i+1\rangle \\
&= \frac{\lambda^2}{8} \sum_{j \neq i} \sum_{i=1}^n |j-1, j+1, i-1, i+1\rangle \\
&= \frac{\lambda^2}{4} \sum_{j>i} \sum_{i=1}^n X_j X_i |C\rangle
\end{aligned} \tag{A.1.3}$$

Hence we have found to second order in perturbation theory (neglecting normalization):

$$|C\rangle - \frac{\lambda}{2} \sum_{i=1}^n X_i |C\rangle + \frac{\lambda^2}{4} \sum_{j>i} \sum_{i=1}^n X_j X_i |C\rangle \tag{A.1.4}$$

Which is consistent (to second order) with the state:

$$|\Psi(\lambda)\rangle = \bigotimes_{i=1}^n (I_i - \frac{\lambda}{2} X_i) |C\rangle = \bigotimes_{i=1}^n (I_i + \frac{\tan(\alpha)}{2} X_i) |C\rangle \quad (\text{A.1.5})$$

which up to rescaling by $\cos(\alpha)$ and a factor of 2 is precisely the ansatz state we have chosen.

A.2 VQE expectation value calculations

We here calculate the expectation value of the interpolated Hamiltonian for the ansatz state. Explicitly, we have:

$$\langle \Psi(\theta) | H(\alpha) | \Psi(\theta) \rangle = -\cos(\alpha) \sum_{i=0}^{n+1} \langle K_i \rangle_\theta - \sin(\alpha) \sum_{i=1}^n \langle X_i \rangle_\theta \quad (\text{A.2.1})$$

so we only need consider calculating the expectation values of the individual terms.

We will find it convenient to evaluate these expectation values in the density matrix picture. For a given stabilizer state $|\psi\rangle$ on n qubits with stabilizer group G , the density matrix can be written as:

$$\rho_\psi = \frac{1}{2^n} \sum_{g \in G} g. \quad (\text{A.2.2})$$

This follows because $\rho_\psi = |\psi\rangle\langle\psi|$ with $g|\psi\rangle = |\psi\rangle$ for any $g \in G$, hence the defining condition of the density matrix must be that $g\rho_\psi = g|\psi\rangle\langle\psi| = |\psi\rangle\langle\psi| = \rho_\psi$. Multiplication by a group element maps the stabilizer group into itself, so the sum remains invariant under multiplication by a group element, i.e. $g' \sum_{g \in G} g = \sum_{g \in G} g$ as required. The $\frac{1}{2^n}$ factor makes the above a valid density matrix as the identity matrix is a stabilizer of any state, has trace $\text{Tr}(I) = 2^n$, and is the only Pauli string with nonzero trace. We will use this fact frequently in the following calculations.

Thus, for the $n + 2$ qubit cluster chain we can write:

$$\rho_C = \frac{1}{2^n} \sum_{g \in G_C} g \quad (\text{A.2.3})$$

where G_C is the stabilizer group generated by the cluster state stabilizers K_i for $i \in 0, \dots, n + 1$. In this form, we can write the density operator of the ansatz state as $T^\dagger(\theta)\rho_C T(\theta)$. The expectation value of an operator A can be calculated as:

$$\langle A \rangle_\theta = \frac{\text{Tr}(AT^\dagger(\theta)\rho_C T(\theta))}{\text{Tr}(T^\dagger(\theta)\rho_C T(\theta))} \quad (\text{A.2.4})$$

where we include the denominator as the normalization of $T^\dagger(\theta)\rho_C T(\theta)$ is not immediately clear. Note that since $T(\theta)$ is real, $T^\dagger(\theta) = T(\theta)$, and using this and the cyclicity of the trace we may write:

$$\langle A \rangle_\theta = \frac{\text{Tr}(AT(\theta)\rho_C T(\theta))}{\text{Tr}(\rho_C (T(\theta))^2)} \quad (\text{A.2.5})$$

The denominator is common to all the proceeding calculations so we begin with it. We have:

$$(T(\theta))^2 = \left(\bigotimes_{i=1}^n \cos(\theta)I_i + \sin(\theta)X_i \right)^2 = \bigotimes_{i=1}^n I_i + 2 \cos(\theta) \sin(\theta) X_i \quad (\text{A.2.6})$$

There are no stabilizers of $|C\rangle$ that contain only Pauli-Xs save for the symmetry $X_0 I_1 X_2 \dots X_{n-1} I_n X_{n+1}$, however $T(\theta)$ does not contain X_0 or X_{n+1} . Hence, any part of $T(\theta)$ with Pauli-X terms that hits $\sum_{g \in G_C} g$ will have surviving Xs and be traceless. Therefore the only term that survives is the identity term, which leaves ρ_C invariant. Hence:

$$\text{Tr}(\rho_C (T(\theta))^2) = \text{Tr}(\rho_C) = 1 \quad (\text{A.2.7})$$

and so the denominator drops out - $T(\theta)$ preserves the normalization of the cluster state.

Local magnetic field

Let $A = X_i$ for $i = 1, 1, \dots, n+1$. Since X_i commutes with T , the expectation value becomes:

$$\langle X_i \rangle_\theta = \text{Tr}(X_i T(\theta) \rho_C T(\theta)) = \text{Tr}(X_i \rho_C (T(\theta))^2) \quad (\text{A.2.8})$$

Since ρ_C contains no stabilizers with just a single X_i term, $X_i \rho_C$ is traceless. The only term that survives in the above expression is that of $(T(\theta))^2$ that cancels the X_i , i.e. The $2 \cos(\theta) \sin(\theta) X_i$ term. Therefore:

$$\langle X_i \rangle_\theta = \text{Tr}(2 \cos(\theta) \sin(\theta) \rho_C) = 2 \cos(\theta) \sin(\theta). \quad (\text{A.2.9})$$

Boundary cluster stabilizer

Let $A = K_i$ for $i = 0, 1, n, n+1$. For this calculation we take $i = 0$ so $A = X_0 Z_1$. The Z_1 flips the sign of the $T_1(\theta)$, while the rest of the T_i s commute, so:

$$\begin{aligned} \langle K_0 \rangle_\theta &= \text{Tr}(K_0 T(\theta) \rho_C T(\theta)) \\ &= \text{Tr}(K_0 \rho_C (\cos(\theta)I_1 + \sin(\theta)X_1)(\cos(\theta)I_1 - \sin(\theta)X_1) \otimes (\bigotimes_{i=2}^n I_i + 2 \cos(\theta) \sin(\theta) X_i)) \\ &= \text{Tr}(K_0 \rho_C (\cos^2(\theta) - \sin^2(\theta))I_1) \otimes (\bigotimes_{i=2}^n I_i + 2 \cos(\theta) \sin(\theta) X_i) \end{aligned} \quad (\text{A.2.10})$$

K_0 is just a cluster state stabilizer generator and thus can be absorbed into ρ_C :

$$\langle K_0 \rangle_\theta = (\cos^2(\theta) - \sin^2(\theta)) \text{Tr}(\rho_C I_1 \otimes (\bigotimes_{i=2}^n I_i + 2 \cos(\theta) \sin(\theta) X_i)) \quad (\text{A.2.11})$$

As before, the only term that is not traceless is the identity term, and hence:

$$\langle K_0 \rangle_\theta = (\cos^2(\theta) - \sin^2(\theta)) \text{Tr}(\rho_C) = \cos^2(\theta) - \sin^2(\theta) \quad (\text{A.2.12})$$

For all of $i = 0, 1, n, n+1$ only one $T_i(\theta)$ gets flipped, and so each have the same expectation value.

Note that since this argument only relies on the fact that one $T_i(\theta)$ is flipped by a Z_i , it generalizes also to any string order parameter which starts at any bulk even qubit and ends at the boundary (Eq. (2.3.11a)), i.e.:

$$\sigma_k(g_{01}) = \langle Z_k X_{k+1} I_{k+2} \dots I_{n-1} X_n Z_{n+1} \rangle_\theta = \cos^2(\theta) - \sin^2(\theta) \quad \forall \text{ bulk even } k \quad (\text{A.2.13})$$

Thus $\sigma_k(g_{01}) = \sigma = \cos^2(\theta) - \sin^2(\theta)$ for all bulk k , and which means the simplifying assumption we made in the experimental prediction of Section 3.3 holds for this ansatz state.

Bulk cluster stabilizer

Let $A = K_i$ for $i = 2, 3, \dots, n-2, n-1$. The calculation proceeds exactly as above, except now the Z_{i-1}, Z_{i+1} of the K_i flips the sign of not one but two $T_i(\theta)$ s. Thus the result is the same with an extra factor of $\cos^2(\theta) - \sin^2(\theta)$ that comes from the sign flip, i.e.:

$$\langle K_i \rangle_\theta = (\cos^2(\theta) - \sin^2(\theta))^2 \quad (\text{A.2.14})$$

Thus we conclude:

$$\langle X_i \rangle_\theta = 2 \cos(\theta) \sin(\theta) \quad (\text{A.2.15a})$$

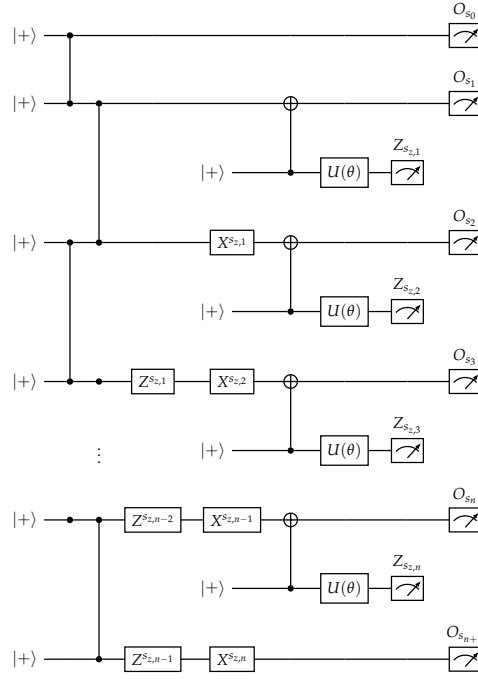
$$\langle K_i \rangle_\theta = \begin{cases} \cos^2(\theta) - \sin^2(\theta) & i = 0, 1, n, n+1 \\ (\cos^2(\theta) - \sin^2(\theta))^2 & i = 2, 3, \dots, n-1 \end{cases} \quad (\text{A.2.15b})$$

And so:

$$\langle H(\alpha) \rangle_\theta = -\cos(\alpha) \left(4(\cos^2(\theta) - \sin^2(\theta)) + (n-2)(\cos^2(\theta) - \sin^2(\theta))^2 \right) - \sin(\alpha) 2n \cos(\theta) \sin(\theta) \quad (\text{A.2.16})$$

A.3 VQE circuit derivations

Our starting point for the quantum circuit to measure the observables $\langle X_i \rangle_\theta / \langle K_i \rangle_\theta$ is given in (A.3.1).



(A.3.1)

The first portion of the circuit corresponds to the preparation of the ansatz state $|\Psi(\theta)\rangle$, starting with the preparation of the cluster state and then an ancilla-based construction to apply $T(\theta) = \bigotimes_{i=1}^n T_i(\theta)$. The ancilla based construction is probabilistic, with $s_{z,i} = +1$ corresponding to an implementation of $T_i(\theta)$ and $s_{z,i} = -1$ corresponding to an implementation of $T_i(-\theta)X_i$. The ancilla-outcome dependent Paulis $X^{s_{z,i}}Z^{s_{z,i-1}}$ are present to allow for the correct circuit to be obtained via an equivalence transformation which we soon describe. At the end of the circuit we choose observables O_0, \dots, O_{n+1} depending on what we wish to measure. The $U(\theta)$ present in the ancilla is defined as:

$$U(\theta) := RY(2\theta) = \cos(\theta)I - i\sin(\theta)Y. \quad (\text{A.3.2})$$

The state preparation seems a priori probabilistic, with exponentially diminishing success probability in the length of the chain. However, it can be made deterministic by considering the following equivalence transformation - on each bulk site with the ancilla construction, we pull out the cluster stabilizer $Z_i X_{i+1} Z_{i+2}$ from the cluster state (the $X^{s_{z,i-1}} Z^{s_{z,i-2}}$ in the original circuit needed to cancel out all but the Z_i). This results in the Equivalent circuit of Fig. A.1.

In this equivalent circuit, the remaining $Z_{s_{z,i}}$ can be pulled past the CNOT gates on a given line to correct the ancilla measurement, leading to the correct (deterministic) implementation of $T_i(\theta)$ on each site regardless of the ancilla measurement outcome. Thus we can use this general circuit (with deterministic state preparation) to derive the protocols to measure $\langle X_i \rangle_\theta$ and $\langle K_i \rangle_\theta$ as given by Tables 4.1-4.3.

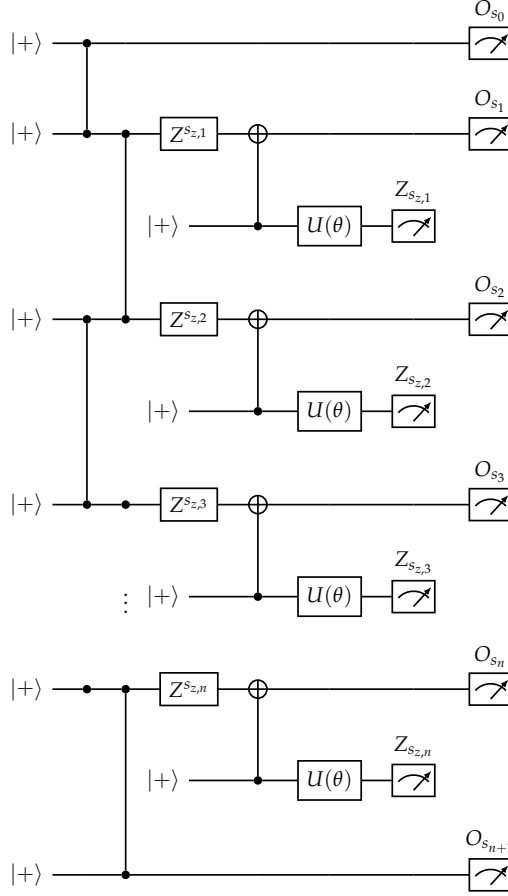


Figure A.1: Full (deterministic) circuit for measuring VQE observables. We start by constructing the cluster state, followed by an ancilla-based construction to place the non-unitary gates $T_i(\theta)$ on each bulk site. The $Z_{s_{z,i}}$ allow for a deterministic implementation of the non-unitary gate. The observables at the end can be chosen to be the appropriate Pauli string to measure $\langle X_i \rangle_\theta$ and $\langle K_i \rangle_\theta$.

A.3.1 Derivation of $\langle X_i \rangle_\theta$ protocol

We start by taking $O_{s_i} = X_{s_i}$ for each qubit in the circuit of Fig. A.1. We may then pull the X-measurement through the CNOT of the ancilla construction, which decouples the two qubits:

$$\begin{array}{c}
 \text{---} [Z^{s_{z,i}}] \text{---} \oplus \text{---} X_{s_i} \\
 |+\rangle \text{---} \bullet \text{---} U(\theta) \text{---} Z_{s_{z,i}} \\
 \end{array} = \begin{array}{c}
 X_{s_i+s_{z,i}} \\
 |+\rangle \text{---} Z^{s_i} \text{---} U(\theta) \text{---} Z_{s_{z,i}}
 \end{array} \quad (\text{A.3.3})$$

Furthermore on the every disconnected ancilla we have:

$$|+\rangle \text{---} Z^{s_i} \text{---} U(\theta) \text{---} Z_{s_{z,i}} = |+\rangle \text{---} Y^{s_i} \text{---} U(\theta) \text{---} Z_{s_{z,i}} = |+\rangle \text{---} U(\theta) \text{---} Z_{s'_i} \quad (\text{A.3.4})$$

where we pull X^{s_i} out of $|+\rangle$ to make Y^{s_i} which then commutes with $U(\theta) = RY(2\theta)$ and can be pushed into the measurement, where we have defined:

$$s'_i = s_i + s_{z,i}. \quad (\text{A.3.5})$$

Looking at the remaining circuit of $n + 1$ qubits, it is simply a sequence of n half-teleportations which collapses into a single qubit circuit:

$$\begin{array}{c}
 X_{s_0} \\
 + \text{---} \bullet \text{---} \text{---} \\
 X_{s'_1} \\
 + \text{---} \bullet \text{---} \bullet \text{---} \text{---} \\
 X_{s'_2} \\
 + \text{---} \bullet \text{---} \bullet \text{---} \text{---} \\
 \vdots \\
 X_{s'_n} \\
 + \text{---} \bullet \text{---} \bullet \text{---} \text{---} \\
 X_{s_{n+1}} \\
 + \text{---} \bullet \text{---} \bullet \text{---} \text{---}
 \end{array} = |+\rangle \text{---} Z^{s_1} \text{---} H \text{---} Z^{s'_2} \text{---} H \text{---} \dots \text{---} H \text{---} Z^{s'_n} \text{---} H \text{---} Z_{s_{n+1}} \quad (\text{A.3.6})$$

which reduces to:

$$|+\rangle \text{---} X_{s_0+s'_2+s'_4+\dots+s'_{n-1}+s_{n+1}} \quad (\text{A.3.7})$$

However, this is simply the statement that $s_0 + s'_2 + s'_4 + \dots + s'_{n-1} + s_{n+1} = 0$, which is something that already follows from the $\mathbb{Z}_2 \times \mathbb{Z}_2$ symmetry of the state! So, this circuit does not need to be run. As such to measure the local magnetic field we only need to restrict our attention to the disconnected ancilla qubits, with the magnetic field measurement at site i given by:

$$|+\rangle \text{ --- } \boxed{U(\theta)} \text{ --- } \boxed{\text{meter}} \quad Z_{s'_i} \quad (\text{A.3.8})$$

which is precisely the circuit that appears in Table 4.1.

A.3.2 Tracing lemmas

Before deriving the $\langle K_i \rangle_\theta$ protocols, we prove a useful Lemma in two steps.

Lemma 1 (Cluster state tracing). Tracing out the boundary qubit of a cluster chain removes it and leaves a Pauli-Z error on the neighbouring qubit with probability one half.

Proof. WLOG let us trace out the zeroth/leftmost qubit of a cluster chain and see its effect on the rest of the state. Our initial state is $\rho_{0,1,\dots,n+1}^C = |C_{n+2}\rangle\langle C_{n+2}|$. We now trace out the zeroth qubit, taking the partial trace in the computational basis, i.e.:

$$\text{Tr}_0(\rho_{0,\dots,n+1}^C) = \langle 0|_0 \rho_{0,\dots,n+1}^C |0\rangle_0 + \langle 1|_0 \rho_{0,\dots,n+1}^C |1\rangle_0 \quad (\text{A.3.9})$$

The first term corresponds to a Z-measurement on the zeroth qubit with enforced outcome of $Z = 0$, which corresponds to:

$$\Pi_0 |C_{n+1}\rangle = \Pi_0 \text{CZ}_{0,1} |+\rangle_0 \otimes |C_n\rangle = \text{CZ}_{0,1} \Pi_0 |+\rangle_0 \otimes |C_n\rangle = \text{CZ}_{0,1} |0\rangle_0 \otimes |C_n\rangle = |0\rangle_0 \otimes |C_n\rangle \quad (\text{A.3.10})$$

where in the second equality we commute the Z-measurement projector with the CZ, and in the last equality we use the fact that a controlled gate with $|0\rangle$ as the control does nothing. We are then left with $|C_n\rangle$ on the remainder of the chain. The probability of this occurring is simply $|\langle 0|+\rangle|^2 = \frac{1}{2}$. Hence:

$$\langle 0|_0 \rho_{0,\dots,n+1}^C |0\rangle_0 = \frac{1}{2} \rho_{1,\dots,n+1}^C \quad (\text{A.3.11})$$

To compute the other term, we can simply pull out a cluster state stabilizer:

$$\langle 1|_0 \rho_{0,\dots,n+1}^C |1\rangle_0 = \langle 1|_0 X_0 Z_1 \rho_{0,\dots,n+1}^C X_0 Z_1 |1\rangle_0 = Z_1 \langle 0|_0 \rho_{0,\dots,n+1}^C |0\rangle_0 Z_1 = \frac{1}{2} Z_1 \rho_{1,\dots,n+1}^C Z_1. \quad (\text{A.3.12})$$

where in the last equality we apply Eq. (A.3.11). Hence:

$$\text{Tr}_0(\rho_{0,\dots,n+1}^C) = \frac{1}{2} \rho_{1,\dots,n+1}^C + \frac{1}{2} Z_1 \rho_{1,\dots,n+1}^C Z_1 \quad (\text{A.3.13})$$

as claimed. \square

Note we can recursively apply the above argument to trace out any number $m < n + 1$ qubits from one end of an $n + 1$ -qubit cluster chain, leaving a $n + 1 - m$ length cluster chain with a probabilistic Z on the boundary.

Lemma 2. Tracing out $m < n + 1$ qubits from the boundary of the ansatz chain of Eq. (4.1.2) removes the qubits and leaves a Pauli-Z error on the remaining boundary qubit with probability one half.

Proof. If $m = 1$, then the argument reduces to that of the previous Lemma. Let us consider the case where $m > 1$. Applying the previous Lemma, after tracing out the zeroth qubit our state is the mixed state with a Pauli error on qubit 1 with probability one half:

$$\rho_{1,\dots,n+1} = \frac{1}{2} \left(\bigotimes_{i=1}^n T_i(\theta) \rho_{1,\dots,n+1}^C \bigotimes_{i=1}^n T_i(\theta) \right) + \frac{1}{2} \left(\bigotimes_{i=1}^n T_i(\theta) Z_1 \rho_{1,\dots,n+1}^C Z_1 \bigotimes_{i=1}^n T_i(\theta) \right) \quad (\text{A.3.14})$$

Now, we trace out qubit 1, taking the partial trace in the X-basis. We note that:

$$T_i(\theta) |\pm\rangle_i = (\cos \theta I_i + \sin \theta X_i) |\pm\rangle_i = (\cos \theta \pm \sin \theta) |\pm\rangle_i \quad (\text{A.3.15})$$

And so:

$$\begin{aligned} & \text{Tr}_1(\rho_{1,\dots,n+1}) \\ &= \langle + |_1 \rho_{1,\dots,n+1} | + \rangle_1 + \langle - |_1 \rho_{1,\dots,n+1} | - \rangle_1 \\ &= \langle + |_1 \frac{1}{2} \bigotimes_{i=1}^n T_i(\theta) \rho_{1,\dots,n+1}^C \bigotimes_{i=1}^n T_i(\theta) | + \rangle + \langle + |_1 \frac{1}{2} \bigotimes_{i=1}^n T_i(\theta) Z_2 \rho_{1,\dots,n+1}^C Z_2 \bigotimes_{i=1}^n T_i(\theta) | + \rangle \\ &+ \langle - |_1 \frac{1}{2} \bigotimes_{i=1}^n T_i(\theta) \rho_{1,\dots,n+1}^C \bigotimes_{i=1}^n T_i(\theta) | - \rangle + \langle - |_1 \frac{1}{2} \bigotimes_{i=1}^n T_i(\theta) Z_2 \rho_{1,\dots,n+1}^C Z_2 \bigotimes_{i=1}^n T_i(\theta) | - \rangle \\ &= \frac{(\cos \theta + \sin \theta)^2}{2} \left(\langle + |_2 \bigotimes_{i=2}^n T_i(\theta) \rho_{1,\dots,n+1}^C \bigotimes_{i=2}^n T_i(\theta) | + \rangle + \langle - |_2 \bigotimes_{i=2}^n T_i(\theta) \rho_{1,\dots,n+1}^C \bigotimes_{i=2}^n T_i(\theta) | - \rangle \right) \\ &+ \frac{(\cos \theta - \sin \theta)^2}{2} \left(\langle - |_2 \bigotimes_{i=2}^n T_i(\theta) \rho_{1,\dots,n+1}^C \bigotimes_{i=2}^n T_i(\theta) | - \rangle + \langle + |_2 \bigotimes_{i=2}^n T_i(\theta) \rho_{1,\dots,n+1}^C \bigotimes_{i=2}^n T_i(\theta) | + \rangle \right) \end{aligned} \quad (\text{A.3.16})$$

where in the last equality we use the eigenvalue relation for T , as well as that $Z |\pm\rangle = |\mp\rangle$. Now, noting that $(\cos \theta + \sin \theta)^2 + (\cos \theta - \sin \theta)^2 = 2(\cos^2 \theta + \sin^2 \theta) = 2$, combining the first/fourth term and the second/third term we find:

$$\text{Tr}_1(\rho_{1,\dots,n+1}) = \langle + |_2 \bigotimes_{i=2}^n T_i(\theta) \rho_{1,\dots,n+1}^C \bigotimes_{i=2}^n T_i(\theta) | + \rangle + \langle - |_2 \bigotimes_{i=2}^n T_i(\theta) \rho_{1,\dots,n+1}^C \bigotimes_{i=2}^n T_i(\theta) | - \rangle$$

But now note that the expression on the RHS is just taking the partial trace of a cluster state qubit (there is no longer any $T_i(\theta)$ operator being applied on qubit 1). Hence, our previous Lemma applies, and tracing out the qubit 1 now just amounts to removing it, and placing a Pauli Z error on qubit 2 with probability $\frac{1}{2}$:

$$\text{Tr}_1(\rho_{1,\dots,n+1}) = \frac{1}{2} \bigotimes_{i=2}^n T_i(\theta) \rho_{2,\dots,n+1}^C \bigotimes_{i=2}^n T_i(\theta) + \frac{1}{2} \bigotimes_{i=2}^n T_i(\theta) Z_2 \rho_{2,\dots,n+1}^C Z_2 \bigotimes_{i=2}^n T_i(\theta)$$

Now, noting that this expression is identical to what we started with (just that we have now removed one more qubit, and the probabilistic Pauli Z error has shifted to the next qubit over), we can apply the above tracing argument m times until m qubits have been removed. Doing so, we will obtain:

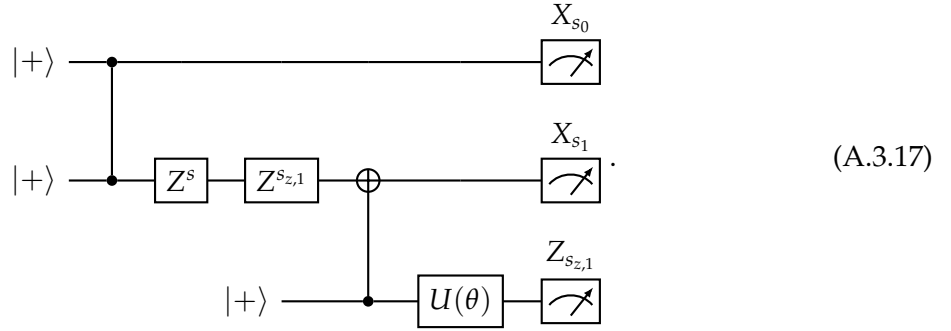
$$\text{Tr}_{0,\dots,m-1}(\rho_{0,\dots,n+1}) = \frac{1}{2} \left(\bigotimes_{i=m}^n T_i(\theta) \rho_{m,\dots,n+1}^C \bigotimes_{i=m}^n T_i(\theta) \right) + \frac{1}{2} \left(\bigotimes_{i=m}^n T_i(\theta) Z_m \rho_{m,\dots,n+1}^C Z_m \bigotimes_{i=m}^{n+1} T_i(\theta) \right).$$

which was the claimed formula. \square

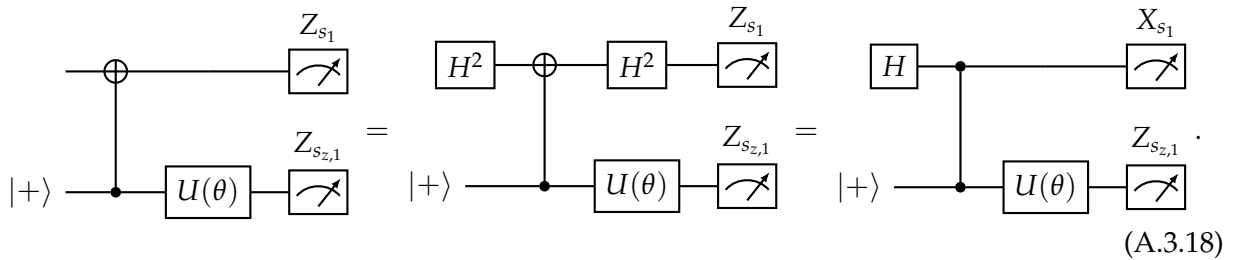
Lemma in hand, we now derive the $\langle K_i \rangle_\theta$ circuits.

A.3.3 Derivation of boundary $\langle K_i \rangle_\theta$ protocol

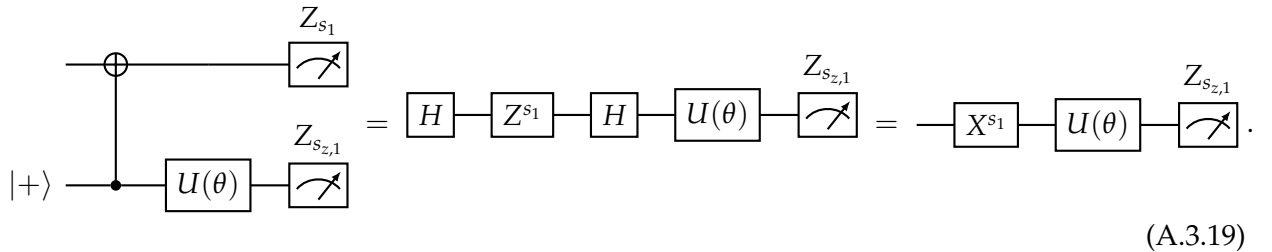
First we study the two-body boundary cluster state stabilizer, and take $O_{s_0} = X_{s_0}$ and $O_{s_1} = Z_{s_1}$ in the circuit of Fig. A.1. We then apply tracing Lemma 2 above to remove qubits $2, \dots, n+1$, leaving behind a probabilistic Z-error Z^s on qubit 1:



Note that we can insert $H^2 = I$ twice around the CNOT, yielding the following sequence of identities:



This we recognize as another half-teleportation and so:



Further, we notice another half-teleportation of qubit 0 in Eq. (A.3.17), which yields the overall single-qubit circuit:

$$|+\rangle \xrightarrow{Z^{s_0}} \xrightarrow{H} \xrightarrow{Z^s} \xrightarrow{Z^{s_{z,1}}} \xrightarrow{X^{s_1}} \xrightarrow{U(\theta)} \xrightarrow{Z^{s_{z,1}}} . \quad (\text{A.3.20})$$

$Z^s, Z^{s_{z,1}}$ act on a Z-eigenstate and hence have no effect on the state; we may therefore remove them. The net result is:

$$|s_0 + s_1\rangle \xrightarrow{U(\theta)} \xrightarrow{Z^{s_{z,1}}} \quad (\text{A.3.21})$$

which precisely measures $(-1)^{s_0+s_1+s_{z,1}} = (-1)^{s_0+s'_1} = \langle X_1 Z_2 \rangle$, and hence we can equivalently write:

$$|0\rangle \xrightarrow{U(\theta)} \xrightarrow{Z^{s_0+s'_1}} \quad (\text{A.3.22})$$

which is precisely the circuit that appears in Table 4.2.

We also show that the other (3-body) boundary cluster stabilizer term has an equivalent final circuit. We start by taking $O_{s_0} = Z_{s_0}, O_{s_1} = X_{s_1}, O_{s_2} = Z_{s_2}$ in the circuit of Fig. A.1, again applying tracing Lemma 2 above to remove qubits $3, \dots, n+1$, leaving behind a probabilistic Z-error Z^s on qubit 2:

$$(\text{A.3.23})$$

On qubit 1 + ancilla we use the same decoupling as we did in the $\langle X_i \rangle_\theta$ derivation (moving the X measurement through the CNOT and half-teleportation), and on qubit 2 + ancilla we apply the same simplification as in the two-body boundary cluster stabilizer measurement (insertions

of $H^2 = I$ and half-teleportation), which yields:

$$(A.3.24)$$

Inserting $H^2 = I$ after the CZ gate and transforming the $Z^{s'_1} \mapsto HZ^{s'_1}H = X^{s'_1}$, we obtain:

$$(A.3.25)$$

Now, since $H_1 CZ_{0,1} |+ \rangle_0 \otimes |+ \rangle_1 = \frac{|00\rangle + |11\rangle}{\sqrt{2}}$, measuring the qubit 0 in Z forces the second qubit to be the same state, and so:

$$(A.3.26)$$

$Z^s, Z^{s_{z,2}}$ can be removed as they act on a computational basis state, and the Xs can be absorbed so:

$$(A.3.27)$$

which precisely measures $(-1)^{s_0 + s'_1 + s_2 + s_{z,2}} = (-1)^{s_0 + s'_1 + s'_2} = \langle Z_0 X_1 Z_2 \rangle$, and hence we can write:

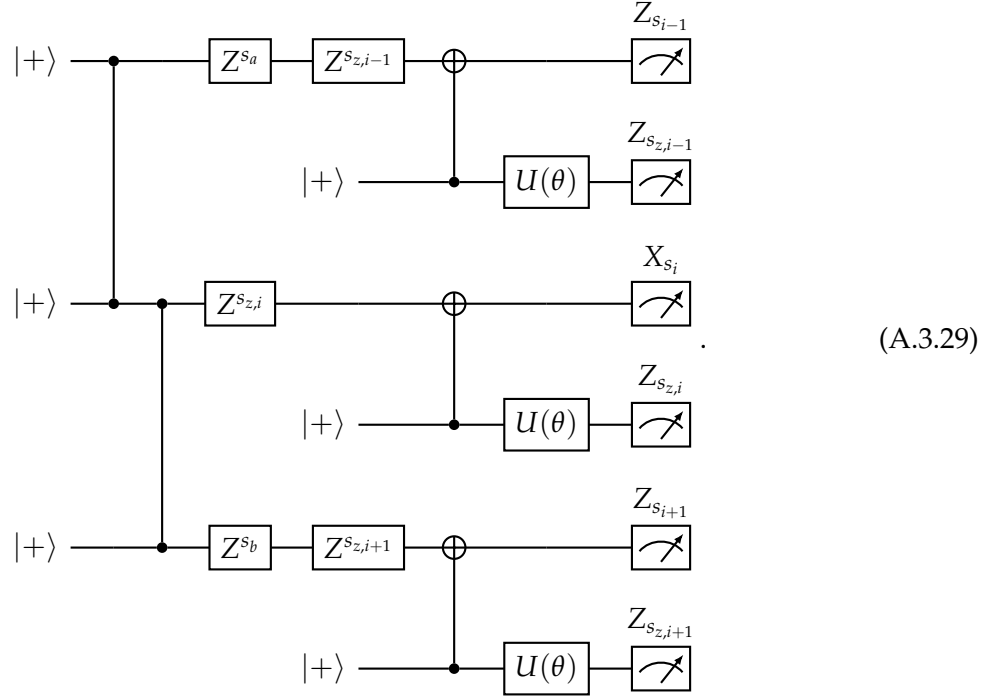
$$(A.3.28)$$

This circuit is identical to that obtained from our previous simplification.

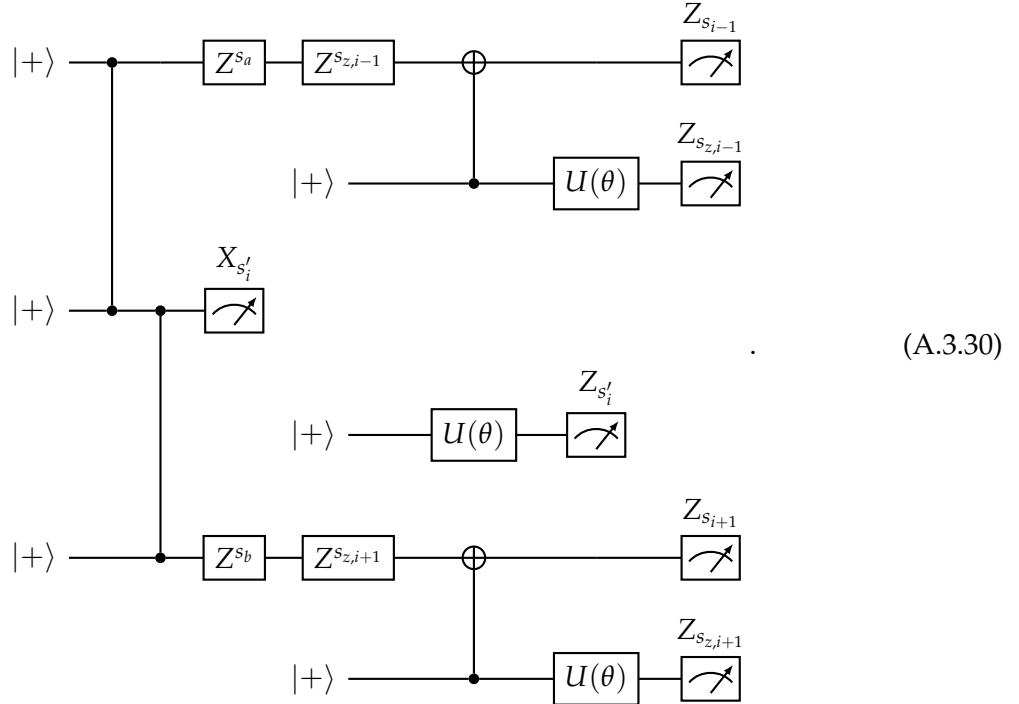
A.3.4 Derivation of bulk $\langle K_i \rangle_\theta$ protocol

We take $O_{s_{i-1}} = Z_{s_{i-1}}$, $O_{s_i} = X_{s_{i+1}}$, and $O_{s_{i+1}} = Z_{s_{i+1}}$ in the circuit of Fig. A.1, where $2 \leq i \leq n-1$. We then apply tracing Lemma 2 above to remove qubits $0, \dots, i-2$ and $i+2, \dots, n+2$, leaving

behind a probabilistic Z-error Z^{s_a} on qubit $i - 1$ and Z^{s_b} on qubit $i + 1$:

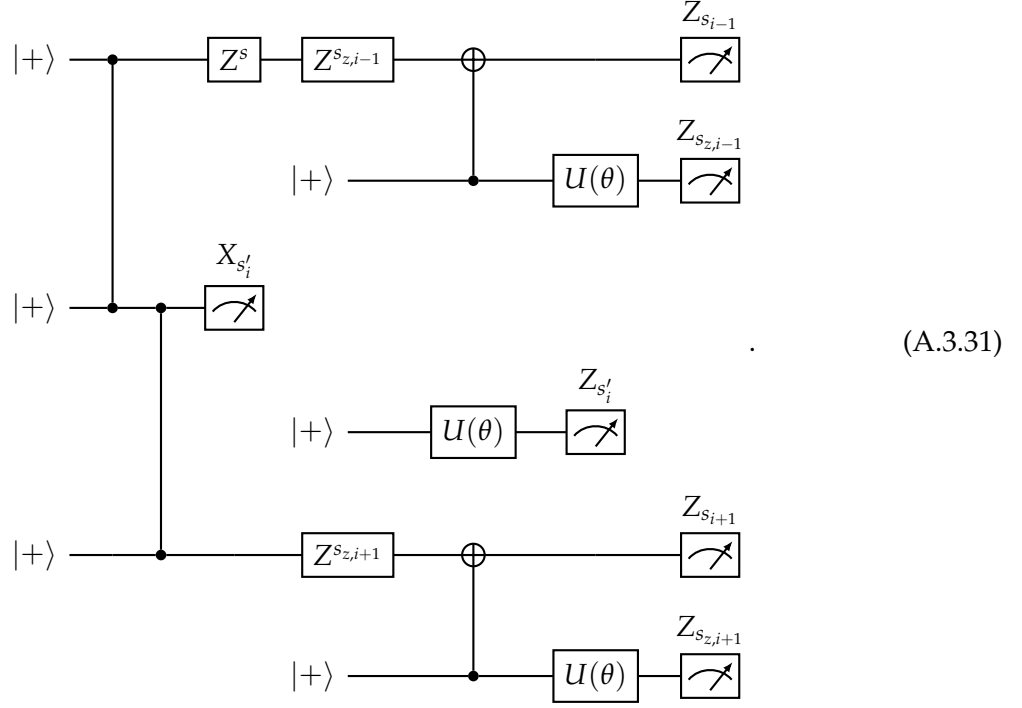


As we did previously, we decouple the ancilla on the i th qubit:

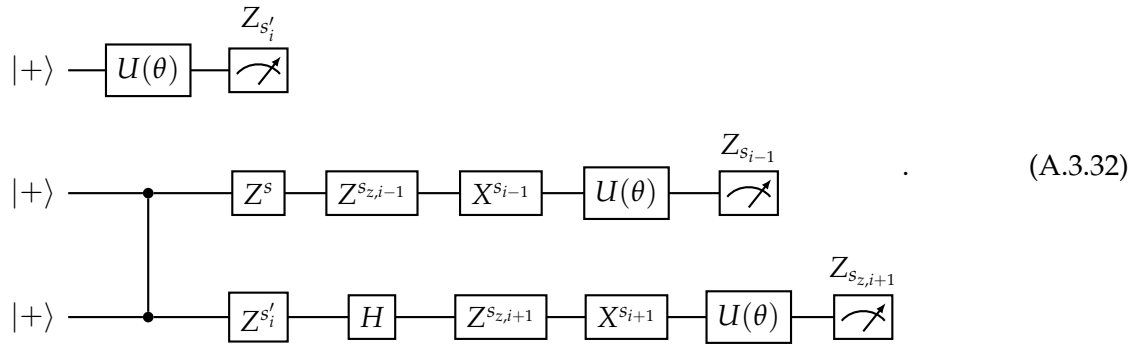


Note that currently we have s_a, s_b as 0/1 with 50/50 probability each. In the case where $s_b = 1$ we can pull out a cluster stabilizer $Z_{s_{i-1}} X_{s_i} Z_{s_{i+1}}$ and convert Z^{s_b} to Z^{s_a} (the X part of the stabilizer

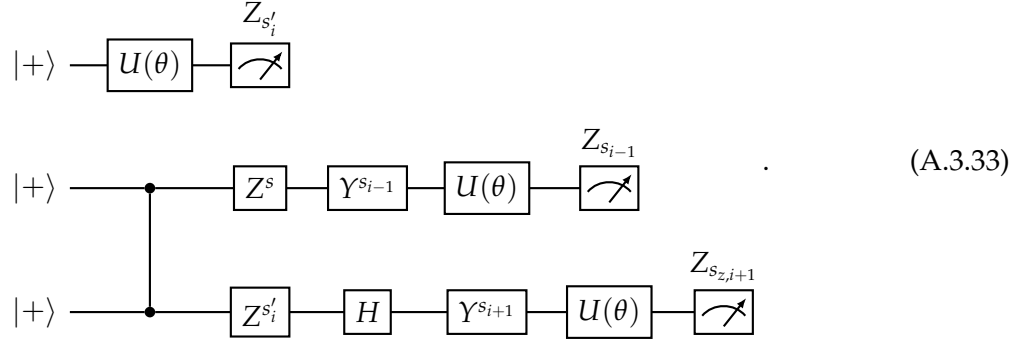
simply commutes with the measurement), so we can simply replace the two probabilistic Z s with a single one Z^s on the $i - 1$ th qubit:



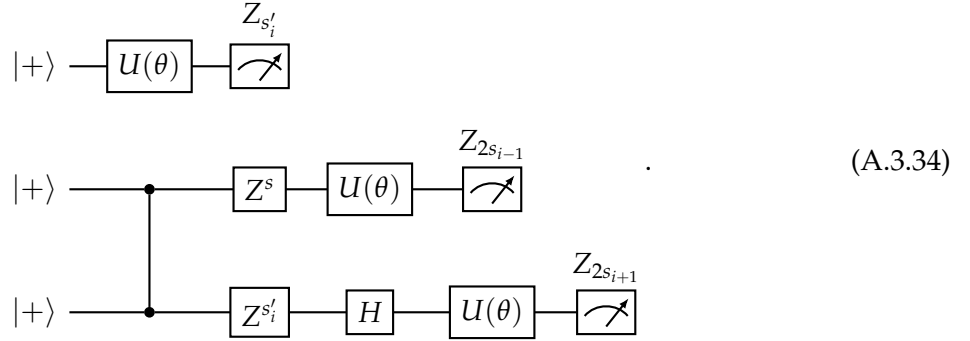
Now we may simplify the Z measurements via the already seen technique of inserting $H^2 = I$ and performing half-teleportations, and also half teleport qubit i . This leaves us with:



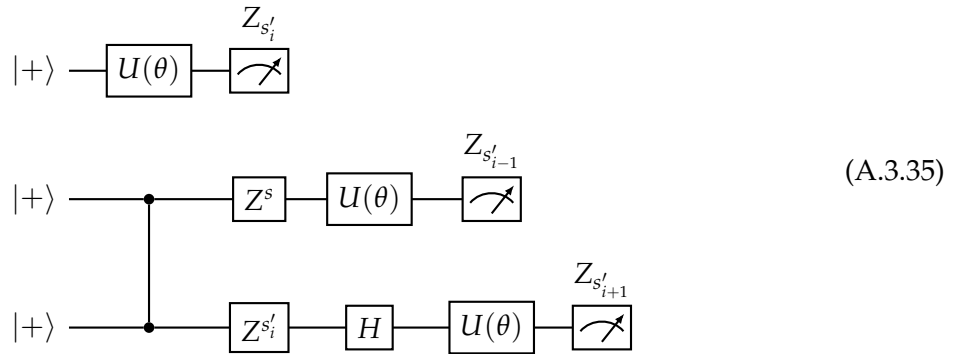
Now, suppose that $s_{z,i-1} = s_{i-1}$ and $s_{z,i+1} = s_{i+1}$ so that the Z/X gates on each of the two qubit lines can be combined into a Y :



Then, since Y commutes with $U(\theta) = RY(2\theta)$ we can commute it past U and through to the measurement, from which we obtain:



Thus, under the assumption that $s_{z,i-1} = s_{i-1}$, we measure $s'_{i-1} = 2s_{i-1} = 0$ (and the same for $i + 1$). In other words, the final measurements on the circuit lines here correspond to measurements of s'_{i-1}/s'_{i+1} , with 0 corresponding to the $s_{z,i-1} = s_{i-1}$ condition and 1 corresponding to the $s_{z,i-1} \neq s_{i-1}$ condition, and thus we conclude with the circuits:



from which we can obtain $\langle Z_{i-1} X_i Z_{i+1} \rangle = \langle (-1)^{s'_{i-1} + s'_i + s'_{i+1}} \rangle$. These are the circuits that appear in Table 4.3 and so we conclude.

A.4 Phase transition calculation

Rewriting the expectation value of Eq. (A.2.16) in terms of $x = 2 \sin(\theta) \cos(\theta)$, we obtain:

$$\langle H(\alpha) \rangle_x = -\cos(\alpha) \left(4\sqrt{1-x^2} + (n-2)(1-x^2) \right) - \sin(\alpha)nx \quad (\text{A.4.1})$$

Taking the $n \rightarrow \infty$ limit, only the terms proportional to n remain:

$$\lim_{n \rightarrow \infty} \langle H(\alpha) \rangle_x = -n \left[\cos(\alpha)(1-x^2) + \sin(\alpha)x \right] \quad (\text{A.4.2})$$

So to minimize the energy we want to find the x that minimizes the expression in the brackets above - taking the derivative w.r.t. x we find:

$$\frac{d}{dx} \left[\cos(\alpha)(1-x^2) + \sin(\alpha)x \right] = 2\cos(\alpha)x - \sin(\alpha) \quad (\text{A.4.3})$$

Setting the above to zero to find the minimizing x (noting that for the α s of interest, namely $0 \leq \alpha \leq \pi/2$ that the second derivative is positive and hence the extrema is really a minima) we find:

$$x_{\min}(\alpha) = \frac{1}{2} \tan(\alpha) \quad (\text{A.4.4})$$

Since $x = 2 \sin(\theta) \cos(\theta)$, there is the restriction that $-1 \leq x \leq 1$ - in particular the above minima only holds for $\alpha < \arctan(2)$. Above $\arctan(\alpha)$ the minimizing permissible x will be as close to $\frac{1}{2} \tan(\alpha)$ as possible, i.e. the largest x possible - 1. Hence, in the $N \rightarrow \infty$ limit the minimizing x is:

$$x_{\min}(\alpha) = \begin{cases} \frac{1}{2} \tan(\alpha) & 0 \leq \alpha \leq \arctan(2) \\ 1 & \arctan(2) < \alpha \leq \pi/2 \end{cases} \quad (\text{A.4.5})$$

Hence, we find that the ansatz states of Eq. (4.1.2) indeed exhibit a phase transition, albeit at $\alpha = \arctan(2)$ instead of $\alpha = \pi/4$ as is the case for the cluster phase/the true ground states of Eq. (2.3.13).

Appendix B

Details on the XX -rotated cluster state

In this appendix, we include the detailed calculations concerning the state with length scale of Eq. (4.1.10):

$$|\Omega(\phi)\rangle = V(\phi) |C_{n+2}\rangle = RX_1(\phi)RX_2(\phi)RX_{n-1}(\phi)RX_n(\phi) \prod_{i=1}^{n-2} RXX_{i,i+2}(\phi) |C_{n+2}\rangle. \quad (\text{B.0.1})$$

B.1 Proof of string order parameter convexity

We consider $|\Omega(\phi)\rangle$ on ≥ 11 qubits. We can analytically calculate the string order parameters Eq. (2.3.14):

$$\sigma_{k,l} = \langle \Omega(\phi) | Z_k X_{k+2} \dots X_{l-2} Z_l | \Omega(\phi) \rangle \quad (\text{B.1.1})$$

where $1 \leq k, l \leq n$ and $k-l$ is even. First, we can write:

$$\rho_\phi = |\Omega(\phi)\rangle \langle \Omega(\phi)| = V(\phi) \rho_{n+2}^C V^\dagger(\phi) \quad (\text{B.1.2})$$

And compute the expectation values in the density matrix picture as $\text{Tr}(\sigma_{k,l} \rho_\phi)$. By the cyclicity of the trace, we can move the $V^\dagger(\phi)$ term to the front of the expression, then move it through $\sigma_{k,l}$. Then, any X rotations on sites k, l will have the angle flipped from $-\phi$ to ϕ - these flipped rotations meet their counterpart in the $RX_1(\phi)RX_2(\phi)RX_{n-1}(\phi)RX_n(\phi) \prod_{i=1}^{n-2} RXX_{i,i+2}(\phi)$ term and become a rotation by 2ϕ . The other rotations that commute with $\sigma_{k,l}$ remain as angle $-\phi$, and hence when combined with the $RX_1(\phi)RX_2(\phi)RX_{n-1}(\phi)RX_n(\phi) \prod_{i=1}^{n-2} RXX_{i,i+2}(\phi)$ term annihilate.

Let us first consider $k-l=2$. Then, $\sigma_{k,l}$ only anti-commutes with $RX_k(\phi)$ or $RXX_{k-2,k}(\phi)$ and the $RX_l(\phi)$ or $RXX_{l,l+2}(\phi)$ - hence only two terms remain (notably, it commutes with $RXX_{k,l}(\phi)$ as $[X_k X_l, Z_k Z_l] = 0$). WLOG suppose we are in the bulk so the terms left are $RXX_{k-2,k}(2\phi)$ and $RXX_{l,l+2}(2\phi)$ (the result is the same for the single X -rotations; indeed this is why they are placed at the qubits near the boundary, to maintain translation invariance of the string order parameters). We can then calculate:

$$\text{Tr}(\sigma_{k,l} \rho_{n+2}^C) = \text{Tr}(RXX_{k-2,k}(2\phi) RXX_{l,l+2}(2\phi) \rho_{n+2}^C) = \cos^2(\phi) \quad (\text{B.1.3})$$

where the last equality follows since none of the terms in $RX(X)_{k-2,k}(2\phi)RX(X)_{l,l+2}(2\phi)$ save for the identity with weight $\cos^2 \phi$ stabilize the cluster state.

For $k-l > 2$ we have that $\sigma_{k,l}$ anti-commutes with four terms - $RX_k(\phi)$ or $RXX_{k-2,k}(\phi)$, $RXX_{k,k+2}(\phi)$, $RXX_{l-2,l}(\phi)$, and $RX_l(\phi)$ or $RXX_{l,l+2}(\phi)$. So we have four terms remaining, with:

$$\text{Tr}(\sigma_{k,l} \rho_{n+2}^C) = \text{Tr}(RXX_{k-2,k}(2\phi) RXX_{k,k+2}(2\phi) RXX_{l-2,l}(2\phi) RXX_{l,l+2}(2\phi) \rho_{n+2}^C) = \cos^4(\phi) \quad (\text{B.1.4})$$

where again the last equality follows as none of the terms in

$RXX_{k-2,k}(2\phi)RXX_{k,k+2}(2\phi)RXX_{l-2,l}(2\phi)RXX_{l,l+2}(2\phi)$ stabilize the cluster state, save for the identity with weight $\cos^4 \phi$.

Hence, we conclude that:

$$\sigma_{k,l} = \sigma(k-l) = \sigma(d) = \begin{cases} \cos^2 \phi & d = 2 \\ \cos^4 \phi & d = 4, 6, \dots \end{cases} \quad (\text{B.1.5})$$

showing that the SOPs $\sigma(d)$ are convex (and also only depend on the separation d) for $|\Omega(\phi)\rangle$, a necessary condition for the state to test Prediction 4.

Note we can also compute $\sigma_k = \sigma_{\geq} = \langle Z_k X_{k+2} X_{k+4} \dots X_n Z_{n+1} \rangle$ in the same fashion; the only terms that commute with σ_k are $RXX_{k-2,k}(\phi)$ and $RXX_{k,k+2}(\phi)$ (or $RX_{1/2}(\phi), RX_{n-1/n}(\phi)$ if k is near one of the two boundaries). Only the identity term with weight $\cos^2 \phi$ stabilizes the cluster state and hence:

$$\sigma_k = \sigma_{\geq} = \cos^2 \phi. \quad (\text{B.1.6})$$

Although we have shown that the SOPs are convex, there are in fact some slight modifications we can make to $|\Omega(\phi)\rangle$ to make the SOPs non-decreasing. We discuss them briefly as they are the first such known examples. Consider the 9-qubit version of $|\Omega(\phi)\rangle$. Repeating the above SOP calculation for 9 qubits, we find that $\sigma_{2,4} = \cos^2 \phi$ but $\sigma_{2,6} = \cos^4 \phi + \sin^4 \phi$. The additional term in $\sigma_{2,6}$ arises as we have the product of rotations $RX_2(\phi)RX_{2,4}(\phi)RXX_{4,6}(\phi)RX_6(\phi)$, and hence we obtain a $\sin^4 \phi$ from the four-fold product of $-i \sin \phi X$ terms as well as the $\cos^4 \phi$ term from the $\cos \phi I$ terms. For $\pi/4 < \phi \leq \pi/2$ we find in this case therefore that $\sigma(4) > \sigma(2)$. We can also consider, for ≥ 11 qubits, a modified version of the state where we omit the boundary X -rotations, i.e.:

$$|\tilde{\Omega}(\phi)\rangle = \prod_{i=1}^{n-2} RXX_{i,i+2}(\phi) |C_{n+2}\rangle \quad (\text{B.1.7})$$

And if we repeat the SOP calculations with this state (simply omitting the $RX(\phi)$ terms), we find that $\sigma_{2,4} = \cos \phi$, $\sigma_{2,k} = \cos^3 \phi$ for $k = 6, 8, \dots, n-3$, and $\sigma_{2,n-1} = \cos^2 \phi$. Here again the SOPs do not strictly decrease with distance -the boundary terms are thus crucial in enforcing the convex decay.

B.2 Efficient circuits for measuring string order parameters

We derive the efficient/small circuits presented in Section 4.1.3 to measure the bulk string order parameters $\sigma(2), \sigma(4), \sigma(6)$. Our starting point is the “straightforwards” circuit presented in Fig. B.1 which consists of the full state preparation of $|\Omega(\phi)\rangle$ (On 11 qubits) followed by the measurement of the relevant Pauli string.

For any qubits that are unmeasured or measured in the X -basis, we can omit the X/XX rotations as these commute past the measurement. Another set of simplifications follows from considering a modification to the Tracing Lemma of Appendix A.3 which accounts for an XX -rotation between cluster state qubits. Consider a $n+2$ qubit cluster state $\rho_{0,\dots,n+1}^C$ with XX -rotation applied

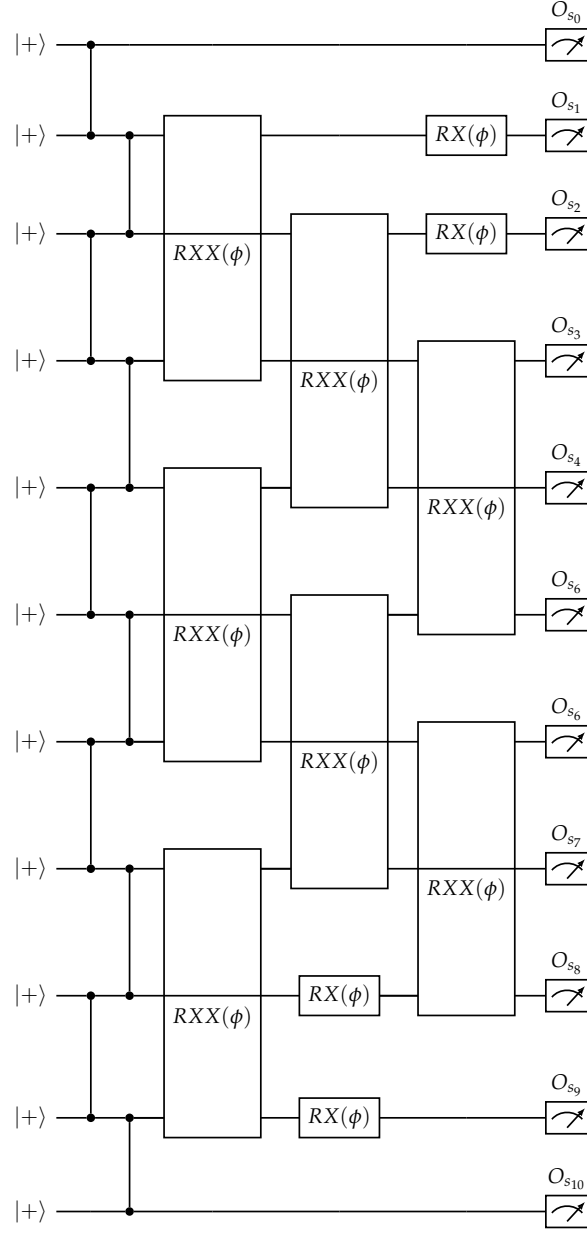


Figure B.1: Full circuit for measuring string order parameters of 11-qubit $|\Omega(\phi)\rangle$ state. We choose $O_{s_2} = Z_{s_2}, O_{s_3} = X_{s_3}, O_{s_4} = Z_{s_4}$ for measuring $\sigma(2)$, $O_{s_2} = Z_{s_2}, O_{s_3} = X_{s_3}, O_{s_5} = X_{s_5}, O_{s_6} = Z_{s_6}$ for measuring $\sigma(4)$, and $O_{s_2} = Z_{s_2}, O_{s_3} = X_{s_3}, O_{s_5} = X_{s_5}, O_{s_7} = X_{s_7}, O_{s_8} = Z_{s_8}$ for measuring $\sigma(6)$.

between qubits 0 and 2, and tracing out qubits 0,1. We start by tracing out qubit 0 taking the partial trace in the X-basis:

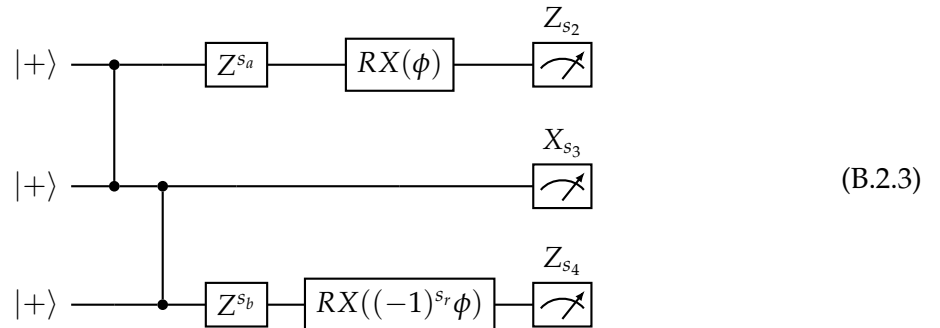
$$\begin{aligned}
\rho_{1,\dots,n+1} &= \text{Tr}_0(RXX_{0,2}(\phi)\rho_{0,\dots,n+1}^C RXX_{0,2}(-\phi)) \\
&= \langle +|_0 RXX_{0,2}(\phi)\rho_{0,\dots,n+1}^C RXX_{0,2}(-\phi) |+\rangle_0 + \langle -|_0 RXX_{0,2}(\phi)\rho_{0,\dots,n+1}^C RXX_{0,2}(-\phi) |-\rangle_0 \\
&= RX_2(\phi) \langle +|_0 \rho_{0,\dots,n+1}^C |+\rangle_0 RX_2(-\phi) + RX_2(-\phi) \langle -|_0 \rho_{0,\dots,n+1}^C |-\rangle_0 RX_2(\phi) \\
&= RX_2(\phi) H_1 \rho_{1,\dots,n+1}^C H_1 RX_2(-\phi) + RX_2(-\phi) H_1 Z_1 \rho_{1,\dots,n+1}^C Z_1 H_1 RX_2(\phi)
\end{aligned} \tag{B.2.1}$$

where the second line follows from $RXX_{0,2}(\phi) |\pm\rangle_{0,2} = \exp(-i\frac{\phi}{2} X_0 X_2) |\pm\rangle_0 = \exp(\mp i\frac{\phi}{2} X_2) |\pm\rangle_0 = |\pm\rangle_0 RX_2(\pm\phi)$ and the third line follows from considering the half-teleportation resulting from an X-measurement of a cluster state (with byproduct operator HZ^s depending on the measurement outcome s). Now tracing out qubit 1:

$$\begin{aligned}
\rho_{2,\dots,n+1} &= \text{Tr}_1(RX_2(\phi) H_1 \rho_{1,\dots,n+1}^C H_1 RX_2(-\phi) + RX_2(-\phi) H_1 Z_1 \rho_{1,\dots,n+1}^C Z_1 H_1 RX_2(\phi)) \\
&= \langle +|_1 RX_2(\phi) H_1 \rho_{1,\dots,n+1}^C H_1 RX_2(-\phi) + RX_2(-\phi) H_1 Z_1 \rho_{1,\dots,n+1}^C Z_1 H_1 RX_2(\phi) |+\rangle_1 \\
&\quad + \langle -|_1 RX_2(\phi) H_1 \rho_{1,\dots,n+1}^C H_1 RX_2(-\phi) + RX_2(-\phi) H_1 Z_1 \rho_{1,\dots,n+1}^C Z_1 H_1 RX_2(\phi) |-\rangle_1 \\
&= RX_2(\phi) \langle 0|_1 \rho_{1,\dots,n+1}^C |0\rangle_1 RX_2(-\phi) + RX_2(-\phi) \langle 0|_1 \rho_{1,\dots,n+1}^C |0\rangle_1 RX_2(\phi) \\
&\quad + RX_2(\phi) \langle 1|_1 \rho_{1,\dots,n+1}^C |1\rangle_1 RX_2(-\phi) + RX_2(-\phi) \langle 1|_1 \rho_{1,\dots,n+1}^C |1\rangle_1 RX_2(\phi) \\
&= RX_2(\phi) \rho_{2,\dots,n+1}^C RX_2(-\phi) + RX_2(-\phi) \rho_{2,\dots,n+1}^C RX_2(\phi) \\
&\quad + RX_2(\phi) Z_2 \rho_{2,\dots,n+1}^C Z_2 RX_2(-\phi) + RX_2(-\phi) Z_2 \rho_{2,\dots,n+1}^C Z_2 RX_2(\phi)
\end{aligned} \tag{B.2.2}$$

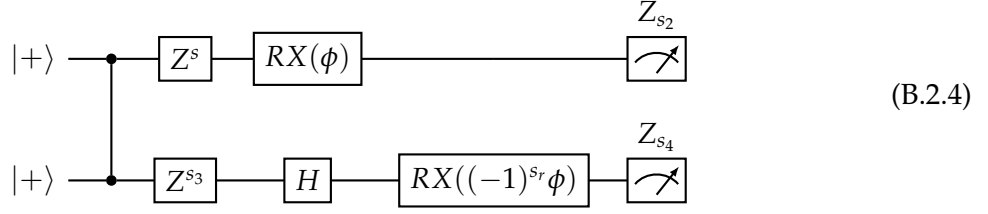
So we are left with a n -qubit cluster state with X-rotation on qubit 2 (with probability 1/2 that the rotation angle is flipped) and a Z-error on qubit 2 also with probability 1/2. If we have traced out the cluster state before this point (i.e. we start this argument with a cluster state with a Z-error on the boundary) we obtain the same result.

With these simplification tools let us derive the simplified circuits, starting with that for the measurement of $\sigma(2) = \sigma_{2,4} = \langle Z_2 X_3 Z_4 \rangle$. We can omit all X/XX-rotations except for $RX_2(\phi)$, $RXX_{2,4}(\phi)$, and $RXX_{4,6}(\phi)$. Additionally, we notice that $RXX_{2,4}(\phi)$ commutes with $\sigma_{2,4}$ and it too can be omitted. Tracing out qubits 0,1 and $5, \dots, 10$ we obtain:



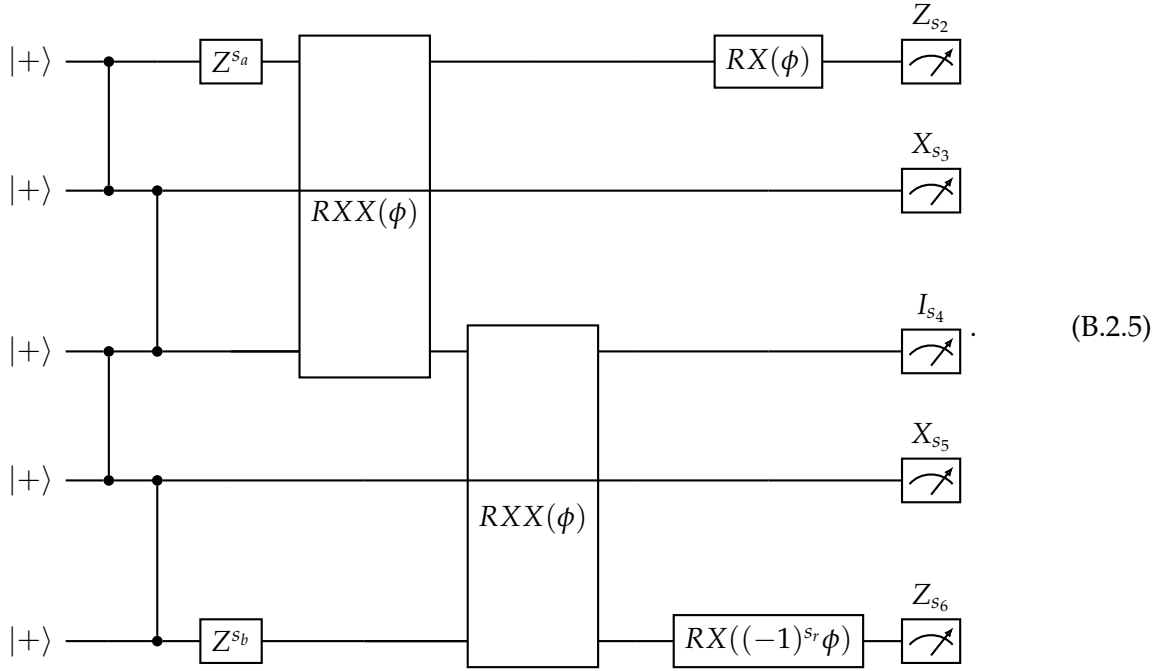
where s_a, s_b, s_r are 0/1 with 50/50 probability. By pulling out a cluster state stabilizer we can convert Z^{s_b} to Z^{s_a} and so we can just consider a single 50/50 Z^s error on the s_2 qubit line. In

addition, we can perform a half-teleportation on the s_3 qubit, yielding:

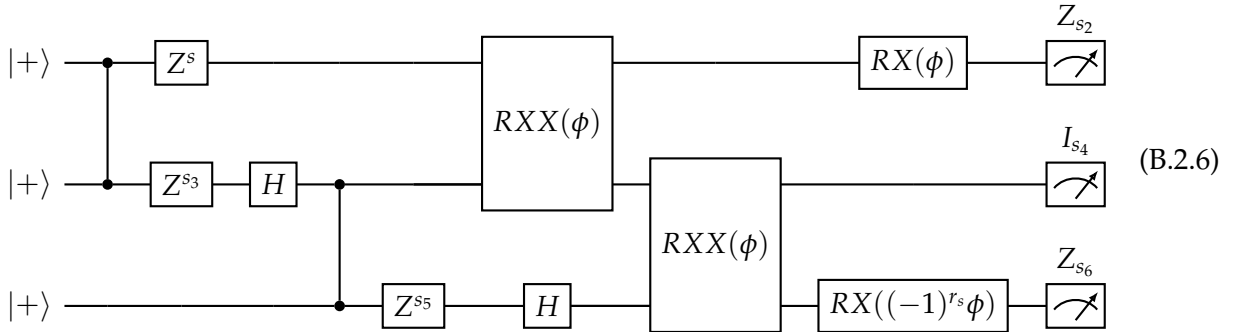


and commuting the Z s before the CZ gate we obtain the circuit in Table 4.4.

Next we consider the measurement of $\sigma(4) = \sigma_{2,6} = \langle Z_2 X_3 X_5 Z_6 \rangle$. We can omit all X/XX -rotations except for $RX_2(\phi)$, $RXX_{2,4}(\phi)$, $RXX_{4,6}(\phi)$, and $RXX_{4,6}(\phi)$. Tracing out qubits 0, 1 and $7, \dots, 10$ we obtain:

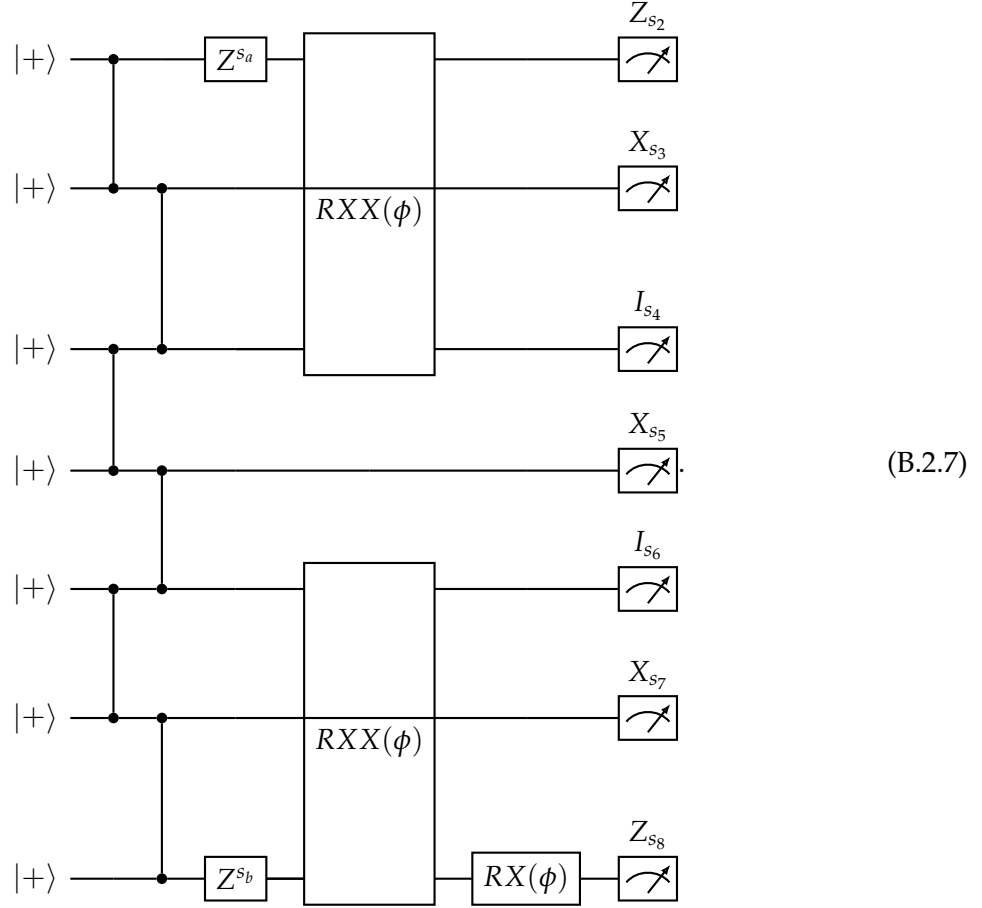


By pulling out a cluster state stabilizer ($Z_2 X_3 I_4 X_4 Z_5$) we can convert Z^{s_b} to Z^{s_a} so again we can just consider a single 50/50 Z^s error on the s_2 qubit line. In addition, we can perform a half-teleportation on the s_3 and s_5 qubits, which yields:

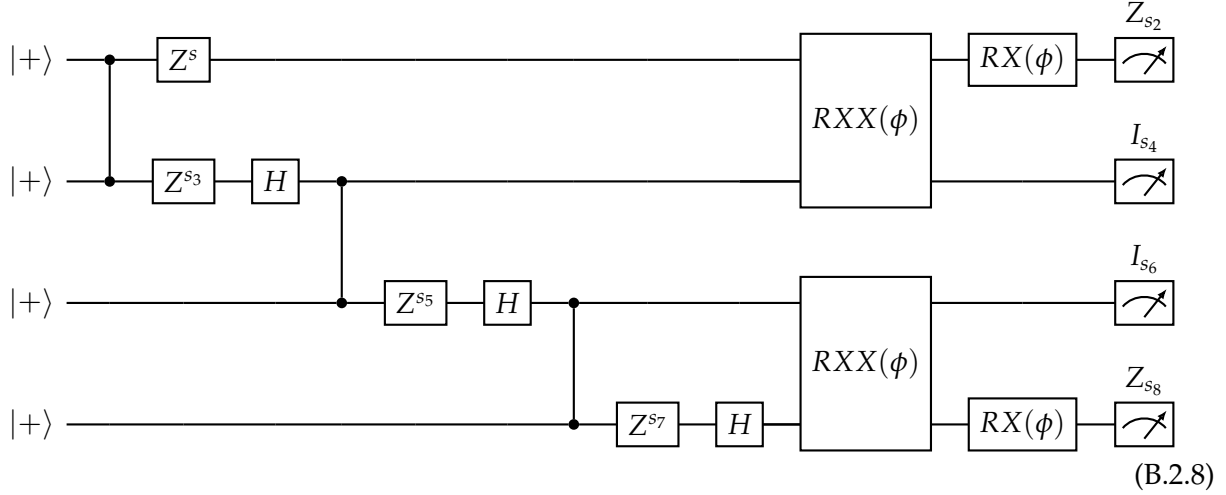


which commuting the initial Zs yields the circuit in Table 4.6.

Finally, we consider the measurement of $\sigma(6) = \sigma_{2,8} = \langle Z_2 X_3 X_5 X_7 Z_8 \rangle$. We can omit all X/XX-rotations except for $RX_2(\phi)$, $RXX_{2,4}(\phi)$, $RXX_{6,8}(\phi)$, and $RX_8(\phi)$. Tracing out qubits 0, 1 and 9, 10 we obtain:



Again repeating the conversion to the single Z error and the half-teleportations, we obtain:



which commuting the initial Zs yields the circuit in Table 4.8.

B.3 Analytical calculations of loss in purity for various rotation splittings

Using Eq. (2.3.15):

$$\begin{bmatrix} \langle \bar{X} \rangle \\ \langle \bar{Y} \rangle \\ \langle \bar{Z} \rangle \end{bmatrix} = \left\langle \left(\prod_{j \in \mathcal{R}} \begin{bmatrix} \cos \beta & -S_j \sin \beta & 0 \\ S_j \sin \beta & \cos \beta & 0 \\ 0 & 0 & 1 \end{bmatrix} \right) \right\rangle \begin{bmatrix} \langle \bar{X}_0 \rangle \\ \langle \bar{Y}_0 \rangle \\ \langle \bar{Z}_0 \rangle \end{bmatrix} \quad (\text{B.3.1})$$

we can track the evolution of $\bar{X}, \bar{Y}, \bar{Z}$ through multiple logical rotations. We can then compute the output expectation values and loss in purity as a function of the total logical rotation angle β and the XX -rotation angle ϕ of the resource state (using known expectation values of string order operators $S_j = Z_j X_{j+1} X_{j+3} \dots X_n Z_{n+1}$ and their products $S_{j_1, j_2, \dots} = S_{j_1} S_{j_2} \dots$). In our case, we have $\langle \bar{X}_0 \rangle = 1$ and $\langle \bar{Y}_0 \rangle = \langle \bar{Z}_0 \rangle = 0$. We can omit \bar{Z} as it is unmodified by Z -rotations. Hence our evolution equation becomes:

$$\begin{bmatrix} \langle \bar{X} \rangle \\ \langle \bar{Y} \rangle \end{bmatrix} = \left\langle \left(\prod_{j \in \mathcal{R}} \begin{bmatrix} \cos \beta & -S_j \sin \beta \\ S_j \sin \beta & \cos \beta \end{bmatrix} \right) \right\rangle \begin{bmatrix} 1 \\ 0 \end{bmatrix}. \quad (\text{B.3.2})$$

We compute the output expectation values for various choices of splitting the logical rotation angle. The loss in purity of the logical information can be computed in each case as:

$$\text{LP} = 1 - \langle \bar{X} \rangle^2 - \langle \bar{Y} \rangle^2. \quad (\text{B.3.3})$$

For two $\beta/2$ rotations separated by $\Delta = 2$ (concretely - on qubits 2, 4) we have:

$$\begin{aligned}
\begin{bmatrix} \langle \bar{X} \rangle \\ \langle \bar{Y} \rangle \end{bmatrix} &= \left\langle \begin{bmatrix} \cos(\frac{\beta}{2}) & -S_4 \sin(\frac{\beta}{2}) \\ S_4 \sin(\frac{\beta}{2}) & \cos(\frac{\beta}{2}) \end{bmatrix} \begin{bmatrix} \cos(\frac{\beta}{2}) & -S_2 \sin(\frac{\beta}{2}) \\ S_2 \sin(\frac{\beta}{2}) & \cos(\frac{\beta}{2}) \end{bmatrix} \right\rangle \begin{bmatrix} 1 \\ 0 \end{bmatrix} \\
&= \begin{bmatrix} \cos^2(\frac{\beta}{2}) - \sigma_{2,4} \sin^2(\frac{\beta}{2}) \\ (\sigma_2 + \sigma_4) \sin(\frac{\beta}{2}) \cos(\frac{\beta}{2}) \end{bmatrix} \\
&= \begin{bmatrix} \cos^2(\frac{\beta}{2}) - \cos^2 \phi \sin^2(\frac{\beta}{2}) \\ 2 \cos^2 \phi \sin(\frac{\beta}{2}) \cos(\frac{\beta}{2}) \end{bmatrix}
\end{aligned} \tag{B.3.4}$$

Where in the second equality we use that $\langle S_2 S_4 \rangle = \langle S_{2,4} \rangle = \sigma_{2,4}$ and $\langle S_{2/4} \rangle = \sigma_{2/4}$ and in the last equality we use that $\sigma_{2,4} = \sigma(2)$ and $\sigma_{2/4} = \sigma_{\geq}$ and apply the results of Appendix B.1.

For two $\beta/2$ rotations separated by $\Delta = 6$ (on qubits 2, 8), we can modify the above:

$$\begin{aligned}
\begin{bmatrix} \langle \bar{X} \rangle \\ \langle \bar{Y} \rangle \end{bmatrix} &= \begin{bmatrix} \cos^2(\frac{\beta}{2}) - \sigma_{2,8} \sin^2(\frac{\beta}{2}) \\ (\sigma_2 + \sigma_8) \sin(\frac{\beta}{2}) \cos(\frac{\beta}{2}) \end{bmatrix} \\
&= \begin{bmatrix} \cos^2(\frac{\beta}{2}) - \cos^4 \phi \sin^2(\frac{\beta}{2}) \\ 2 \cos^2 \phi \sin(\frac{\beta}{2}) \cos(\frac{\beta}{2}) \end{bmatrix}
\end{aligned} \tag{B.3.5}$$

noting the modification that $\sigma_{2,8} = \sigma(6) = \cos^4 \phi$ compared to the $\Delta = 2$ case. Note that two rotations separated by $\Delta = 4$ yields the same result as $\sigma(4) = \sigma(6)$.

For three $\beta/3$ rotations separated by $\Delta = 2$ (on qubits 2, 4, 6), we have:

$$\begin{aligned}
\begin{bmatrix} \langle \bar{X} \rangle \\ \langle \bar{Y} \rangle \end{bmatrix} &= \left\langle \begin{bmatrix} \cos(\frac{\beta}{3}) & -S_6 \sin(\frac{\beta}{3}) \\ S_6 \sin(\frac{\beta}{3}) & \cos(\frac{\beta}{3}) \end{bmatrix} \begin{bmatrix} \cos(\frac{\beta}{3}) & -S_4 \sin(\frac{\beta}{3}) \\ S_4 \sin(\frac{\beta}{3}) & \cos(\frac{\beta}{3}) \end{bmatrix} \begin{bmatrix} \cos(\frac{\beta}{3}) & -S_2 \sin(\frac{\beta}{3}) \\ S_2 \sin(\frac{\beta}{3}) & \cos(\frac{\beta}{3}) \end{bmatrix} \right\rangle \begin{bmatrix} 1 \\ 0 \end{bmatrix} \\
&= \begin{bmatrix} \cos^3(\frac{\beta}{3}) - (\sigma_{2,4} + \sigma_{4,6} + \sigma_{2,6}) \cos(\frac{\beta}{3}) \sin^2(\frac{\beta}{3}) \\ (\sigma_2 + \sigma_4 + \sigma_6) \cos^2(\frac{\beta}{3}) \sin(\frac{\beta}{3}) + \sigma_{2,4,6} \sin^3(\frac{\beta}{3}) \end{bmatrix} \\
&= \begin{bmatrix} \cos^3(\frac{\beta}{3}) - 2 \cos^2 \phi \cos(\frac{\beta}{3}) \sin^2(\frac{\beta}{3}) - \cos^4 \phi \cos(\frac{\beta}{3}) \sin^2(\frac{\beta}{3}) \\ 3 \cos^2 \phi \cos^2(\frac{\beta}{3}) \sin(\frac{\beta}{3}) + \cos^2 \phi \sin^3(\frac{\beta}{3}) \end{bmatrix}
\end{aligned} \tag{B.3.6}$$

The only non-familiar jump in the last line is with the three-body expectation value $\sigma_{2,4,6} = \langle Z_2 X_3 Z_4 Z_6 X_7 X_9 Z_{10} \rangle$. Noting that the operator only anti-commutes with the two rotations $RX_2(\phi)$ and $RXX_{6,8}(\phi)$, the SOP has value (by the same line of arguments as Appendix B.1) $\cos^2 \phi$.

If we have three $\beta/3$ rotations, two separated by $\Delta = 2$ and two separated by $\Delta = 4$ (on qubits 2,

4, 8), we instead obtain:

$$\begin{aligned}
\begin{bmatrix} \langle \bar{X} \rangle \\ \langle \bar{Y} \rangle \end{bmatrix} &= \left\langle \begin{bmatrix} \cos(\frac{\beta}{3}) & -S_8 \sin(\frac{\beta}{3}) \\ S_8 \sin(\frac{\beta}{3}) & \cos(\frac{\beta}{3}) \end{bmatrix} \begin{bmatrix} \cos(\frac{\beta}{3}) & -S_4 \sin(\frac{\beta}{3}) \\ S_4 \sin(\frac{\beta}{3}) & \cos(\frac{\beta}{3}) \end{bmatrix} \begin{bmatrix} \cos(\frac{\beta}{3}) & -S_2 \sin(\frac{\beta}{3}) \\ S_2 \sin(\frac{\beta}{3}) & \cos(\frac{\beta}{3}) \end{bmatrix} \right\rangle \begin{bmatrix} 1 \\ 0 \end{bmatrix} \\
&= \begin{bmatrix} \cos^3(\frac{\beta}{3}) - (\sigma_{2,4} + \sigma_{4,8} + \sigma_{2,8}) \cos(\frac{\beta}{3}) \sin^2(\frac{\beta}{3}) \\ (\sigma_2 + \sigma_4 + \sigma_8) \cos^2(\frac{\beta}{3}) \sin(\frac{\beta}{3}) + \sigma_{2,4,8} \sin^3(\frac{\beta}{3}) \end{bmatrix} \\
&= \begin{bmatrix} \cos^3(\frac{\beta}{3}) - \cos^2 \phi \cos(\frac{\beta}{3}) \sin^2(\frac{\beta}{3}) - 2 \cos^4 \phi \cos(\frac{\beta}{3}) \sin^2(\frac{\beta}{3}) \\ 3 \cos^2 \phi \cos^2(\frac{\beta}{3}) \sin(\frac{\beta}{3}) + \cos^4 \phi \sin^3(\frac{\beta}{3}) \end{bmatrix}
\end{aligned} \tag{B.3.7}$$

Where we note that $\sigma_{2,4,8} = \langle Z_2 X_3 Z_4 Z_8 X_9 Z_1 0 \rangle = \cos^4 \phi$ as the operator anti-commutes with $RX_2(\phi)$, $RXX_{4,6}(\phi)$, $RXX_{6,8}(\phi)$, and $RX_8(\phi)$.

Finally, for four $\beta/4$ rotations separated by $\Delta = 2$ (on qubits 2,4,6,8) we have:

$$\begin{aligned}
\begin{bmatrix} \langle \bar{X} \rangle \\ \langle \bar{Y} \rangle \end{bmatrix} &= \left\langle \left(\prod_{j \in \{2,4,6,8\}} \begin{bmatrix} \cos \beta & -S_j \sin \beta \\ S_j \sin \beta & \cos \beta \end{bmatrix} \right) \right\rangle \begin{bmatrix} 1 \\ 0 \end{bmatrix} \\
&= \begin{bmatrix} \cos^4(\frac{\beta}{4}) + \sigma_{2,4,6,8} \sin^4(\frac{\beta}{4}) - (\sigma_{2,4} + \sigma_{2,6} + \sigma_{2,8} + \sigma_{4,6} + \sigma_{4,8} + \sigma_{6,8}) \cos^2(\frac{\beta}{4}) \sin^2(\frac{\beta}{4}) \\ (\sigma_2 + \sigma_4 + \sigma_6 + \sigma_8) \cos^3(\frac{\beta}{4}) \sin(\frac{\beta}{4}) - (\sigma_{2,4,6} + \sigma_{2,4,8} + \sigma_{2,6,8} + \sigma_{4,6,8}) \cos(\frac{\beta}{4}) \sin^3(\frac{\beta}{4}) \end{bmatrix} \\
&= \begin{bmatrix} \cos^4(\frac{\beta}{4}) + \sigma_{2,4,6,8} \sin^4(\frac{\beta}{4}) - (\sigma_{2,4} + \sigma_{2,6} + \sigma_{2,8} + \sigma_{4,6} + \sigma_{4,8} + \sigma_{6,8}) \cos^2(\frac{\beta}{4}) \sin^2(\frac{\beta}{4}) \\ (\sigma_2 + \sigma_4 + \sigma_6 + \sigma_8) \cos^3(\frac{\beta}{4}) \sin(\frac{\beta}{4}) - (\sigma_{2,4,6} + \sigma_{2,4,8} + \sigma_{2,6,8} + \sigma_{4,6,8}) \cos(\frac{\beta}{4}) \sin^3(\frac{\beta}{4}) \end{bmatrix} \\
&= \begin{bmatrix} \cos^4(\frac{\beta}{4}) + \cos^2 \phi \sin^4(\frac{\beta}{4}) - 3 \cos^2 \phi \cos^2(\frac{\beta}{4}) \sin^2(\frac{\beta}{4}) - 3 \cos^4 \phi \cos^2(\frac{\beta}{4}) \sin^2(\frac{\beta}{4}) \\ 4 \cos^2 \phi \cos^3(\frac{\beta}{4}) \sin(\frac{\beta}{4}) - 2 \cos^2 \phi \cos(\frac{\beta}{4}) \sin^3(\frac{\beta}{4}) - 2 \cos^4 \phi \cos(\frac{\beta}{4}) \sin^3(\frac{\beta}{4}) \end{bmatrix}
\end{aligned} \tag{B.3.8}$$

Where we note that $\sigma_{2,4,6,8} = \langle Z_2 X_3 Z_4 Z_6 X_7 Z_8 \rangle = \cos^2 \phi$ as the operator only anti-commutes with $RX_2(\phi)$ and $RX_8(\phi)$.